Master's thesis

NTNU
Norwegian University of Science and Technology
Faculty of Engineering
Department of Ocean Operations and Civil Engineering

Hamed Ghaffari Darab

Experimental and CFD Analysis of Sloshing in Water, Liquid Hydrogen and Liquified Natural Gas Tanks

Master's thesis in Product and System Design
Supervisor: Vilmar Æsøy and Ann Rigmor Nerheim
December 2021

NTNU
Norwegian University of
Science and Technology

Hamed Ghaffari Darab

Experimental and CFD Analysis of Sloshing in Water, Liquid Hydrogen and Liquified Natural Gas Tanks

Master's thesis in Product and System Design
Supervisor: Vilmar Æsøy and Ann Rigmor Nerheim
December 2021

Norwegian University of Science and Technology
Faculty of Engineering
Department of Ocean Operations and Civil Engineering

NTNU
Norwegian University of
Science and Technology

Abstract

The sloshing phenomenon of water in rectangular, and water, liquid hydrogen (LH2), and liquefied natural gas (LNG) in cylindrical tanks are investigated and compared in this thesis. The sloshing phenomenon in the partially filled tanks have challenges that need to be studied. These problems can affect the system's performance and stability. In terms of efficiency, the rapid pressure drop which occurs inside the tank causing issues such as not getting enough fuel to the engine and eventually causing the engine to shut down is directly related to the intensity of sloshing motion inside the partially filled fuel tanks such as LNG or LH2 tanks. In terms of stability, the intensity of motion inside the tanks can damage the tank walls and the stability of the system thus, in this thesis, the sloshing phenomenon is studied experimentally and numerically in partially filled tanks filled with different fluids to determine how to suppress the sloshing severity inside these tanks.

Due to the limitation of using LNG and LH2, water and air are selected to be the main fluids used in the experimental part of this study with the applied pitch motion of 4.8 degrees on the tank and different filling levels of 30 and 50%. The applied moment force on the rectangular tank is recorded during the experiments to be used for validating the numerical results. In addition to the patterns correspondence, the recorded data of different experimental cases are used to validate the numerically obtained data.

The numerical part of the thesis utilizes the CFD method to perform the simulations based on the volume of fluid (VOF) multi-phase method. The turbulence 2D and 3D models of RANS are applied to obtain the numerical results. To find the most severe motion inside the tanks, empirical formulas and methods are used to estimate the natural frequency and period for each filling level and tank types. To make sure that the empirical formulas work correctly, other excitation periods are added to the estimated natural period and after finding the correct natural period, the results using the natural period including the imposed hydrodynamic forces and pressure on the tank walls, the free surface elevation, and the moment force applied on the tank are investigated.

To suppress the sloshing severity, two different types of baffles including the low central and slot central baffles are used within the rectangular tank and for the cylindrical tank, only the low central baffle is deployed. Numerical simulations of the rectangular tank cover all the filling levels of 30,50, and 70% using water as the main fluid whereas, the cylindrical tank simulations are limited to use only one filling level of 30% but with all three fluids of water, LH2 and LNG to be able to have comparisons between the results achieved from all fluid types.

All the rectangular tank baffles are found to be effective in suppressing sloshing intensity, but the slot baffle is found to be the most efficient by having a 59.5% of reduction in the imposed forces on the tank walls. The low baffle in the cylindrical tank shows an efficiency ranges from 18 to 25 percent in reducing the imposed forces on the tank walls.

For future work since the slot baffle is showing high efficiency, the developed slot baffle can be deployed in different positions of the tanks as well as including more motion types and amplitude to be more close to the real conditions.

Preface

My master's thesis at the Norwegian University of Science and Technology in Ålesund resulted in this report. I would like to thank my supervisors Vilmar Æsøy and Ann Rigmor Nerheim for all the constant help, guidance, and supports they gave me. Additionally, I would like to express my gratitude to Henry Peter Piehl, Marko Mikulec, and Karl Henning Halse for their assistance and guidance regarding the CFD and software license. I would like to thank my assistant supervisor Nastaran for all her help and time, especially when it came to the experimental part of my research. NTNU's Department of Ocean Operations and Civil Engineering would like to thank all its staff, colleagues, and friends. Also, I would like to thank my parents and family for their support throughout the years and for never stopping to motivate me.

It would not have been possible to complete this thesis without the assistance of all these people.

Nomenclature

Abbreviations

CAD	Computer Aided Design
CFD	Computational Fluid Dynamics
CV	Control Volume
DEM	Discrete Element Model
DES	Detached Eddy Simulation
DMP	Dispersed Multi-phase Model
DNS	Direct Numerical Simulation
EMP	Eulerian Multi-phase
FVM	Finite Volume Method
IMO	International Marine Organization
JONSWAP	Joint North Sea Wave Project
LES	Large Eddy Simulation
LH2	Liquefied Hydrogen
LMP	Lagrangian Multi-phase
LNG	Liquefied Natural Gas
RANS	Reynolds Averaged Navier-Stokes
RPM	Rotation Per Minute
VBF	Virtual Boundary Force
VOF	Volume of Fluid

List of Symbols

S_E	heat source
α_i	volume fraction
γ_n	frequency parameter
$(C_p)_i$	specific heat of the i th phase
μ_i	molecular viscosity
ω	Angular frequency [rad/s]
$\otimes$	Kronecker product
ρ	Density [kg/m^3]
σ	stress tensor
θ	angle [degrees]
A	Amplitude [Degrees]

a	fluid depth
b	tank length
C_a	sharpening factor
E	energy [J]
f	frequency [H_z]
f_n	natural frequency
g	gravity
H	height [m]
L	length [m]
n	frequency mode number
P	pressure [Pa]
q	heat flux
R	radius
Re	Reynolds number
S	mean strain rate tensor
T	period
t	time [s]
T_n	natural period
V	velocity [m/s]
W	width [m]

Table of Contents

List of Figures

List of Tables

1 Introduction

1.1 Background and Motivation

As the most abundant element in the universe, hydrogen has one proton and one electron. However, despite its abundance, hydrogen cannot be found in the gaseous state in nature, thus it is always combined with other elements, like hydrogen and oxygen combined as H2O. [7]. In addition to the gaseous state, hydrogen can also be liquefied; therefore, hydrogen must be cooled to -253°C in order to liquefy it in atmospheric pressure [32]. As its background hydrogen for the first time was liquefied by a Scottish chemist named James Dewar in 1898 by using the regenerating cooling method and his vacuum flask invention [1].

Liquid Hydrogen (LH2) as a high-energy substance has various applications such as rockets and vehicles fuel for combustion with Oxygen or fluorine but it can be said that the majority of using LH2 is in air and space production [22]. Furthermore, liquid hydrogen can also be used as fuel for internal combustion engines, fuel cells, and hydrogen-powered ships fuel.

Car manufacturers have built some concepts using LH2 as the fuel, and engineers are modifying liquefied natural gas (LNG) systems in order to be used as LH2 systems, due to the similarities between the two systems and the advantage of having hydrogen fuel cells to power the electrical engines. By burning hydrogen in the engines, such cars will convert the chemical energy of hydrogen to mechanical energy. They can also get a reaction of mixing Hydrogen and Oxygen in the fuel cells to provide the required power for electric motors. The race car 'BMW H2R' is one of the LH2-powered cars that generates 232 horsepower which is able to achieve the top speed of 300 kmh [3].

The maritime sector is also investing in hydrogen-powered vessels as shipping accounts for 2,5 percent of world greenhouse gas emissions, according to the International Maritime Organization (IMO) thus, it has a promising prospect of achieving zero-emission shipping in the near term. The world's first liquid hydrogen fuel cell cruise ship is planned to be built in 2023 in Norway and it is going to be done by combining liquid hydrogen fuel cells with battery storage [9]. Fuel cells are used to power electric motors, either in automobiles or to rotate propellers of the ships and if they are used with pure hydrogen, they will be completely carbon-free with the only byproducts of electricity, heat, and water [8]. Besides the liquid hydrogen tanks which are used as fuel tanks for shuttles, cars, and hydrogen-powered ships, the storage, and transportation of liquid hydrogen in tanks is also a big concern.

1.2 Hydrogen Storage

Hydrogen storage and transformation are considered as one of the topmost concerns in the hydrogen industry. There are currently various hydrogen storage technologies available, but none fully meets all the requirements of the industry. Nowadays hydrogen can be stored in various ways consisting of gas, liquid, and solid forms which are explained in the following.

Hydrogen in Compressed Gas Form

Physically, hydrogen can be stored as compressed gas form by keeping it under pressure which increases the storage density. Such a process is done to decrease the volume of the gas that as an example it can be referred to the compressed hydrogen tanks systems in vehicles at 350 - 700 bar [20].

Hydrogen in Cryogenic Liquid Form

Cryogenic tanks are used either for the distribution or storing liquid hydrogen. These cryogenic tanks are meant to maintain the necessary temperature of cryogenic liquids and tank pressure. These tanks have been built like a bottle of thermos [10] which means there are two cylinders, which one, is within the another and the space between the two layers is filled with a material that provides insulation.

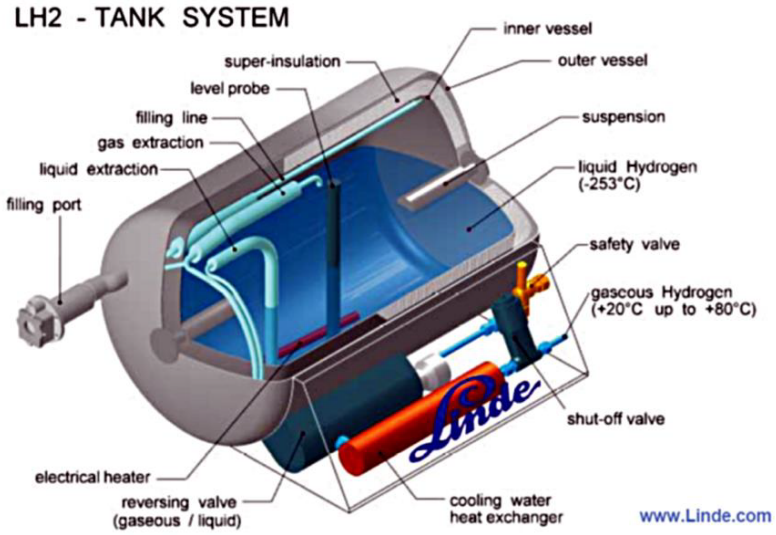

Figure 1: Liquid hydrogen tank [2]

In the liquid form, the cryogenic temperature is needed to store hydrogen therefore, if it is cooled down to -253°C, it will be liquefied and then it can be stored in insulated tanks. It should be mentioned that to reduce the boil-off gas it is necessary to keep this low temperature. Beneficially, the liquid form of hydrogen permits substantial stocking reduction since gaseous hydrogen requires 4 times the space of liquid hydrogen; equipment and structure weight would be reduced accordingly. It can be said that liquid hydrogen may be a more beneficial choice where the size and weight matter [6].

Hydrogen in Solid Form

By absorbing hydrogen into another material, hydrogen can be stored in solid form such as surface absorption meaning that hydrogen is bound to the surface of a substance either as hydrogen molecules or as hydrogen atoms during adsorption. In adsorption, hydrogen is attached to the surface of material either as hydrogen molecules or as hydrogen atoms. 'Hydrogen is dissociated into H-atoms, and then the hydrogen atoms are incorporated into the solid lattice framework'. In these components, only a low mass of hydrogen can be contained, which is the main drawback of this technology at present [4].

1.3 Challenges and Objectives

In addition to the storage challenges, there are still other challenges that need to be solved. Sloshing is one of the major industrial challenges and has been the interest of a lot of researchers across the world. The movement of a liquid inside another object like a tank or a container is called sloshing which occurs when the frequency of the partially-filled tank motion is close to the natural frequency of the liquid in the tank. When the free surface of a liquid generates sloshing, the loads created by sloshing will affect various factors. The temperature of the fluid, the tank movement, and the filling level are some of the factors that should be taken into account as well. In the context of hydrodynamics, imposed forces on the tank walls that lead to instability and structural damages should be considered thus, the fundamental problem posed by sloshing is to determine the distribution of hydrodynamic pressure, forces, moments, and natural frequencies. Another important problem that occurs due to sloshing is the pressure drop. As the tank moves, thermal

energy is transferred more rapidly, causing an abrupt pressure drop, therefore, sloshing results in the time reduction to reach the equilibrium of temperature and pressure [26]. This means that the pressure drop inside the tank is highly dependent on the intensity of sloshing [27]. As an example, in the maritime low-pressure fuel systems, if the sloshing occurs in a fuel tank, the pressure of the system will drop, and accordingly, the fuel is not transported to the engine which leads to the engine shutdown [14] [23].

The descriptions above strongly suggest that the intensity of sloshing and means of suppressing sloshing severity should be studied in further detail. This research studies the numerical and experimental analysis of the sloshing intensity including the free surface movement of the liquid and the hydrodynamic forces and impact pressures on the walls of the horizontally positioned tanks that are filled with various fluids when they are in various geometry types (rectangular and cylindrical) and filling levels by applying the certain degree of pitch motion to the tanks, in addition, modify the tank design to reduce the sloshing severity by deploying anti-wave baffles of different types including low and slot central baffles for the rectangular tank and the low central baffle for the cylindrical tank which ends to comparing the results with non baffled cases and experimental results.

1.4 Scope of the Research

The scope of this research consists of, the experimental study, the Computational Fluid Dynamic (CFD) study, and the comparison between them to investigate the possibility of comparing water, LH2, and LNG results.

Experimental study

The experimental part of this thesis covers the experiments using only the rectangular tank equipped with a low central baffle and without baffle. Experimental results are obtained from the rectangular tank which is only filled with water with two filling levels of 30 and 50% over three excitation periods of 1.65s 2.35s and 3s (refer to Table 3). Due to the limitations, water is used as the main liquid since liquid hydrogen or LNG experiments require special equipment to keep the cryogenic temperature of the tank which shows limitations are inherent to any experimental work therefore no experiments are conducted using LH2 or LNG. The moment force applied to the tank is measured and recorded to be used for the validation part. In addition to the moment force, the correspondence of the patterns is also compared between the experimental and simulation patterns. The measured data is classified in the empty tank and filled tank results for each specific excitation period.

CFD study

CFD is a numerical method of fluid analysis that can be used to analyze complex fluid-fluid, fluid-solid, or fluid-gas relationships. Complex CFD solvers transform the laws of fluid mechanics, physical, hydrodynamics, and aerodynamics into algebraic equations and solve the equations numerically which enables the designers to do the different simulations in different conditions. In this study, CFD that is conducted using STAR-CCM+ helps to simulate the sloshing phenomenon within the tanks to measure imposed hydrodynamic forces and pressures on the tank walls, capturing the free surface movement to show the motion intensity, and find the natural frequency of the tank leads to the most severe motions in the tanks. The 2D CFD tanks models are developed including the rectangular and cylindrical tanks. The 2D model is more rapidly simulated which reduces its computational time and cost, therefore for most of the numerical simulation, the 2D model is selected, although one 3D case is modeled to support the 2D results. The Reynolds-averaged Navier–Stokes (RANS) turbulence model and volume of fluid (VOF) multi-phase model are selected to model all the CFD models that are explained in chapter 3.2 in detail.

The numerical simulations of the rectangular tanks for non baffled and baffled cases are performed covering the three different filling levels of 30, 50, and 70% corresponding to 7.5, 12.5, and 17.5cm of fluid height respectively (refer to Table 4). Since the obtained results from the rectangular tank simulations are validated with the experimental ones, water and air are selected as the multi-phase of rectangular tank simulations. The diversity of the rectangular tank results that are obtained from

the CFD model can be summarized as finding the natural frequency of the tank, force and pressure measurement on the left tank walls, free surface elevation on a defined plane positioned 3cm away from the left tank wall, the peak forces recorded on the left tank wall and the measurement of the applied moment force on the tank to be compared with the experimental obtained moment forces.

The cylindrical tank CFD model uses the same principles as those for the rectangular tank except the filling level, the baffle type, and the defined multi-phase. The numerical simulations for the cylindrical tank whether it is baffled or non baffled are performed using only one defined filling level of 30% (7.2cm fluid height). The slot baffle is not included in the simulations of the cylindrical tank meaning the only baffle type that is used is the low central baffle. Because of the cylindrical shape the baffle should be annular but since the model is 2D a low central baffle is used. The simulations are performed firstly with water and air, secondly with LH2 and H2, and lastly LNG and CH4 as the defined multi-phase flow.

Comparison of Numerical and Experimental Study

This study also covers the comparison between the obtained results from numerical and experimental to validate the CFD work. Due to the previously explained limitations, only the experimental results of the rectangular tank filled with water are compared with the numerical ones and when the CFD method is validated, the comparisons are expanded to compare the numerical results of the cylindrical tanks filled with the other fluids of LH2 and LNG, this means the final comparison is conducted between the results taken from the water, LH2, and LNG including maximum forces and pressure measurement on the left hemisphere of the tank as well as the free surface elevation comparison between baffled and non baffled cases over different excitation periods.

1.5 Numerical and Experimental Cases

Cases that are studied in this thesis are classified as below tables show.

Table 1: 2D numerical cases of rectangular tank

Baffle Type	Filling Level	Excitation Period (s)	Amplitude	Fluid
Without Baffle	30%	1.3, 1.65, 1.9, 2.35, 2.7, 3	4.8 deg	Water
Without Baffle	50%	1.45, 1.65, 1.85, 2.35, 2.7, 3	4.8 deg	Water
Without Baffle	70%	1.2, 1.4, 1.6, 1.9, 2.35, 3	4.8 deg	Water
Low Central Baffle	30%	1.3, 1.65, 1.9, 2.35, 2.7, 3	4.8 deg	Water
Low Central Baffle	50%	1.45, 1.65, 1.85, 2.35, 2.7, 3	4.8 deg	Water
Low Central Baffle	70%	1.2, 1.4, 1.6, 1.9, 2.35, 3	4.8 deg	Water
Slot Central Baffle	30%	1.3, 1.65, 1.9, 2.35, 2.7, 3	4.8 deg	Water
Slot Central Baffle	50%	1.45, 1.65, 1.85, 2.35, 2.7, 3	4.8 deg	Water
Slot Central Baffle	70%	1.2, 1.4, 1.6, 1.9, 2.35, 3	4.8 deg	Water

Table 2: 2D numerical cases of cylindrical tank

Baffle Type	Filling Level	Excitation Period (s)	Amplitude	Fluid
Without Baffle	30%	1.5, 1.83, 2, 2.5, 3, 3.5	6 deg	Water
Low Central Baffle	30%	1.5,1.83, 2, 2.5, 3, 3.5	6 deg	Water
Without Baffle	30%	1.5, 1.83, 2, 2.5, 3, 3.5	6 deg	LH2
Low Central Baffle	30%	1.5, 1.83, 2, 2.5, 3, 3.5	6 deg	LH2
Without Baffle	30%	1.5, 1.83, 2, 2.5, 3, 3.5	6 deg	LNG
Low Central Baffle	30%	1.5,1.83, 2, 2.5, 3, 3.5	6 deg	LNG

Table 3: Experimental cases of the rectangular tank

Baffle Type	Filling Level	Excitation Period (s)	Amplitude	Fluid
Low central baffle	30%	1.65	4.8 deg	Water
Without baffle	30%	2.35	4.8 deg	Water
Low central baffle	50%	3	4.8 deg	Water
Without baffle	50%	2.35	4.8 deg	Water

Filling levels in this thesis are defined as the height of the fluid inside the tanks. For each filling level, a specific fluid height is assigned as for the rectangular tank, the filling level of 30% equals 7.5cm for 50% equals 12.5cm and for 70% the depth of fluid equals 17.5cm. For the cylindrical tank, the filling level of 30% equals 7.2cm. Table 4 shows the assigned depth for each filling level for both tanks.

Table 4: Assigned fluid depth for each filling level

Tank Type	30% Filling Level	50% Filling Level	70% Filling Level
Rectangular	7.5cm	12.5cm	17.5cm
Cylindrical	7.2cm	-	-

To support the 2D cases, one 3 dimensional (3D) simulation is conducted with the cylindrical tank in this thesis as well. Table 5 shows the specifications of this 3D case.

Table 5: 3D numerical case of cylindrical tank

Baffle Type	Filling Level	Excitation Period (s)	Amplitude	Fluid
Without Baffle	30%	2.5	6 deg	Water

1.6 Literature Review

The thermodynamic response inside the LNG tanks which is accelerated by sloshing is studied in this paper [26]. The main issue studied in this paper is the rapid drop in pressure caused by sloshing intensity which means large motions will accelerate the transport of thermal energy, leading to a rapid drop in pressure. For the experimental part of this article, a pressure tank is made of steel to investigate the thermodynamic response. All tests involve rotation around the bottom center plane of the tank, with a three-degree angle amplitude. To investigate the sloshing characteristics of the transparent tank, a variety of fillings and frequencies are tested. In the hydrodynamic tests, water and air are used, whereas the thermal tank tests used liquid water and vapor with a small amount of air. The numerical models are built through the OpenFoam CFD tool. The RANS turbulence model and VOF method are used to determine which cells contain gas or liquid properties based on the position of the interface. Three grids were compared in order to determine the area of the interface. In conclusion, "the grid independence study indicates that the area can be estimated when the free surface does not break". "The increase of the interface area is approximately 2.5% when the sloshing is closer to a quasi-steady condition"[26]. According to the pressure measurement, the occurrence of the jet causes the pressure to drop in accordance with the sloshing hydrodynamics. Based on simulations with the extended OpenFOAM solver, the results are in good agreement with the measured pressure.

Pressure variations in a cryogenic liquid storage tank subjected to periodic excitation are studied in this article [30]. Experiments have been conducted on the pressure change in a liquid nitrogen tank that is partially filled and subjected to periodic lateral forces. Nitrogen vapor was used to pressurize the tank, when the pressure at sloshing initiation ranged generally around p = 250 kPa. They have measured pressure drops in the order of 100 kPa, and have determined how pressure drops depend on wave amplitude. According to their findings, the pressure drop is often large when sloshing is present, but it rapidly stops. Under the surface of the liquid, a mixed layer has formed that is causing this arrest in pressure drop [30].

Liquid sloshing damping in an accelerated tank using a novel slot-baffle design [19] is the next paper to be investigated. This article investigates the effect of slot baffles to prevent sloshing effect in an accelerated tank which has a baffle design with a gap in the middle that has various uses in engineering. Large amplitude surface waves in a harmonically excited tank are simulated using a second-order accurate numerical model in OpenFOAM. The numerical model testing is done by matching the numerical findings with current experimental tests that shows satisfactory results. The baffle design with various configurations is tested to evaluate the damping performance during the external excitation of the tank. The design shows that it has an effective performance since 88% of the internal kinetic energy of the liquid is dissipated over a certain amount of oscillation (30 in this case). Different slot baffles that are used in a rectangular tank with (a) Slot widths are equal; (b) Slot width is decreasing in the y-direction and (c) Slot width is increasing in the y-direction are shown in the figure below.

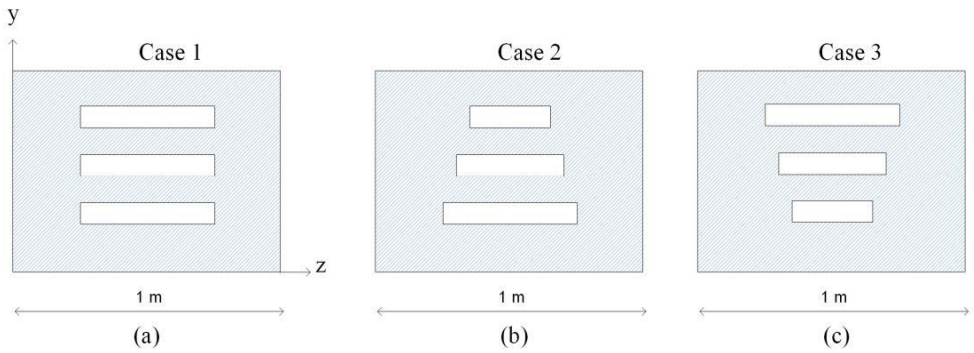

Figure 2: Slot baffle configuration [19]

Next paper is evaluating vertical baffles with different configurations but in an experimental way which is an Experimental study on vertical baffles of different configurations in suppressing sloshing pressure[33]. This article studies 4 different types of baffles including immersed bottom-mounted vertical baffles, vertical baffles flushing with a free surface, surface-piercing bottom-mounted vertical baffles, and perforated vertical baffles(hole in the middle) in a rectangular tank to suppress the sloshing pressure under a wide range of force frequencies.

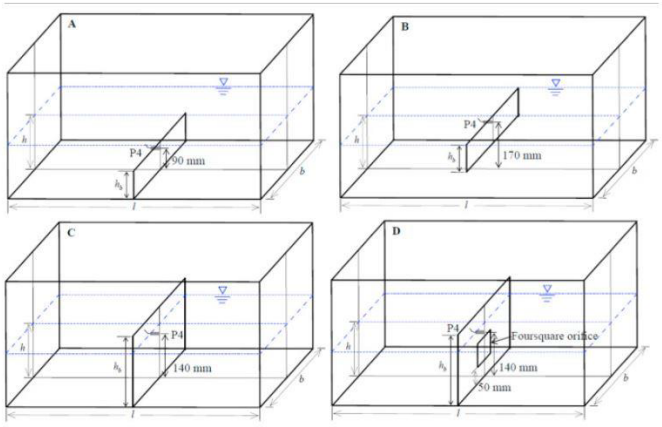

Figure 3: Baffle types [33]

The experimental method equipment consists of a shaker table, a liquid tank, a wave maker, displacement (to record the motion history of the liquid tank), and pressure sensors and cameras.

The shaker table is connected to the wave maker and The irregular wave-maker driven by an electro-hydraulic servo system can generate all kinds of excitation motions such as harmonic motion, random motion related to JONSWAP spectrum[33]. In this study, about 150 experimental tests are done to investigate the pressure distribution on the baffles and the sloshing damping effect on the vertical baffle. The maximum dynamic impact pressure on the tank wall remarkably decreases in low frequency and slightly increases in high frequency with moving the immersed bottom-mounted vertical baffle[33]. It concludes that, in addition to the frequency relation between forcing frequency and natural frequency, the configuration and location of the vertical baffles determine how effective they are at suppressing sloshing pressure. Compared with the immersed bottom-mounted vertical baffle and the surface-piercing bottom-mounted vertical baffle, the vertical baffle flushing with free surface and the perforated vertical baffle can reduce dynamic impact pressure more effectively[33].

In the next study two-phase fluid flow in the 3D model is developed to simulate the sloshing in baffled and non baffled tanks[29]. The tank baffles are designed using the Virtual Boundary Force (VBF) method principle. The 2D sloshing is also done. The results are compared with available results from other literature. The model is first validated against analytical solution and experimental data for 2D sloshing without baffle. Sloshing with small amplitudes produces very good agreement between the numerical results and linear theory. The numerical results diverge from the linear analytical solution for sloshing of large amplitudes. In fact, they correspond well to the experimental data that clearly illustrate nonlinear wave effects. A closer examination reveals that this wave nonlinearity imposes a finite wave amplitude even in the resonant case. A 2D liquid sloshing model is then validated for a tank with a horizontal baffle. The numerical results match very well with the numerical results by Biswal [16]. In addition, the sloshing of liquids in a vertical baffle tank is examined. A vertical baffle reduces sloshing amplitude more effectively than a horizontal baffle. As a result of analyzing pressures and free surface displacements, it was concluded that vertical baffles can also reduce impulse pressure significantly.

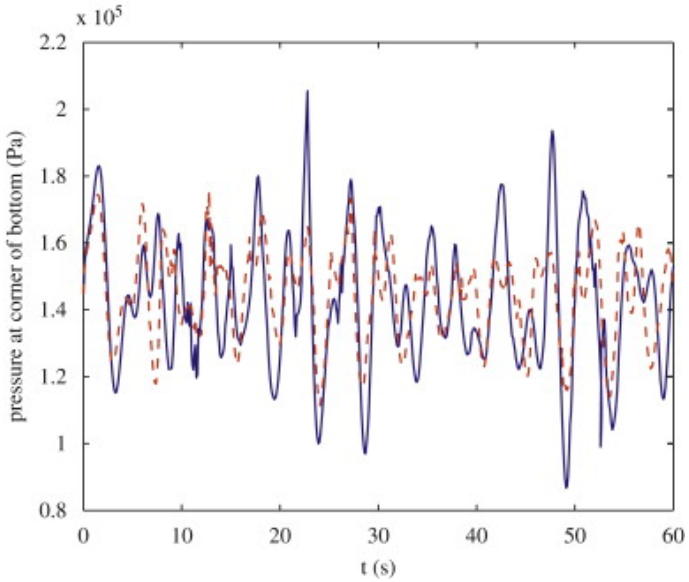

Figure 4: Time histories of pressure at the corner of tank bottom comparisons in the tank with a vertical baffle (dashed line) and without baffle (solid line) [29]

The last paper studies the Experimental and Numerical Investigation of Sloshing in Marine LNG Fuel Tanks [25] which is based on experimental work, analysis, modeling, and simulations, several sloshing tests that investigated with different liquids such as LNG in LNG fuel tanks, liquid Nitrogen, and also water and vapor. The equipment for the experimental part is also designed for hydrodynamic study(transparent tank) and thermodynamic study(steel tank). In this study, the focus is on the thermodynamics of natural gas (LNG) and the natural gas/liquid mixture in moving tanks, which causes a pressure drop and since the pressure drop happened to the fuel tank, it may be necessary to shut down the gas fuel system to avoid further damage. The hydrodynamic sloshing part of the tank can be done with both rectangular and cylindrical tanks. CFD is applied on both tank types with different geometry. The movable platform in this experimental part has one degree of freedom meaning that the tank is rotated with an angle amplitude of 3 degrees around

the bottom center plane of it in all tests. A crank mechanism operated by an electric motor produces the motion. Both rectangular and cylindrical tanks are simulated, but the rectangular tank is being used to validate the CFD analysis and to determine its limitations. A cylinder geometry is almost unexplored in terms of sloshing, but investigations have been conducted to determine sloshing characteristics and prepare thermal experimentation.

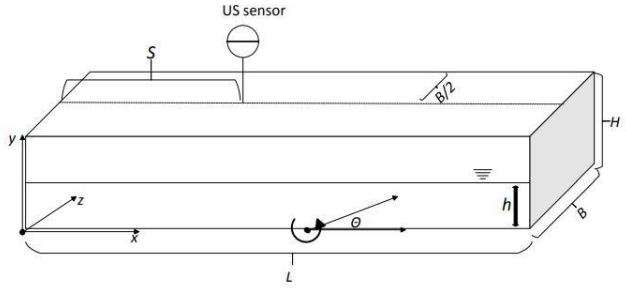

Figure 5: Rectangular tank [25]

In conclusion of this study, sloshing is influenced significantly by the spherical form of tank heads. There is a very good agreement between the free-surface elevation measured in the experiments and the simulations for low filling ."When the tank is low filled, a single wave does not impact the roof regardless of the frequency of motion"[25].

2 Experimental Method

Albeit numerical methods could be considered as accurate methods, all numerical simulations require validations from the relative real cases to be more realistic and trustworthy. In this part, experiments are done based on factors that are explained in the experimental procedure to get the most possible accurate results to validate the CFD results of Sloshing. The experimental rig used to study the sloshing phenomenon and validate the numerical results is explained in the following.

2.1 Experimental Rig

The experimental rig is denoted in Figure 84 (refer to appendix A) and Figure 6 is made by previous NTNU researchers which creates the motion by an electromotor and a crank mechanism connected to the platform's table.

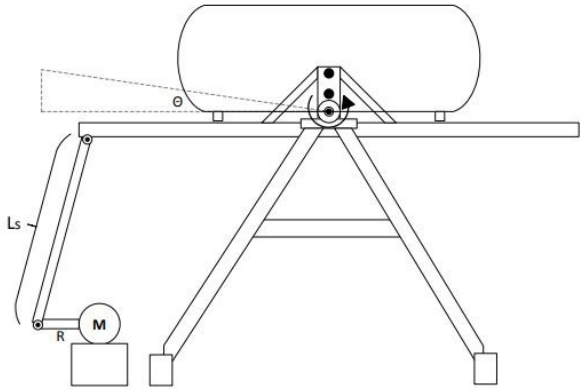

Figure 6: The experimental rig 2D sketch [24]

The platform is able to rotate around the pitch axis with a constant angle amplitude of 4.8 degrees.

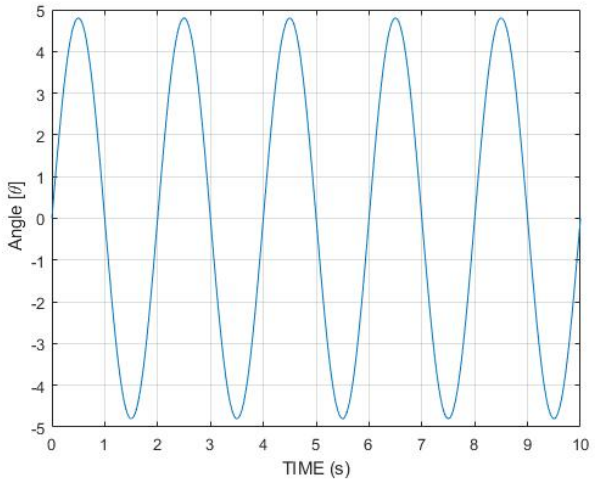

Figure 7: The platform motion angle with an amplitude of 4.8 degrees, period of 2 seconds

The motion is described as sinusoidal form and the displacement can be calculated using a simple harmonic motion equation $d = A \cdot \sin(\omega \cdot t)$. in which A is the amplitude, ω refers to the angular displacement per unit time that can be calculated from the frequency with the equation $\omega = 2.\Pi.f$ and t is time. In addition to a gearbox with a gear ratio of 1:95, the platform is equipped with two sensors used to record the motion angle and force exerted on the crank arm.

2.2 Experimental Procedure

The experimental procedure includes the tank geometry used for getting the experimental results and studying the sloshing characteristics, sensor optimization, zero balance of the platform angle, recording the data obtained from sensors, and video recording to correspond the experimental patterns with CFD simulations. The tank used for the experiment is a rectangular, transparent tank as is shown in Figure 8 with its geometry.

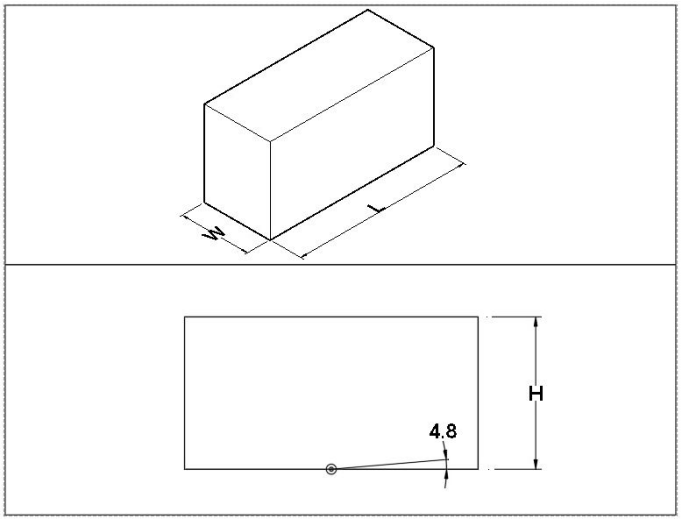

Figure 8: Rectangular tank used for experiments geometry and its rotation amplitude

This tank has a length of 1m (L), a height of 52cm (H), and a width of 40cm (W). The rotation axis is placed in the bottom center of the tank with a height of 2cm from its center to the bottom of the tank. Water is used during the entire experimental process, Firstly, with the empty tank to record the data having the dead weight of the tank and secondly, the filled tank with the specific assigned water level. This is done because in the CFD simulation the weight of the tank is not considered therefore, by subtracting the synchronized empty tank result from the filled tank result it is possible to compare the experimental result with the numerical ones. The camera used for recording to compare the patterns is Sony rx100 vii which is classified as a high fps camera.

3 Theoretical and Numerical Method

3.1 Theoretical Analysis

Conservation laws are the main parts of any fluid problems. The first law is the conservation of mass or continuity equation. The second law is the conservation of momentum which can be calculated using Newton's second law and the momentum equation. The third law is the conservation of energy and it can be calculated using the first law of thermodynamics.

Above mentioned laws state that mass, momentum, and energy in a closed system are constant. Basically, it can be said that the same amount of mass, momentum, and energy entered into the system should leave the system. These three conservation rules can also be used to determine the characteristics of a fluid whose thermal parameters are changing. In fact, by using these three laws, three main parameters of pressure (P), velocity (V), and temperature (T) can be measured therefore, when in the governing equations, pressure and temperature are known as two required thermodynamic independent variables, other fluid properties such as density, enthalpy, viscosity, and thermal conductivity can be expressed in terms of these two parameters of pressure and temperature. Another point to note to start to use the governing equations and the Navier-Stokes equations are the presence of two approaches on "Eulerian" and "Lagrangian" in fluid mechanics. The Lagrangian approach looks at the fluid motion where the observer follows an individual fluid parcel as it moves through space and time [15] [5]. This means that in this case, the initial position of a particle at time t_0 and the final position at time t_1 must be calculated. In fact, The Lagrangian view moves along a fluid particle and follows its path from beginning to end. One of the most important points to note is that the Lagrangian view always has a time-dependent solution. In fact, since this view follows the motion of the fluid particle over time, it can be concluded that this view will always be a function of time.

In the second view, the Eulerian approach is a way of looking at fluid motion that focuses on specific locations in the space through which the fluid flows as time passes [15] [5]. It considers a control volume (CV) and, as an external viewer, studies the particles passing through this CV. In the next section, the conservation of continuity, momentum, and energy equations are explained in a mathematical way.

3.1.1 Governing Equations

Describing fluid motion is possible by a set of partial differential equations named Navier-Stokes equations. This set of equations are named after French engineer Claude-Louis Navier and mathematician George Gabriel Stokes. Navier-Stokes equations represent the conservation of momentum and the conservation of mass mathematically. In fluid dynamics, the continuity equation states that the rate at which mass enters a system is equal to the rate at which mass leaves the system [31] [18]. hence, the balance of mass through a control volume is expressed by the continuity equation as the following equation[12].

$$\frac{\partial \rho}{\partial t} + \nabla \cdot (\rho \mathbf{v}) = 0 \tag{1}$$

Where; ρ is the fluid density, t is time, v is the continuum velocity, and ∇ is the divergence term represents the difference of flow in versus flow out[12].

If the density is constant, the fluid is incompressible and the mass continuity equation simplifies to a volume continuity equation. This means the divergence of the velocity field is zero everywhere.

$$\nabla \cdot v = 0 \tag{2}$$

Conservation of Linear Momentum

The time rate of change of linear momentum is equal to the resultant force acting on the continuum;

$$\frac{\partial(\rho v)}{\partial t} + \nabla \cdot (\rho v \otimes v) = \nabla \cdot \sigma + f_b \tag{3}$$

Where; $\otimes$ denotes the Kronecker product, f_b is the resultant of the body forces (such as gravity and centrifugal forces) per unit volume acting on the continuum, and σ is the stress tensor[12].

For a fluid, the stress tensor is often written as the sum of normal stresses and shear stresses, $\sigma = -\mathrm{pI} + \mathrm{T}$ where p is the pressure and T is the viscous stress tensor[12], giving :

$$\frac{\partial(\rho v)}{\partial t} + \nabla \cdot (\rho v \otimes v) = -\nabla \cdot (pI) + \nabla \cdot T + f_b \tag{4}$$

Conservation of Angular Momentum

The stress tensor must be symmetric in order to maintain angular momentum;

$$\sigma = \sigma^{\mathrm{T}} \tag{5}$$

Conservation of Energy

The conservation of energy can be expressed as follows when the first law of thermodynamics is applied to the control volume;

$$\frac{\partial(\rho E)}{\partial t} + \nabla \cdot (\rho E v) = f_b \cdot v + \nabla \cdot (v \cdot \sigma) - \nabla \cdot q + S_E \tag{6}$$

Where; E is the total energy per unit mass, q is the heat flux, and S_E is an energy source per unit volume[12].

3.2 Numerical Method of Sloshing

As sloshing is considered a severe motion, the turbulence models need to be used to model this phenomenon. Different types of turbulence models are available to users having their own advantages and disadvantages including Direct Numerical Simulation (DNS), Detached Eddy Simulation (DES), Large Eddy Simulation (LES), Reynolds-averaged Navier–Stokes equations (RANS) and etc. The models of LES, DES and RANS are explained in the following.

LES

'Large Eddy Simulation (LES) is an inherently transient technique in which the large scales of the turbulence are directly resolved everywhere in the flow domain, and the small-scale motions are modeled. One justification for the LES technique is that by modeling "less" of the turbulence and explicitly solving for more of it, the error in the turbulence modeling assumptions is not as consequential. Furthermore, it is hypothesized that the smaller eddies are self-similar and thus lend themselves to simpler and more universal models. The downside of the approach is the computational expense, which, although less than direct numerical simulation, is still nonetheless excessive. In contrast to the RANS equations, the equations that are solved for LES are obtained by spatial filtering rather than an averaging process. Each solution variable $\emptyset$ is decomposed into a filtered value $\bar{\emptyset}$ and a sub-filtered, or sub-grid, value $\emptyset'$'[12].

$$\phi = \tilde{\phi} + \phi' \tag{7}$$

Where: $\emptyset$ represents velocity components, pressure, energy, or species concentration[12].

DES

'Detached Eddy Simulation (DES) is a hybrid modeling approach that combines features of Reynolds-Averaged (RANS) simulation in some parts of the flow and Large Eddy Simulation (LES) in others. The unsteady RANS equations are applicable to transient situations where the unsteadiness is either imposed, such as by a time-varying boundary condition, or is inherent, such as the vortex shedding in a massively separated flow. In the latter case, transient simulations often yield better results than attempting to use a steady-state approach. However, successful unsteady RANS simulations require that the time scales of the turbulence be disparate from the mean-flow unsteadiness. Furthermore, the limitations of the turbulence model may preclude good unsteady results. DES turbulence models are set up so that boundary layers and irrotational flow regions are solved using a base RANS closure model. However, the turbulence model is intrinsically modified so that, if the grid is fine enough, it will emulate a basic LES subgrid-scale model in detached flow regions. In this way, one gets the best of both worlds: a RANS simulation in the boundary layers and an LES in the unsteady separated regions'[12]. STAR-CCM+ provides the DES modeling approach for three different RANS models;

- Spalart-Allmaras DES
- Elliptic Blending K-Epsilon DES
- SST K-Omega DES

RANS

'RANS turbulence models provide closure relations for the Reynolds-Averaged Navier-Stokes equations that govern the transport of the mean flow quantities. To obtain the Reynolds-Averaged Navier-Stokes equations, each solution variable $\emptyset$ in the instantaneous Navier-Stokes equations is decomposed into its mean, or averaged Equation7, value $\bar{\varnothing}$ and its fluctuating component $\emptyset'$' [12] .

'The averaging process may be thought of as time-averaging for steady-state situations and ensemble averaging for repeatable transient situations. Inserting the decomposed solution variables into the Navier-Stokes equations results in equations for the mean quantities'[12]. The mean mass and momentum transport equations can be written as;

$$\frac{\partial(\rho)}{\partial t} + \nabla \cdot (\rho \bar{v}) = 0 \tag{8}$$

$$\frac{\partial}{\partial t}(\rho \bar{v}) + \nabla \cdot (\rho \bar{v} \otimes \bar{v}) = -\nabla \cdot \bar{p} I + \nabla \cdot (T + T_t) + f_b \tag{9}$$

Where; ρ is the density, $\bar{v}$ and $\bar{p}$ are the mean velocity and pressure respectively, I is the identity tensor, T is the viscous stress tensor, f_b is the resultant of the body forces (such as gravity and centrifugal forces)[12].

'These equations are essentially identical to the original Navier-Stokes equations except that an additional term now appears in the momentum transport equation. This additional term is a tensor quantity, known as the Reynolds stress tensor, which has the following definition'[12];

$$\mathbf{T}_t = -\rho \begin{pmatrix} \overline{u'u'} & \overline{u'v'} & \overline{u'w'} \\ \overline{u'v'} & \overline{v'v'} & \overline{v'w'} \\ \overline{u'w'} & \overline{v'w'} & \overline{w'w'} \end{pmatrix} \tag{10}$$

where; ρ is the density, u, v , and w are the velocity components[12].

The challenge is thus to model T_t in terms of the mean flow quantities and hence provide closure of the governing equations. Two basic approaches are used in STAR-CCM+;

- Eddy viscosity models
- Reynolds stress transport models

Eddy Viscosity Models

Eddy viscosity models use the concept of a turbulent eddy viscosity μ_t to model the Reynolds stress tensor as a function of mean flow quantities.The most common model is known as the Boussinesq approximation[12].

$$\mathbf{T}_t = 2\mu_t \mathbf{S} - \frac{2}{3}\left(\mu_t \nabla \cdot \overline{\mathbf{v}}\right)\mathbf{I} \tag{11}$$

Where; S is the mean strain rate tensor, $\bar{v}$ is the mean velocity, I is the identity tensor[12].

'While some simpler models rely on the concept of mixing length to model the turbulent viscosity in terms of mean flow quantities (similar to the Smagorinsky Subgrid Scale model used in Large Eddy Simulation (LES)), the eddy viscosity models in STAR-CCM+ solve additional transport equations for scalar quantities that enable the turbulent viscosity μ_t to be derived'[12]. These include the following turbulence models

- Spalart-Allmaras models
- K-Epsilon models
- K-Omega models

'The assumption that the Reynolds stress tensor is linearly proportional to the mean strain rate does not consider the anisotropy of turbulence. In order to account for this turbulence anisotropy, some two-equation models are provided with an option to extend the linear approximation to include non-linear constitutive relations'[12].

Spalart-Allmaras

The Spalart-Allmaras turbulence model is a one-equation model that solves a transport equation for the modified diffusivity $\bar{v}$ in order to determine the turbulent eddy viscosity[12].

K-Epsilon

'The K-Epsilon turbulence model is a two-equation model that solves transport equations for the turbulent kinetic energy K and the turbulent dissipation rate ϵ in order to determine the turbulent eddy viscosity. Various forms of the K-Epsilon model have been in use for a number of decades, and it has become the most widely used model for industrial applications. Since the inception of the K-Epsilon model, there have been countless attempts to improve it. The most significant improvements have been incorporated into STAR-CCM+'[12].

K-Omega

'The K-Omega turbulence model is a two-equation model that solves transport equations for the turbulent kinetic energy K and the specific dissipation rate ω the dissipation rate per unit turbulent kinetic energy in order to determine the turbulent eddy viscosity. One reported advantage of the K-Omega model over the K-Epsilon model is its improved performance for boundary layers under adverse pressure gradients. Perhaps the most significant advantage, however, is that it may be applied throughout the boundary layer, including the viscous-dominated region, without further modification. Furthermore, the standard K-Omega model can be used in this mode without requiring the computation of wall distance. The biggest disadvantage of the K-Omega model, in its original form, is that boundary layer computations are sensitive to the values of ω in the free-stream. This translates into extreme sensitivity to inlet boundary conditions for internal flows, a problem that does not exist for the K-Epsilon models'[12].

3.2.1 Multi-phase Flow

Multi-phase flow is a term that refers to the flow and interaction of several phases within the same system where distinct interfaces exist between the phases. The term 'phase' usually refers to the thermodynamic state of the matter: solid, liquid, or gas[13].

In modeling terms, a phase is defined in broader terms and can be defined as a quantity of matter within a system that has its own physical properties to distinguish it from other phases within the system[12]. For example;

- Liquids of different density
- Bubbles of different size
- Particles of different shape

Multi-phase flow can be classified into two categories;

- Dispersed flows, such as bubbly, droplet, and particle flows
- Stratified flows, such as free surface flows, or annular film flow in pipes

STAR-CCM+ provides the following distinct models to meet the requirements of these two categories of flow.

The Lagrangian Multi-phase Model

'This model solves the equation of motion for representative parcels of the dispersed phase as they pass through the system. It is intended for systems that consist mainly of a single continuous phase carrying a relatively small volume of discrete particles, droplets, or bubbles. It is suited where the interaction of the discrete phase with physical boundaries is important'[12].

The Fluid Film Model

'This model predicts the dynamic characteristics of wall films using boundary layer approximations and assumed velocity and temperature profiles across the depth of the film. Film transport is predicted using thin shells that lie across the surface of solid walls on which the film is formed' [12].

The Discrete Element Model (DEM)

'This model is an extension of the Lagrangian Multi-phase model, but where individual particles are modeled rather than representative parcels, and where inter-particle contact forces are explicitly accounted for'[12].

The Eulerian Multi-phase Mixture Model

'This model is a simplified multi-phase model that can be used to model suspension-like multi-phase flows. In this model, the computational efforts are reduced by assuming the suspension to be a homogeneous single-phase system'[12].

The Multi-phase Segregated Flow Model

'This model is commonly known as the Eulerian Multi-phase model in the literature, but that term has been given a wider significance in STAR-CCM+. The Multi-phase Segregated Fluid model solves conservation equations for mass, momentum, and energy for each phase. Phase interaction models are provided to define the influence that one phase exerts upon another across the interfacial area between them'[12].

The Dispersed Multi-phase Model (DMP)

'This model simulates dispersed phases in an Eulerian manner. The Dispersed Multi-phase model combines aspects of both the Lagrangian Multi-phase (LMP) model and the Segregated (Eulerian) Multi-phase (EMP) models. The DMP model and the Volume of Fluid (VOF) model can be activated in the same simulation' [12].

The Volume of Fluid Model (VOF)

'This model is provided for systems containing two or more immiscible fluid phases, where each phase constitutes a large structure within the system (such as typical free surface flows). This approach captures the movement of the interface between the fluid phases'[12]. The VOF model is explained in the following as it has been used to model the sloshing phenomenon in this research.

The Volume Of Fluid (VOF) Multi-phase model which is often used for marine applications, is a simple multi-phase model. It is suited to simulating flows of several immiscible fluids on numerical grids capable of resolving the interface between the phases of the mixture. The VOF Multi-phase model is used to solve problems involving immiscible fluid mixtures, free surfaces, and phase contact time. In such cases, there is no need for extra modeling of inter-phase interaction, and the model assumes that all phases share velocity, pressure, and temperature fields become a discretization error. The figure below provides an illustration of unsuitable grids (left) and suitable grids (right) for two-phase flows using the VOF model[12].

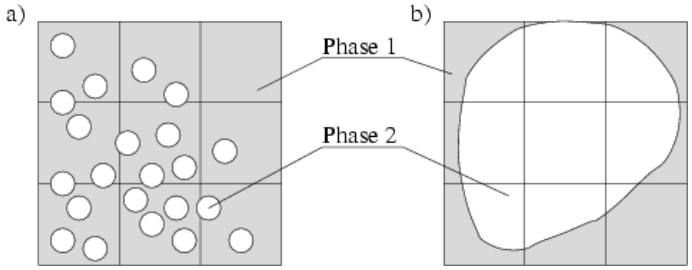

Figure 9: Unsuitable grids (left) and suitable grid (right) for two-phase flows using the VOF model [12]

Due to its numerical efficiency, the model is suited for simulations of flows where each phase constitutes a large structure, with a relatively small total contact area between phases. A good example of this type of flow is sloshing flow in a water tank, where the free surface always remains smooth. If the tank movement becomes pronounced, this results in breaking waves, large numbers of air bubbles in the water, and water droplets in the air[12]. The method would then require a fine mesh (at least three cells across each droplet/bubble) to produce small modeling errors. The spatial distribution of each phase at a given time is defined in terms of a variable that is called the volume fraction. A method of calculating such distributions is to solve a transport equation for the phase volume fraction which is explained in the following as basic VOF model equations[12].

VOF Formulation

The VOF model description assumes that all immiscible fluid phases present in a control volume share velocity, pressure, and temperature fields. Therefore, the same set of basic governing equations describing momentum, mass, and energy transport in a single-phase flow is solved[12].

Basic VOF Model Equations

The equations are solved for an equivalent fluid whose physical properties are calculated as functions of the physical properties of its constituent phases and their volume fractions. The equations are;

$$\rho = \sum_i \rho_i \alpha_i \tag{12}$$

$$\mu = \sum_i \mu_i \alpha_i \tag{13}$$

$$c_p = \sum_i \frac{(c_p)\,\rho_i}{\rho} \alpha_i \tag{14}$$

Where; $\alpha_i = \frac{V_i}{V}$ is the volume fraction and ρ_i, μ_i , and $(C_p)_i$ are the density, molecular viscosity, and specific heat of the i th phase[12].

The conservation equation that describes the transport of volume fractions a_i is;

$$\frac{d}{dt}\int_V \alpha_i dV + \int_S \alpha_i \left(\mathbf{v} - \mathbf{v}_g\right) \cdot d\mathbf{a} = \int_V \left(s_{\alpha_i} - \frac{\alpha_i D\rho_i}{\rho_i}\frac{D\rho}{Dt}\right) dV \tag{15}$$

Where; S_{a_i} is the source or sink of the i th phase, and $\frac{D_{\rho i}}{D_t}$ is the material or Lagrangian derivative of the phase densities ρ_i. If a non-zero sharpening factor (This factor is used to reduce numerical diffusion in the simulation[12]. The valid values are 0.0 through 1.0 when the sharpening factor is set to 0.0, there is no reduction in numerical diffusion is specified, an additional term is added to the VOF transport equation;

$$\nabla \cdot \left(\mathbf{v}_{c_i} \alpha_i \left(1 - \alpha_i\right)\right) \tag{16}$$

Where: a_i is the volume fraction of phase v_{ci} is defined as follows;

$$\mathbf{v}_{c_i} = C_\alpha \times |\mathbf{v}| \frac{\nabla \alpha_i}{|\nabla \alpha_i|} \tag{17}$$

Where; C_a is the sharpening factor that is specified in the VOF node properties, V is the fluid velocity[12].

If there is a large time variation of phase volume fractions a_i , there is a large time variation of the mixture density ρ which features in the continuity equation. Since this unsteady term cannot be linearized in terms of pressure and velocity, it acts as a large source term that can be "unpleasant" for a numerical treatment within a segregated solution algorithm[12]. Therefore, the continuity equation is rearranged in the following, non-conservative form:

$$\int_A \left(\mathbf{v} - \mathbf{v}_g\right) \cdot d\mathbf{a} = \sum_i \int_V \left(s_{\alpha_i} - \frac{\alpha_i}{\rho_i}\frac{D\rho_i}{Dt}\right) dV \tag{18}$$

In the case when phases have constant densities and have no sources, the continuity equation reduces to;

$$\nabla \cdot \mathrm{v} = 0 \tag{19}$$

3.3 Numerical Software

STAR-CCM+ utilized in this master thesis is a commercial computational fluid dynamics (CFD) software first developed by CD-Adapco and then purchased and developed by Siemens Digital Industries Software in 2016[11]. The software is a simulation software capable to solve, modeling, simulate and analyze a broad variety of engineering issues including stress, fluid flow, multi-phase flows, heat transfer, aero-acoustics, particle flows, electrochemistry, and other related problems under real-world conditions. This all-in-one user-friendly package is considered as a multidisciplinary

and affordable software to handle high processing load using features such as CAD modeling, automatic mesh, reliable post-processing section, being able to get authentic results through multiple iterations to fulfill customer's demand and expectations. As a result of a closer look at the program's capabilities in the following chapter, it becomes clear that this software has the potential to solve complicated Fluid Dynamics problems.

4 Numerical Modeling and Simulation of Sloshing

4.1 Numerical Model and Geometry Description

Simulations are done based on the real tank geometry, dimensions, and rotation used for the experimental method therefore, the rectangular tank length (L) is 1m and the height (H) is 52cm. The cylindrical tank model has the dimensions of the length (L) of 64cm and the head radius of 15.6cm for both ends as shown in figure below.

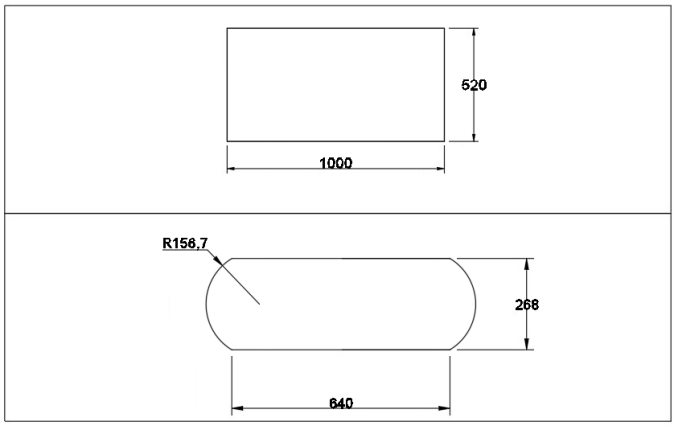

Figure 10: The geometry of simulated rectangular and cylindrical tanks

The models are not imported to the software, all are defined as 2D models in the software using the CAD creator section of STAR-CCM+. Models and parts can be created in this section along with naming the bodies of the models so that analysis can be performed more easily.

4.2 Mesh

To solve the problems the physics solver needs to discretize the domain by using mesh, and since the model is a 2D model after selecting Badge for 2D Meshing to prepare parts for 2D meshing, the Automated Mesh is selected in order to build the actual 2D mesh for the model. CFD requires a suitable high-quality discretized mesh optimized for the volume mesh models therefore, Surface Remesher is selected which can also be used to retriangulate the surface. STAR-CCM+ contains different types of meshing models to build a volume mesh from a suitable surface mesh and since the domains are rectangular and cylindrical in this case needed hexahedral cell shape, a robust, efficient, and high-quality grid for the mesh, the Trimmed Cell Mesher is also selected. To generate the mesh next to the wall surface and boundaries and improve the accuracy of the flow solution as well as allowing the solver to resolve near-wall flow accurately, Prism Layer Mesh is selected with 5 defined layers[12]. To find the best cell size for the mesh, three base sizes are assessed to determine the most accurate at the same time acceptable computational cost. Table 6 shows the comparison between the three different sizes for the rectangular tank.

Table 6: Different base cell sizes comparison

Base Size	Generated Cells	Generated Faces	Generated Vertices	CPU Time(s)	Memory(MB)
0.01m	6220	12283	6378	6	166.63
0.005m	22840	45371	23150	22	183.78
0.0025m	87280	173947	87894	83.14	252.07

The figures below denote the comparison between three simulations based on the different cell sizes presented in Table 6 .

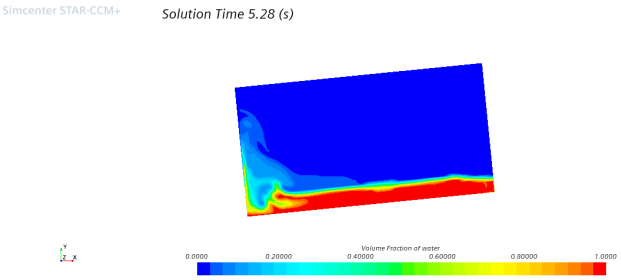

Figure 11: Simulated model utilizing base cell size of 0.01m

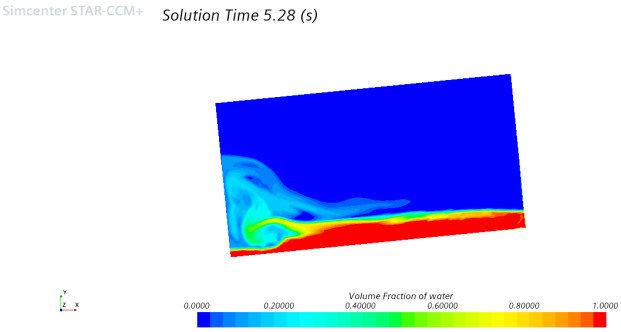

Figure 12: Simulated model utilizing base cell size of 0.005m

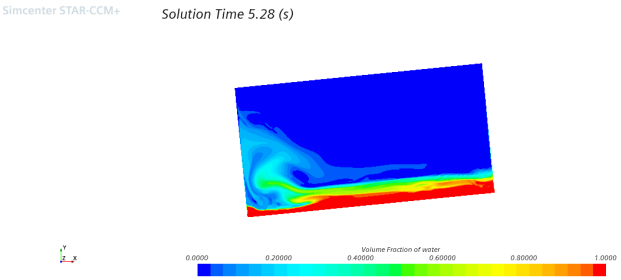

Figure 13: Simulated model utilizing base cell size of 0.0025m

According to this comparison, smaller cells can result in better capturing of the fluid motion but at the expense of increased memory and processing time. Having compared these models, it would make more sense to choose the one offering the most accurate result with an acceptable time and

memory allocation. The second model with the base size of 0.005 and 5 prism layer is the best option to be used for the simulations therefore, this model is selected to be applied in the rest of the simulations for the rectangular tank. The same strategy is applied for the cylindrical tank except for the cell size which is defined as 0.004m.

Figure 14 shows the mesh model and prism layers generated for the rectangular tank. Figures 85 and 86 show the mesh and prism layer model for the cylindrical tank (refer to appendix A).

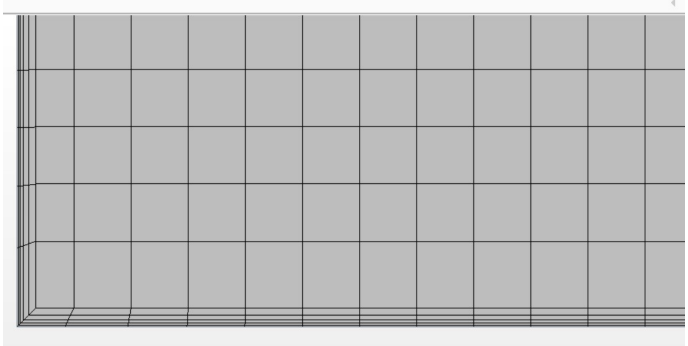

Figure 14: Rectangular tank's mesh and prism layers model

4.3 Numerical Physics Modeling

After the model has meshed the physics of the model should be set for the software. The sloshing model, in this case, is 2D therefore, a Two Dimensional model is selected. Sloshing is considered as a time-dependent flow which means it is a function of time hence, Implicit Unsteady is chosen for the model. Since in the tank there are two phases, Multi-phase is selected to make the VOF activated to be used as the main method for the simulations. To engage the segregated solver the Segregated Flow model is selected for solving each momentum equations in turn, for each dimension. The Turbulent model and after that RANS and K-Omega Turbulence are selected based on the Reynolds number for the Viscous Regime. Wall treatment is set to have an optimal prediction of flow and turbulence parameters across the wall boundary layer therefore, All-Y+ wall treatment is selected. Wall distance is selected automatically and gravitation is applied as an optional selection which is set in Reference Values so that force due to gravity has its impact on momentum balance. The reference pressure is also set in the same section as atmospheric pressure (101325 Pa)[12].

The phases should be defined in the Multi-phase section of the simulation tree hence, water and air are created for the Eulerian phases to set their properties. Similarly, the same approach is applied for the liquid hydrogen and LNG simulations. Since the change of density with pressure and pressure variation are small the phases are considered as incompressible fluids. Likewise, the density and dynamic viscosity for both phases are set as constant considering the room temperature. To predict the interaction of phases that occur on each other, the Phase Interactions must be set for the model, therefore, the VOF-VOF Phase Interaction is selected, and afterward, the primary and secondary phases are defined as water and air respectively. In the Initial Conditions, the Volume Fraction should be defined to set the fluid level of the tank. This should firstly be done by creating two scalar field functions InitialWater and InitialAir to define the filling ratio of the sloshing tank by inputting the specific expression to fill the tank with the water level of 30% (7.5Cm). The procedure is also followed for levels of 50 and 70 percent[12].

4.4 Numerical Boundary Conditions

Boundaries are surfaces in 3D simulations and lines in 2D cases used to define the regions of a model. Boundaries have associated nodes in the simulation tree that let users assign their properties. The rectangular tank lines bordering the region identify the boundaries which are divided into four including down, left, right, and up. Due to the resistance that each of them has, the boundary type is specified as a no-slip wall, which implies all normal and tangential components of the velocity vector must be zero. Having fluid interfaces between two different fluids requires a different type of boundary, which is a free surface boundary. This boundary requires both kinematic and dynamic conditions. Similarly, for the cylindrical tank, all regions are defined as no-slip walls.

4.5 Numerical Motion and Amplitude Description

The motion of the tank is defined as pitch motion and in the 'Motions' section of the simulation tree, the pitch axis is defined in the bottom center of the tank. The motion type is defined as the simple harmonic motion of $d = \mathrm{A} \cdot \sin(\omega \cdot \mathrm{t})$ in which A is the amplitude with 4.8 degrees for rectangular tank cases and 6 degree for cylindrical cases. The motion and the rotation rate for the rectangular tank cases are defined as below.

$$d = \mathrm{A} \cdot \sin(\omega \cdot \mathrm{t}) \tag{20}$$

Where; t is time,

$$d = \left(4.8 \times \frac{\Pi}{180}\right) \cdot \sin\left(\frac{2\Pi}{T} \cdot t\right) \mathrm{rad}$$

$$\frac{dd}{dt} = \left(4.8 \times \frac{\Pi}{180}\right) \cdot \left(\frac{2\Pi}{T}\right) \cdot \cos\left(\frac{2\Pi}{T} \cdot t\right) \mathrm{rad/s}$$

4.6 Numerical Solver

A 0.005s time step with the number of inner iterations of 10 for each time step is used for the implicit unsteady solver, implying that the governing equations are solved step-by-step for each time step. Smaller time steps lead to more accuracy and convergence of results, but will also increase the computational cost and calculation time of the simulation thus, the optimum time step should be chosen to capture all the flow fluctuations while maintaining normal computational cost. In each time step, the governing equations are being solved step-by-step. The volume fraction of water using the line integral report is monitored to get the water surface elevation on a defined plane section indicating the severity of sloshing motion. The plane is specified as a derived part with a 3cm distance from the left side region. Moment, forces, and pressure of the tank are also monitored for different regions to have the relevant reports for comparisons discussions.

4.7 Natural Frequency and Period Estimation

It is necessary to find the natural frequency for a partially filled tank in order to find the most severe sloshing motion and the most critical loads on the tank walls. As the frequency of the tank's motion approaches that of the natural frequency of liquid inside, the motion of liquid causes extreme impact loads on the tank walls. The natural frequency is affected by the level of the liquid in the tank as well as the length and position of the tank thus, it is calculated separately for different filling levels and tank types. This should be noticed that the sloshing phenomenon is nonlinear, so resonance does not arise at the calculated natural frequency precisely, but at a value close to it. According to [21] the empirical formula (Equation21) is used to estimate the natural frequency of the partly filled rectangular tank[17].

$$f_n = \frac{1}{2}\sqrt{\frac{ng \cdot \tanh(n\pi a/b)}{\pi b}} \tag{21}$$

Where; n is frequency mode number, g is the gravity, a is the fluid depth or the level of filling, b is the tank length.

4.7.1 Natural Frequency Estimation for Rectangular Tank With 30% Filling Level

Having the rectangular tank case with 30% of the filling level indicating that the height of the fluid is 0.075m, the natural frequency can be estimated as follows;

$$f_n = \frac{1}{2}\sqrt{\frac{1 \times 9.81. \tanh\left(\frac{1\times 3.14\times 0.075}{1}\right)}{3.14 \times 1}} = 0.4249$$

Having the estimated natural frequency, the natural period T_n can be calculated using Equation22.

$$T_n = \frac{1}{f_n} \tag{22}$$

$$T_n = \frac{1}{f_n} = 2.35 \text{ s}$$

According to the estimated result, to simulate sloshing in the rectangular tank with 30% filling level, the simulation have to be conducted using the period 2.35s as its severe case.

4.7.2 Natural Frequency Estimation for Rectangular Tank With 50% Filling Level

Calculations of the same sort can be made for a rectangular tank with 50% (0.125m) filling level to estimate the natural frequency.

$$f_n = \frac{1}{2}\sqrt{\frac{1 \times 9.81 \cdot \tanh\left(\frac{1\times 3.14\times 0.125}{1}\right)}{3.14 \times 1}} = 0.5401$$

$$T_n = \frac{1}{f_n} = 1.85 \text{ s}$$

As a result, the simulation should be performed at a filling level of 50% and a natural period of 1.85s to get the most intense motion in the tank.

4.7.3 Natural Frequency Estimation for Rectangular Tank With 70% Filling Level

Considering the rectangular tank, the last case is when the filling level is 70% (0.175m). The natural frequency and period are estimated through the following calculations.

$$f_n = \frac{1}{2}\sqrt{\frac{1 \times 9.81 \cdot \tanh\left(\frac{1\times 3.14\times 0.175}{1}\right)}{3.14 \times 1}} = 0.6249$$

$$T_n = \frac{1}{f_n} = 1.6 \text{ s}$$

Accordingly, for the third case with 70% filling level, the period of 1.6s or a value close to this period will give the most severe motion of sloshing.

4.7.4 Natural Frequency Estimation for Cylindrical Tank With 30% Filling Level

Although there is no specific formula to accurately calculate the natural frequency for cylindrical tanks, one method is available to estimate it[21]. Firstly, the ratio of h/2R should be calculated in which h is the filling level and R is the radius of the cylindrical tank heads. By obtaining the ratio, it is possible to derive the frequency parameter γ_n of the frequency mode number for estimating the natural frequency and its natural period [21] [17].

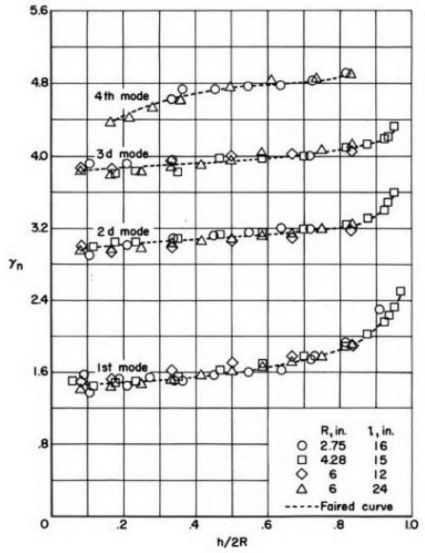

Figure 15: Horizontally positioned cylindrical tank frequency parameter [17] [28]

The ratio h/2R for the a with 30% filling level (0.072m) the radius of 0.156m is 0.2 thus, the frequency parameter of 1.5 can be selected for the 1st mode. The following equation can be used to estimate the frequency ω_n:

$$\omega_n = \gamma_n \cdot \sqrt{\frac{g}{l} \cdot \tanh\left(\frac{n\pi h}{l}\right)} \tag{23}$$

Where; γ_n is the frequency parameter, g is the gravity, l is the length of the tank, h is the filling level, n is the mode number [28] [17]

Therefore the natural frequency for the cylindrical tank with 30% filling level (0.072m) can be estimated using the Equation23

$$1.5 \times \sqrt{\frac{2.81}{0.64} \cdot \tanh\left(\frac{1 \times 3.14 \times 0.072}{0.64}\right)} = 3.4202$$

The natural period can be calculated through Equation24

$$T_n = \frac{2\Pi}{\omega_n} \tag{24}$$

The period T_n now can be calculated as below;

$$T_n = \frac{2\Pi}{\omega_n} = 1.83 \text{ s}$$

Therefore, the most severe motion for the cylindrical tank with 30% filling level should be observed at 1.83s or a value close to it.

4.8 Summary of Chapter

In this chapter, the geometry of the tanks is described. The mesh type and their accuracy are introduced and studied. Furthermore, the 2D model's physics, phase description, as well as rotation type are discussed. After describing the boundary conditions, the motion amplitude, and the solver type, the natural frequencies and periods for each filling level of both tank types (rectangular and cylindrical) are estimated using empirical formulas which can be seen in Table 7.

Table 7: Estimated natural periods using the empirical formulas for rectangular and cylindrical tanks

Tank Type	30% Filling Level	50% Filling Level	70% Filling Level
Rectangular	2.35s	1.85s	1.6s
Cylindrical	1.83s	-	-

5 Results and Discussion

This chapter discusses numerical results from simulations based on different filling levels, tanks, and fluid types. Estimated natural frequencies in chapter 4.7 (refer to Table 7) are used to perform the simulations, additionally, to make sure that the estimated natural frequencies achieved by empirical formulas are accurate enough, close frequencies to the natural frequencies are also simulated. The effects of the different baffle types are investigated and for the validation part, the experimentally obtained results of the rectangular tank are compared to the simulation results of the same cases.The simulation results for the cylindrical tank with and without baffle will be evaluated using water, LNG, and LH2. As the last step, a comparison between the achieved numerical results from the different fluids will be conducted.

5.1 Numerical Simulations of Water in Rectangular Tanks

Water is used as the first fluid to be simulated in this research. This section covers all three filling levels (30%, 50%, 70%)for the rectangular tank to study the natural frequency, the sloshing hydrodynamics forces, and free surface elevation. Table 8 shows the water and air properties at room temperature (22°C) used in the simulation as defined multi-phase.

Table 8: Water and air properties at (22°C)

Fluid Type	Density	Dynamic Viscosity
Water	997.56 kg/m^3	$8.88 * 10^{-4}$ Pa − s
Air	1.18 kg/m^3	$1.85 * 10^{-5}$ Pa − s

5.1.1 Numerical Results of Rectangular Tanks Without Baffle

30% Filling Level

As described in Chapter 4.7.1, based on the 30% filling level, the natural frequency f_n and period T_n were estimated using the empirical formula (Equation21, Equation22)as 0.4249 and 2.35s respectively. Since the formula was used to estimate these values; five other periods (1.3s, 1.65s, 1.9s, 2.7s, 3s) are added to find the most severe forces on the rectangular tank walls. Following is the investigation of cases in which the tank has no baffle installed.

Numerical Results of the Peak Forces on the Left Wall of the Rectangular Tank When no Baffle is Deployed at 30% Filling Level

Based on the calculation, the natural period is 2.35s, but after simulating the added excitation periods, it is observed that sloshing motions are more intense during the period of 1.9s than the other excitation periods, which makes the excitation period of 1.9s the most comparable with the natural period. Figure 16 indicates the measured maximum forces on the left wall of the rectangular tank in different simulated excitation periods.

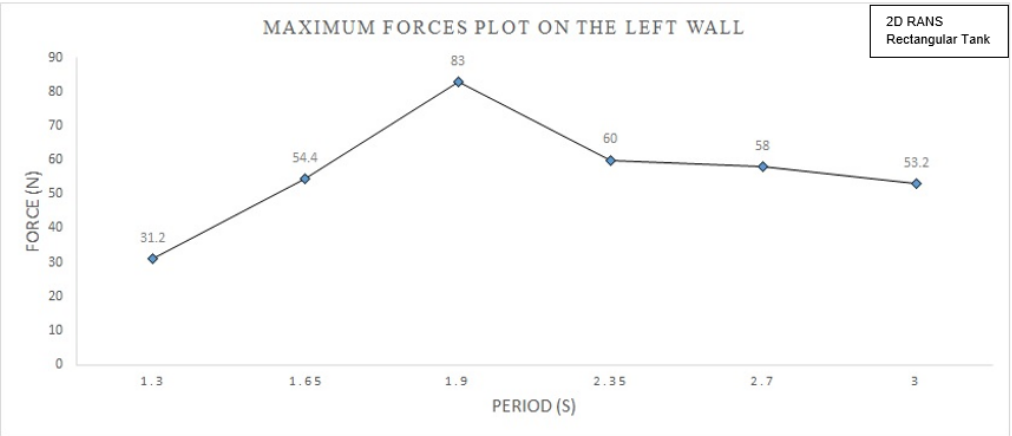

Figure 16: Numerical maximum forces of different simulated excitation periods on the left wall of the rectangular tank filled with water when the filling level is 30% and no baffle is deployed

As the natural period of the system is close to 1.9s, the force monitor diagram on the left wall of the rectangular tank of this excitation period can be investigated exclusively (Figure 17).

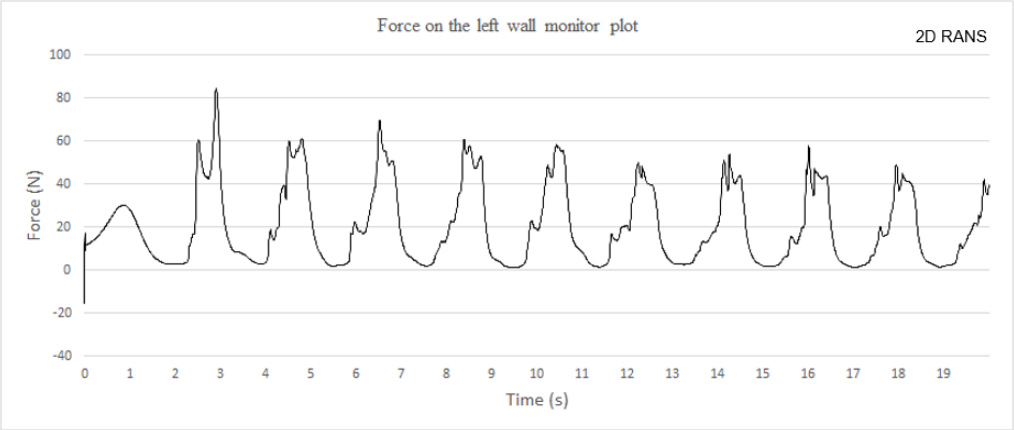

Figure 17: Numerical force monitor plot on the left wall of the rectangular tank at the excitation period of 1.9s when the filling level is 30% with water and no baffle is deployed

As seen in figure 17, the highest force of 83N is applied to the left wall of the rectangular tank at time 2.91s as reflected in the volume fraction of water shot taken at the same time (Figure 18).

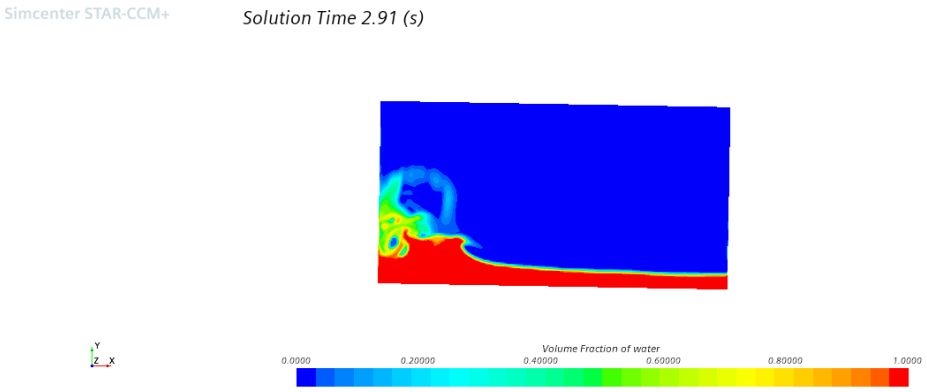

Figure 18: Numerical peak force applied on the left tank wall at time 2.91s over the excitation period of 1.9s, filling level of 30% with water, without baffle

Numerical Results of the Free Surface Elevation Recorded on the Defined Plane Within the Rectangular Tank When no Baffle is Deployed at 30% Filling Level

The free surface elevation on a defined plane explained in chapter 1.4, is also captured using the above-mentioned periods to study the fluid movement and amplitude variation. This is vital to be studied since fluid movements with large amplitudes can impact tank walls and damage the system's stability. Figure 19 illustrates the peak averaged free surface elevations of different excitation periods. As seen in the diagram, the water height on the plane has reached 22 cm when the wave motion at the period of 1.9s is the most severe motion.

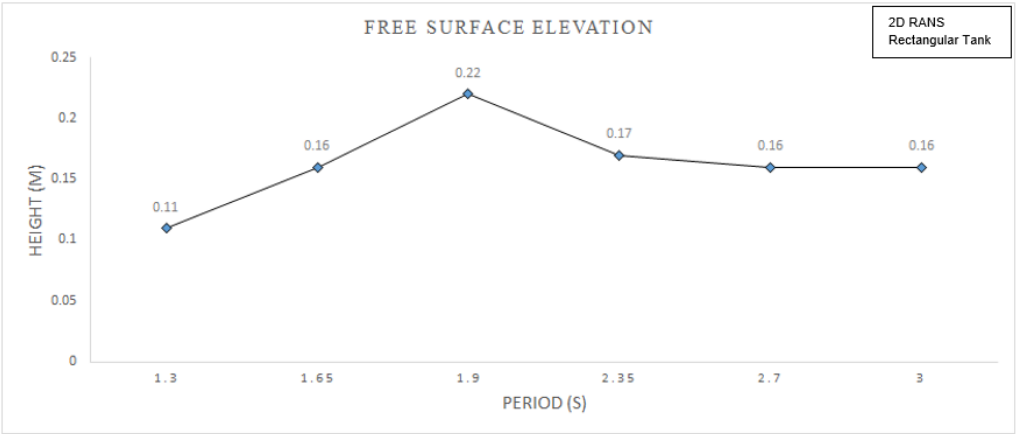

Figure 19: Numerical measured free surface elevation on the defined plane within the rectangular tank over different simulated periods, when the filling level is 30% with water and no baffle is deployed

Figure 20 displays the elevated water surface on the defined plane over the excitation period of 1.9s, reaching a peak of 22cm at a time of 2.81 sec.

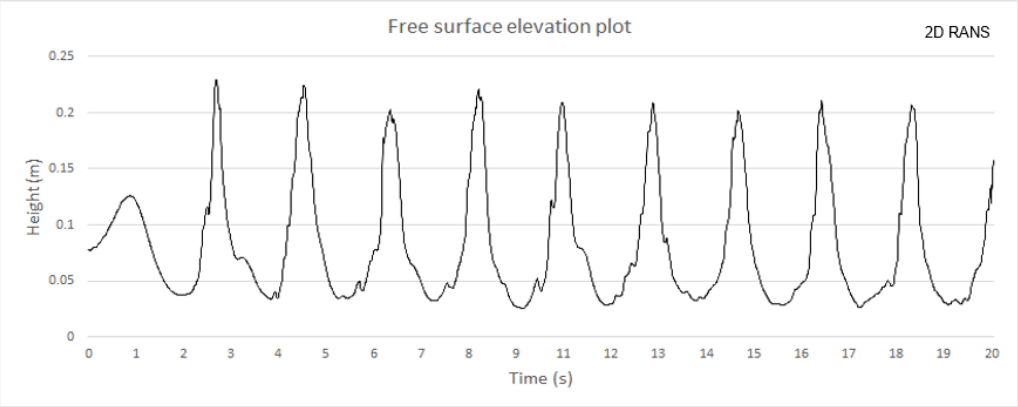

Figure 20: Numerical Free surface elevation on the defined plane within the rectangular tank over the excitation period of 1.9s at 30% filling level of water when no baffle installed

The concentration of water measured on a defined plane reached the maximum amount of 22cm at 2.81 when the free surface elevation shot from the volume fraction is taken (Figure 21).

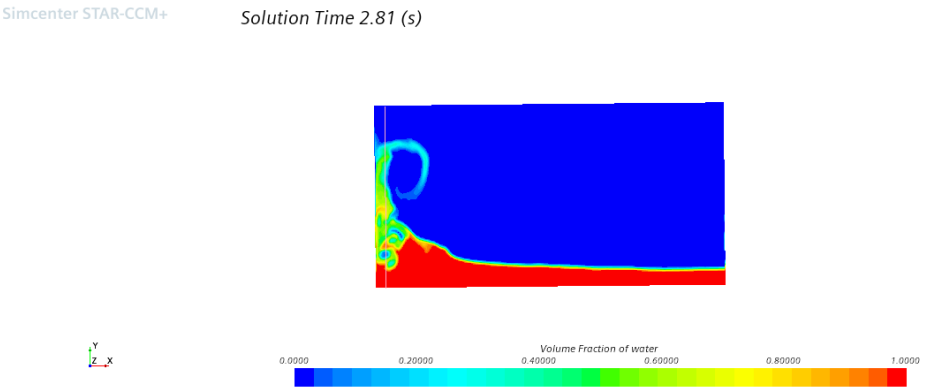

Figure 21: Numerical free surface elevation peak on the plane shot taken at 2.81s over the excitation period of 1.9s, filling level of 30% with water, without baffle

Numerical Results of the Impact Pressure and Pressure Distribution on the Left Wall of the Rectangular Tank When no Baffle is Deployed at 30% Filling Level

The impact pressure is also measured on the same left wall of the rectangular tank at the excitation period of 1.9s as shown in figure 22 the peak of 400Pa is detected.

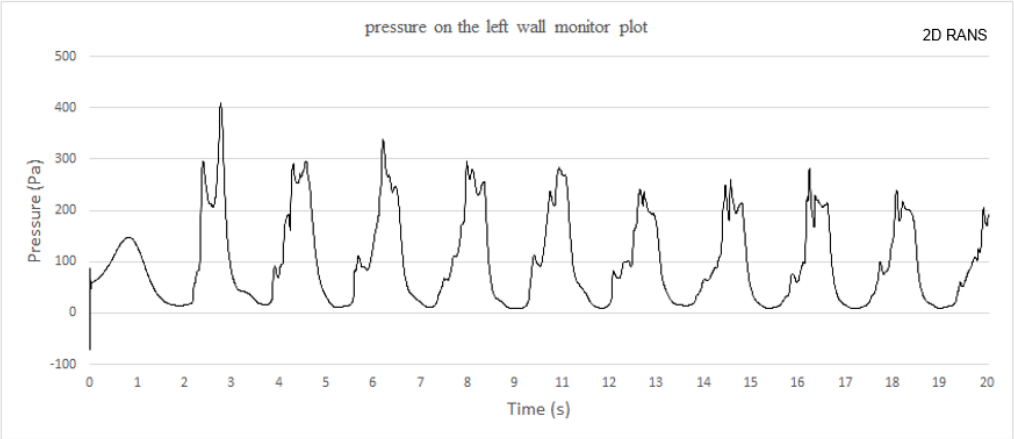

Figure 22: Numerical pressure monitor plot on the left wall of the rectangular tank over the excitation period of 1.9s, filling level of 30% with water and no baffle installed

The pressure distribution at the peak moment of 2.91s shot is also taken and can be seen in figure 23.

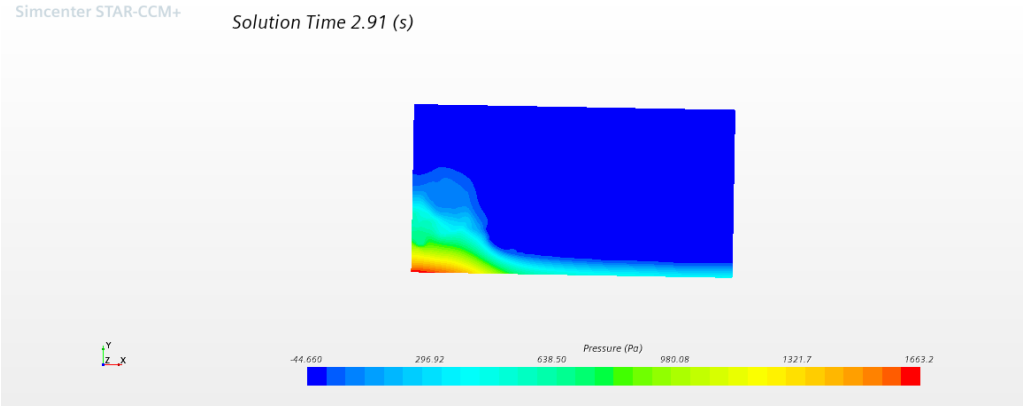

Figure 23: Numerical pressure distribution on the left wall of the rectangular tank at the time of 2.91s over the excitation period of 1.9s, filling level of 30% with water, without baffle

50% Filling Level

In chapter 4.7, the natural frequency $f_n = 0.5401$ and period T_n=1.85s were estimated using the empirical formula (Equation21, Equation22) for the rectangular tank when the filling level is 50%. Water serves as the main fluid, so the material properties remain the same. To test the validity of the natural period estimation, five other periods are added (1.45s, 1.65s, 2.35s, 2.7s, 3s) and simulated.

Numerical Results of the Peak Forces on the Left Wall of the Rectangular Tank When no Baffle is Deployed at 50% Filling Level

Due to the same reasons previously described, the peak forces on the left wall of the rectangular tank with the other added periods are measured for 50% filling level. As Table 9 represents, the peak force on the left wall of the tank occurs when the period is 1.65s with the value of 190.8N,

thus this excitation period is selected as the closest period to the natural period of the tank at 50% of filling level.

Table 9: Numerical maximum forces of different excitation periods on the left wall of the rectangular tank, when the filling level is 50% with water and no baffle is deployed

Excitation Period (s)	Recorded Peak Force (N)
1.45	148.4
1.65	190.8
1.85	154.8
2.35	116.4
2.7	105.08
3	78.08

The peak force has been monitored on the left wall as shown in figure 87 (refer to appendix B) with a value of 190.8N recorded at time 3.89s.

Numerical Results of the Free Surface Elevation Recorded on the Defined Plane Within the Rectangular Tank When no Baffle is Deployed at 50% Filling Level

As before, the free surface elevation on the defined plane within the rectangular tank is captured for all excitation periods which can be seen in Table 10. Based on Table 10, the liquid height reaches 38cm at a period of 1.65s when there is the strongest wave motion.

Table 10: Numerical measured free surface elevation on the defined plane within the rectangular tank over different simulated periods, when the filling level is 50% with water and no baffle is deployed

Excitation Period (s)	Recorded Water Height (m)
1.45	0.28
1.65	0.38
1.85	0.29
2.35	0.23
2.7	0.21
3	0.16

Numerical Results of the Impact Pressure and Pressure Distribution on the Left Wall of the Rectangular Tank When no Baffle is Deployed at 50% Filling Level

The impact pressure is detected with the peak value of 922Pa at time 3.89s as figure 88 shows (refer to appendix B). The pressure distribution at this time is shown in figure 24.

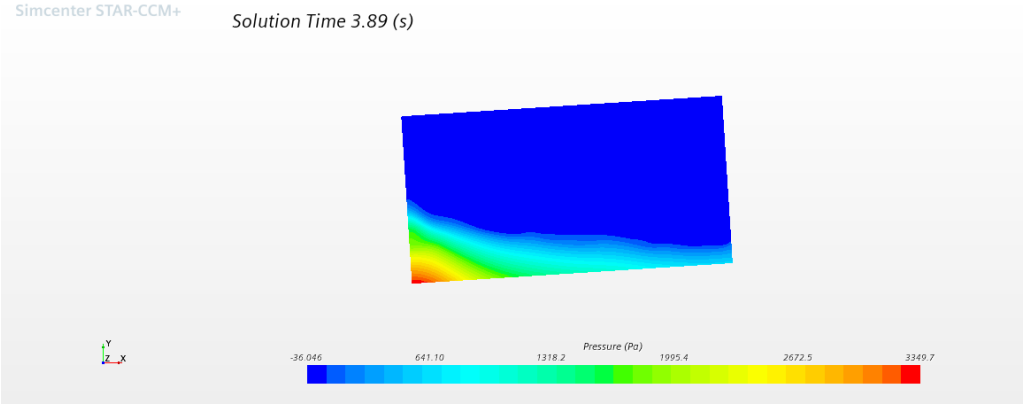

Figure 24: Numerical pressure distribution on the left wall of the rectangular tank at the time of 3.89s over the excitation period of 1.65s, filling level of 50%, without baffle

70% Filling Level

According to chapter 4.7, the natural frequency f_n is equal to 0.6249 and the natural period T_n has been estimated as 1.6s for the tank with 70% filling level. Similar to previous filling levels, five other periods (1.2s, 1.4s, 1.9s, 2.35s, 3s) are added to find the most severe case and the natural period. The fluid properties remain the same as water and air are the defined multi-phase.

Numerical Results of the Peak Forces on the Left Wall of the Rectangular Tank When no Baffle is Deployed at 70% Filling Level

The measured peak forces for each excitation period are shown in Table 11.

Table 11: Numerical maximum forces of different excitation periods on the left wall of the rectangular tank, when the filling level is 70% with water and no baffle is deployed

Excitation Period (s)	Recorded Peak Force (N)
1.2	140.4
1.4	274.6
1.6	328.8
1.9	222
2.35	157.5
3	115.8

Considering that the value 328.8N is the strongest force exerted on the left wall of the rectangular tank, the estimated natural period of 1.6s using the empirical formula (Equation21) is fairly accurate. The force diagram for the excitation period of 1.6 seconds is shown in figure 89 (refer to appendix B), where the force on the left wall reaches its maximum at 3.64 seconds.

Numerical Results of the Free Surface Elevation Recorded on the Defined Plane Within the Rectangular Tank When no Baffle is Deployed at 70% Filling Level

The free surface elevation peak averaged is captured across all of the periods as can be seen in Table 12. As shown in the below table the highest water level recorded on the plane reaches 42cm over the excitation period of 1.6s.

Table 12: Numerical measured free surface elevation on the defined plane within the rectangular tank over different simulated excitation periods, when the filling level is 70% with water and no baffle is deployed

Excitation Period (s)	Recorded Water Height (m)
1.2	0.28
1.4	0.33
1.6	0.42
1.9	0.30
2.35	0.26
3	0.23

Numerical Results of the Impact Pressure and Pressure Distribution on the Left Wall of the Rectangular Tank When no Baffle is Deployed at 70% Filling Level

Figure 90 (refer to appendix B) shows the impact pressure diagram on the left wall with the detected peak of 1500Pa at time 3.64s. Pressure distribution at time 3.64s is shown in figure 25

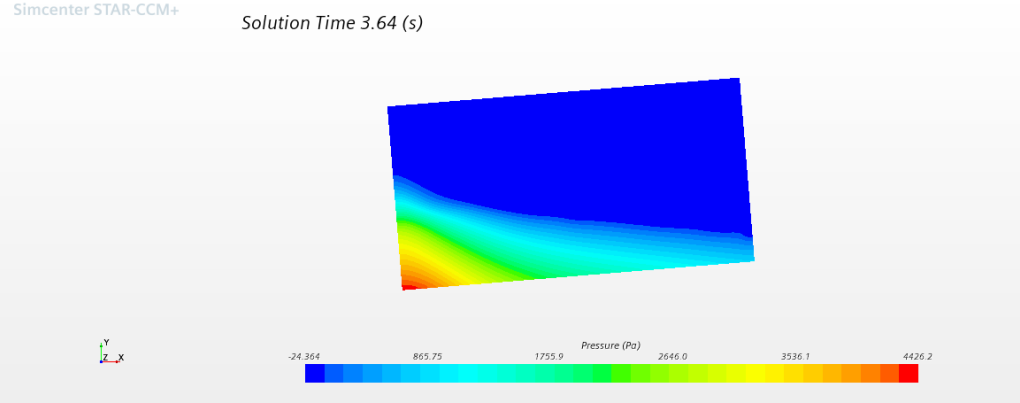

Figure 25: Numerical Pressure distribution on the left wall of the rectangular tank at the time of 3.64s over the excitation period of 1.6s, filling level of 70% with water, without baffle

5.1.2 Numerical Results of Baffle Effect on Rectangular Tanks

There is a possibility of suppressing the impact forces and intensity of the sloshing motion to some extent. One method involves the use of inner structural elements within the tank. For this purpose, baffles can be deployed inside the tank. In order to demonstrate how efficient this method is, in this chapter, the results of the rectangular tank's simulations with baffles will be compared to those of the tanks with no baffles which were discussed previously. Thus two different central baffle types including the low central baffle and slot central baffle are studied numerically in the following.

Baffle Geometry

- 2D low central baffle

  The low central baffle is used for the rectangular tank that is placed in the center which means the tank is divided into two equal halves, covered the whole width of the tank, has a height of 5.5 cm, and a thickness of 6 mm. The rectangular tank is shown in figure 26 which shows the low central baffle's geometry and position.

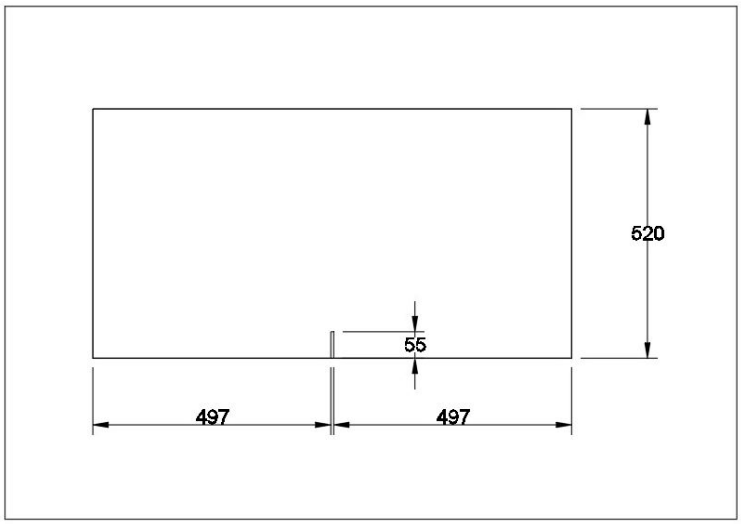

Figure 26: Low central baffle position and geometry in the rectangular tank

- 2D slot central baffle

  Besides the Low central Baffle previously described, another type of baffle is designed to be mounted in the rectangular tank. A slot central baffle is developed to be placed in the center of the rectangle tank to analyze the fluid behavior and its effect on the severity of the sloshing using the same excitation motion modification as non baffle ones. Figure 27 illustrates the geometry of the slot baffle.

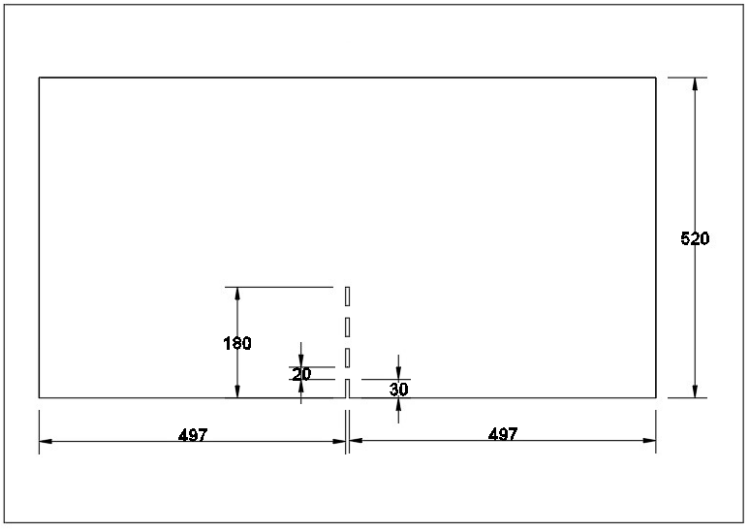

Figure 27: The slot central baffle geometry and position in the rectangular tank

30% filling level

For the baffled cases, simulations are performed using the same excitation periods that have been simulated for the non baffle cases to compare the efficiency of the designed baffle, thus 6 excitation periods (1.3s, 1.65s, 1.9s, 2.35s, 2.7s, 3s) are used in which, 1.9s is the natural period. Figure 28 shows the comparison of the peak forces exerted on the left wall of the rectangular tank between, low baffled, non baffled, and slot baffle cases. The comparison when the low baffle is installed within the rectangular tank clearly shows a reduction of peak forces on the left tank wall. A reduction of 34.4% $\left(\frac{83-54.4}{83}\right)$ in the peak force is noticeable over the natural period of 1.9s. Despite the fact that

the shape of the slot baffle has changed the natural period of the system, as can be seen in figure 28, there is a significant decrease in the peak forces exerted on the left wall of the rectangular tank when the slot baffle is installed. As the below diagram shows, a notable decrease can be observed between the case with a slot baffle and the non-baffle case over the excitation period of 1.9s, showing a reduction percentage of around 56% $\left(\frac{83-36.5}{83}\right)$.

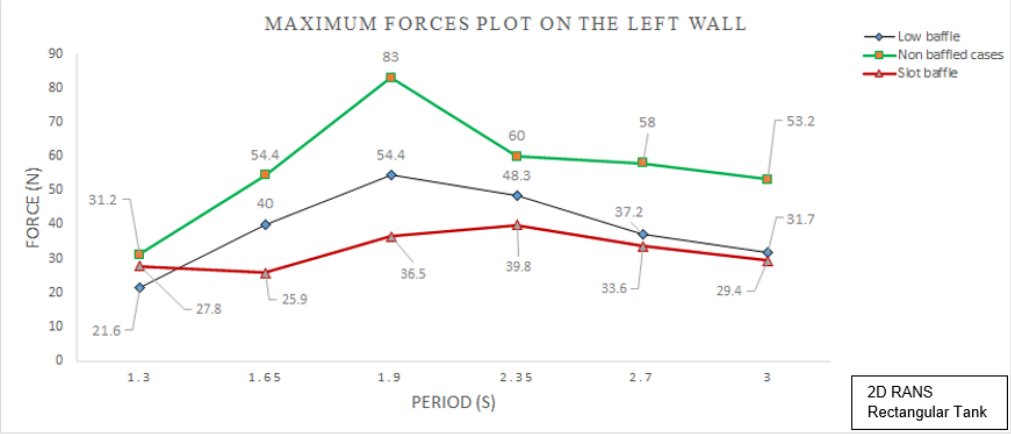

Figure 28: Numerical comparison of the maximum imposed forces on the rectangular tank's left wall between low baffled, slot baffled, and non baffle cases at 30% filling level with water

The natural period of 1.9s is selected to be compared in these three cases thus the applied force on the left tank wall between all these cases diagram over this excitation period can be compared as below (Figure 29).

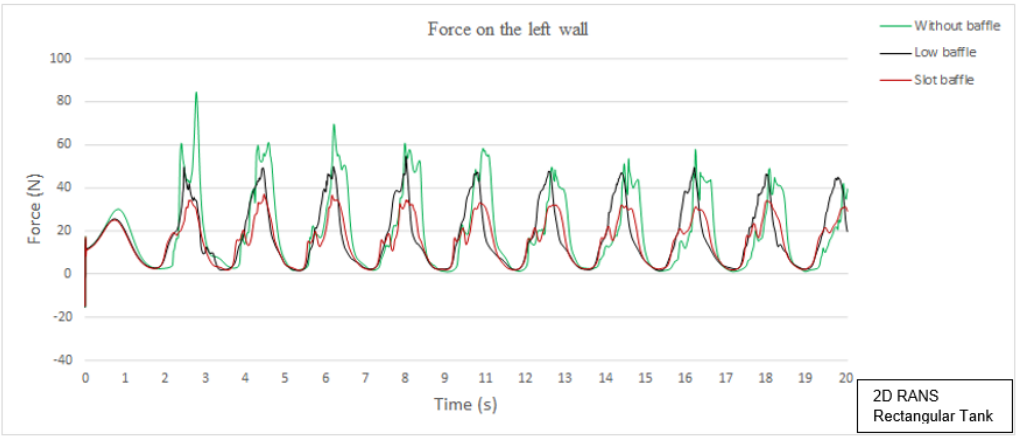

Figure 29: Numerical comparison between imposed forces on the left wall of the rectangular tank over the excitation period of 1.9s between low, slot, and non baffle cases at 30% filling level with water

The free surface elevation can also be compared between the baffled and non baffle cases to show the intensity of the wave motion. As can be seen in figure 30, the height of the water recorded on the plane has dropped from 22cm in the non-baffled case over the natural period of 1.9s to 15cm when the low baffle is deployed. Over the same excitation period, the water level has undergone a considerable drop from 22cm to 13cm comparing the non-baffled case to the slot baffle one.

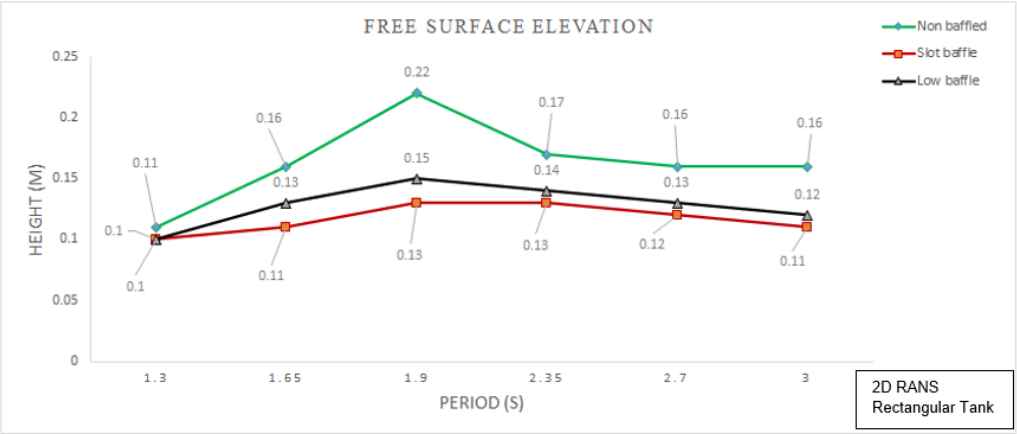

Figure 30: Numerical comparison of the free surface elevation measured on the defined plane within the rectangular tank for low baffled, slot baffled, and non baffle cases at 30% filling level with water

The graph below compares the measured water levels on the plane for all three cases over the period of 1.9s (Figure 31). The below graph also shows, in addition to reducing the water height, the fluctuations in the wave movement have also been decreased.

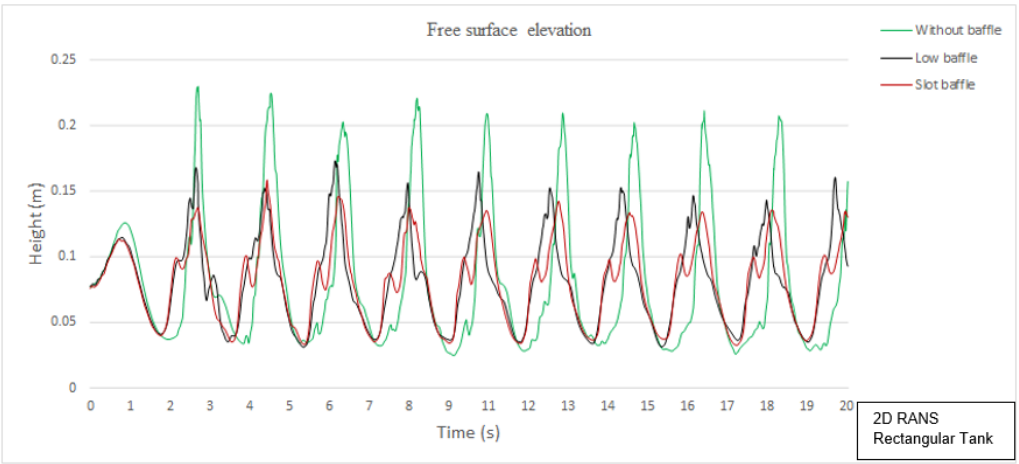

Figure 31: Numerical comparison of recorded levels of water on the defined plane within the rectangular tank between baffled and non baffle cases over the excitation period of 1.9s at 30% filling level with water

50% filling level

The same excitation periods (1.45s, 1.65s, 1.85s, 2.35s, 2.7s, 3s) as those used for non-baffled cases are used to have the comparison between all baffled and non baffle cases for the filling level of 50%. Figure 32 shows the numerical comparison of the peak forces exerted on the left wall between non baffle, low baffled, and slot baffled cases for all the mentioned periods. As can be seen, comparing the non-baffle and low baffle cases, a drop of 46.4% $\left(\frac{190.8-102.1}{190.8}\right)$ is shown in the applied peak forces on the left tank wall over the natural period of 1.65s. The below diagram also shows the maximum reduction of 59.5% $\left(\frac{190.8-77.2}{190.8}\right)$ has occurred over the same period of 1.65s between the non-baffled case and the slot baffled one.

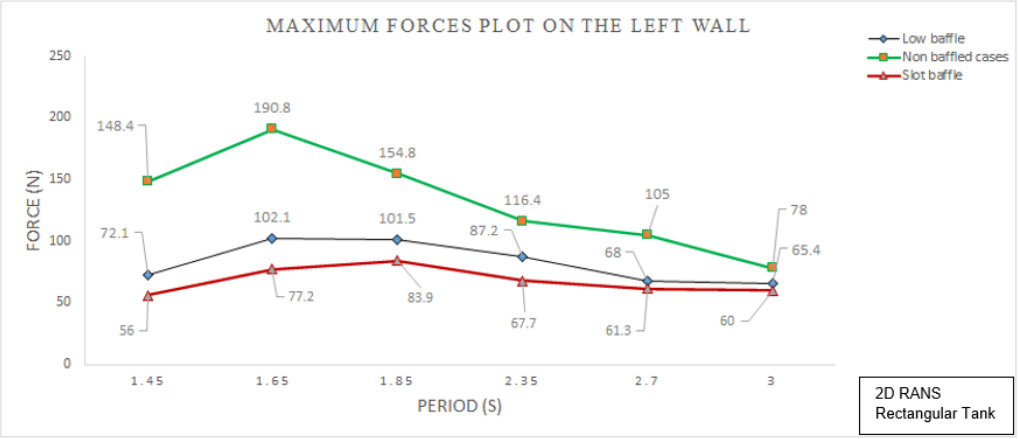

Figure 32: Numerical comparison of the maximum imposed forces on the rectangular tank's left wall between low baffled, slot baffled, and non baffle cases at 50% filling level with water

The comparison of exerted forces on the left wall of the rectangular tank over the excitation period of 1.65s between all the baffled and non baffle cases is shown in figure 33. In addition to the reduction of the value of the imposed forces, the slot baffle shows a more uniform distribution of forces on the tank wall which is approximately 77N.

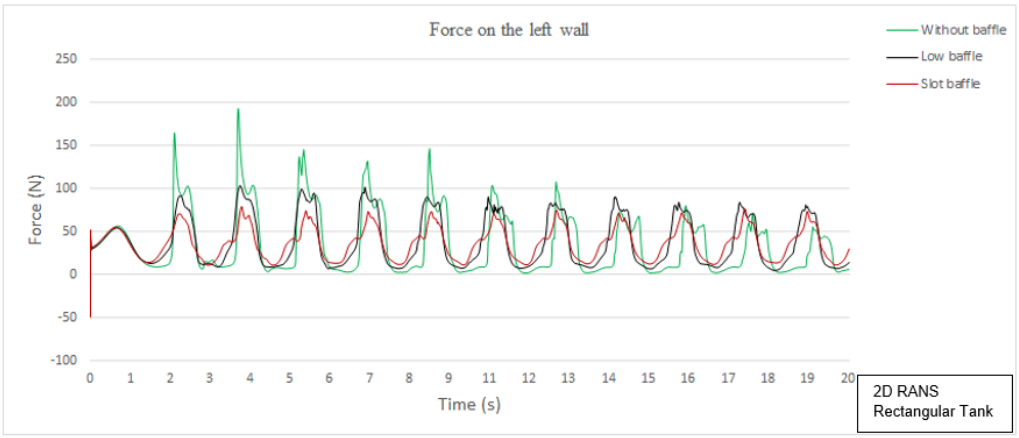

Figure 33: Numerical comparison between imposed forces on the left wall of the rectangular tank over the excitation period of 1.65s between low, slot, and non baffle cases at 50% filling level with water

Figure 34 compares the free surface elevation for the low baffle, slot baffle, and non baffle cases over selected periods. The diagram shows that the most decrease in the recorded water level has occurred over the period of 1.65s. A drop of 36.8% $\left(\frac{38-24}{38}\right)$ can be seen in the recorded water level comparison between non-baffled and low baffle cases over this period. As well as a reduction of 47.3% $\left(\frac{38-20}{38}\right)$ when the non-baffled case is compared with the slot baffle one.

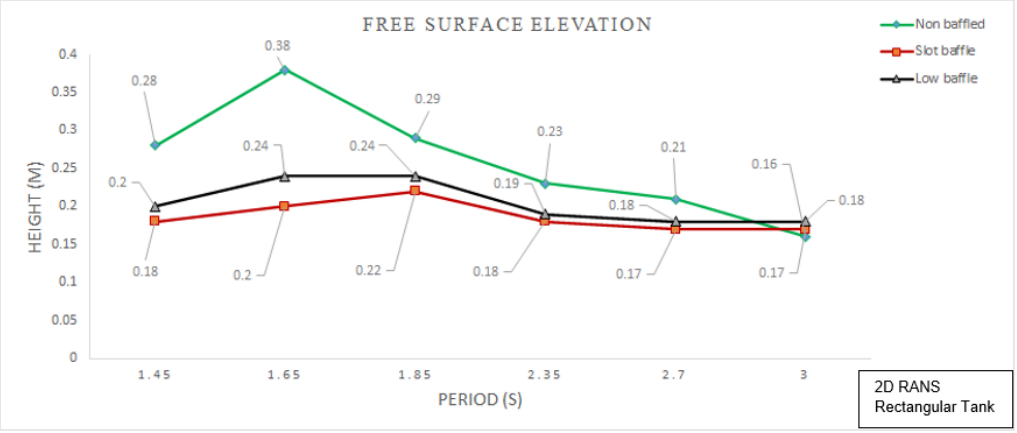

Figure 34: Numerical comparison of the free surface elevation measured on the defined plane within the rectangular tank for low baffled, slot baffled, and non baffle cases at 50% filling level with water

Figure 35 shows the comparison of the free surface elevation between the baffled and non baffle cases over the natural period of 1.65s.

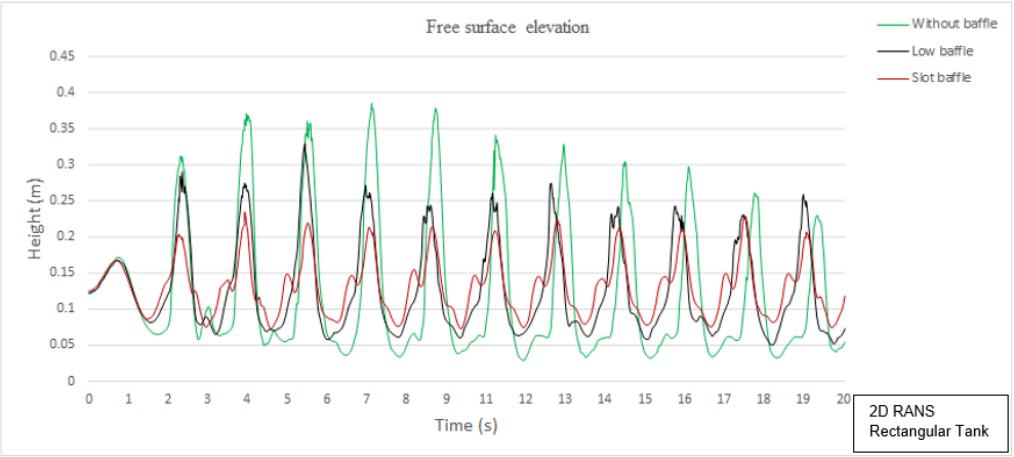

Figure 35: Numerical comparison of recorded levels of water on the defined plane within the rectangular tank between baffled and non baffle cases over the excitation period of 1.65s at 50% filling level with water

70% filling level

The same excitation periods (1.2s, 1.4s, 1.6s, 1.9s, 2.35s, 3s) are simulated as they were for non baffle cases for 70% of the filling level of the rectangular tank. Figure 36 illustrates the peak forces applied on the left wall of the rectangular tank, for low, slot, and non baffle cases. As the below figure shows over the natural period 1.6s, the reduction percentage of the peak force is around 42% $\left(\frac{328.8-190.4}{328.8}\right)$ when the comparison is between non-baffled and low baffle cases. As can also be seen in the below diagram, comparing the peak forces for the non-baffle and slot baffle cases a significant reduction of 52.1% $\left(\frac{328.8-157.2}{328.8}\right)$ has occurred over the period of 1.6s.

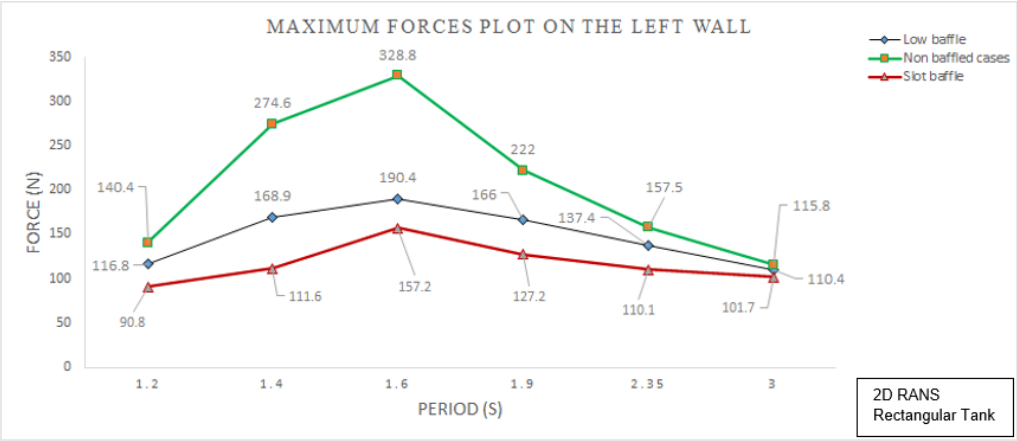

Figure 36: Numerical comparison of the maximum imposed forces on the rectangular tank's left wall between low baffled, slot baffled, and non baffle cases at 70% filling level with water

The force diagram on the left tank wall for all baffled and non-baffle cases over the period of 1.6s can be seen in figure 37.

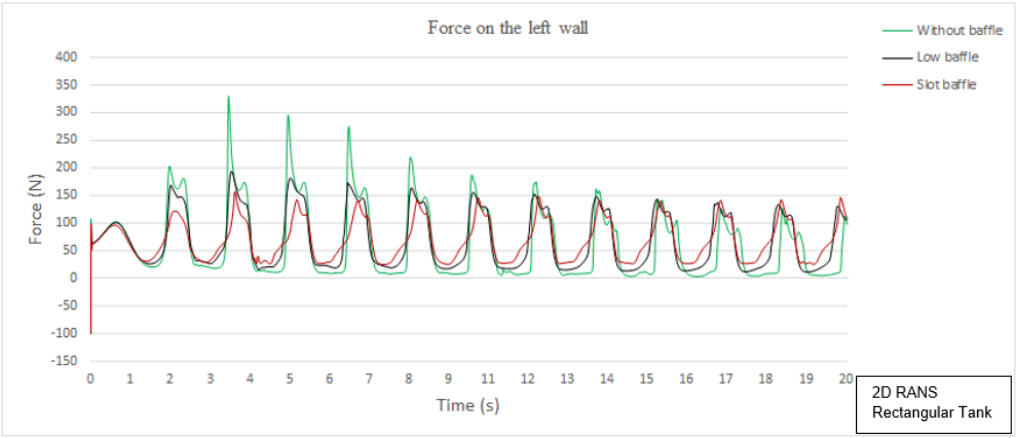

Figure 37: Numerical comparison between imposed forces on the left wall of the rectangular tank over the excitation period of 1.6s between low, slot, and non baffle cases at 70% filling level with water

The free surface elevation graph for all baffled and non baffle cases and all periods are shown in figure 38. According to the below figure, the water level recorded on the defined plane is lowered from 42cm to 36cm showing a reduction of 14.2% when the comparison is between the non-baffled and low baffle cases over the excitation period of 1.6s. The maximum drop occurs over this excitation period when the water level decreases from 42cm to 31cm comparing the non baffled case with the slot baffle one which shows a drop of 26.19%. As can also be seen, during excitation periods other than the natural period of 1.6s, the water level does not change significantly.

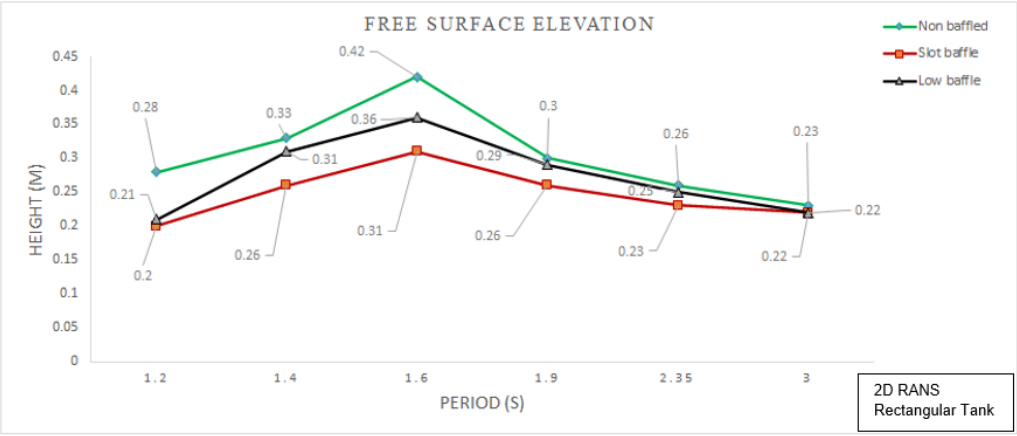

Figure 38: Numerical comparison of the free surface elevation measured on the defined plane within the rectangular tank for low baffled, slot baffled, and non baffle cases at 70% filling level with water

Figure 39 shows the water surface elevation for baffled and non baffle cases over the period of 1.6s where the highest decline occurs.

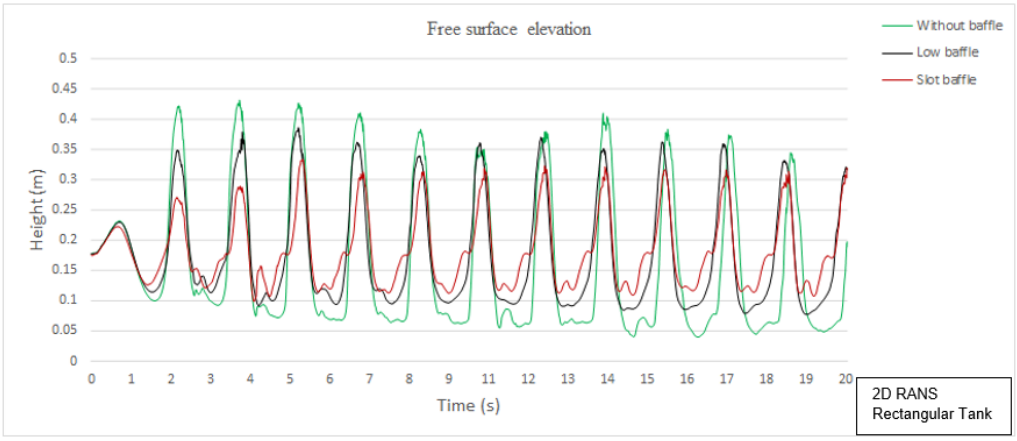

Figure 39: Numerical comparison of recorded levels of water on the defined plane within the rectangular tank between baffled and non baffle cases over the excitation period of 1.6s at 70% filling level with water

5.2 Experimental Results and Validations

For the experimental part, two cases from each filling level of 30 and 50% are selected to validate the numerical result. The experiments are only implemented using the transparent rectangular tank filled with water to record the moment force and motion patterns to compare them with the numerical result. Refer to Table 13 for details of the selected cases.

Table 13: Experimental cases with water

Case number	Filling level	Excitation period (s)	Baffle type
1	30%	1.65	Low central baffle
2	30%	2.35	Without baffle
3	50%	3	Low central baffle
4	50%	2.35	Without baffle

5.2.1 Experimental Results of Case 1

In case 1, the filling level is 30% (7.5cm), the excitation period is 1.65s and the low baffle is installed within the tank. Figure 40 denotes the empty tank result for this period. According to the below figure, the moment force is measured with the arm distance of 0.5m which is the rotation axis position in the bottom center of the rectangular tank for the empty tank during the period of 1.65 which shows the value of about 15Nm.

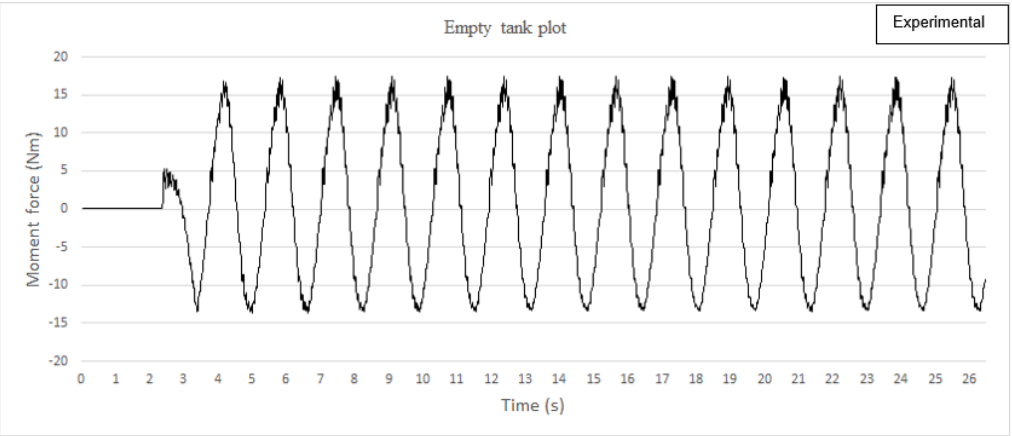

Figure 40: Experimental empty rectangular tank moment force over the excitation period of 1.65s

The next step is to fill the tank with water for 30% (7.5cm). As with the empty tank, the force sensor is zero balanced to sense and record the moment force data. The filled tank plot shown in figure 41 displays a value of around 30Nm.

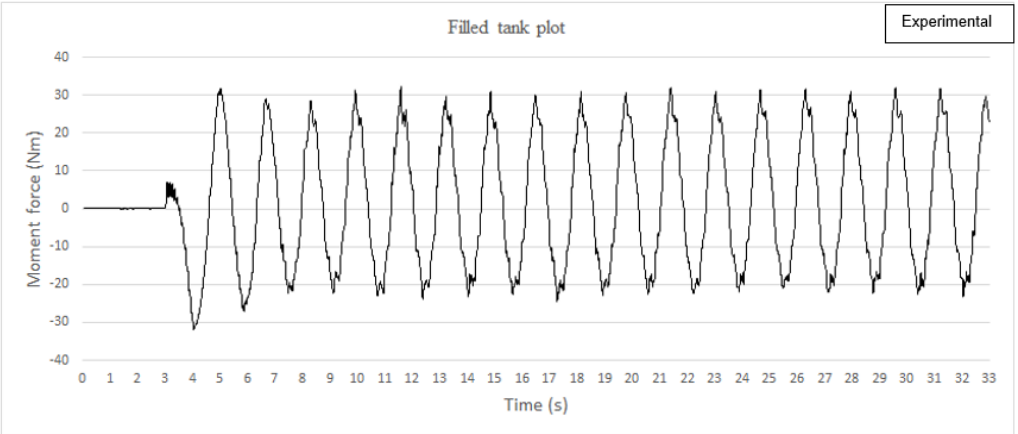

Figure 41: Experimental filled tank moment force over the excitation period of 1.65s, 30% water level, low central baffle installed

To compare the experimental result with the numerical one, the filled tank result should be subtracted from the empty tank result to have the pure fluid effect as figure 42 shows.

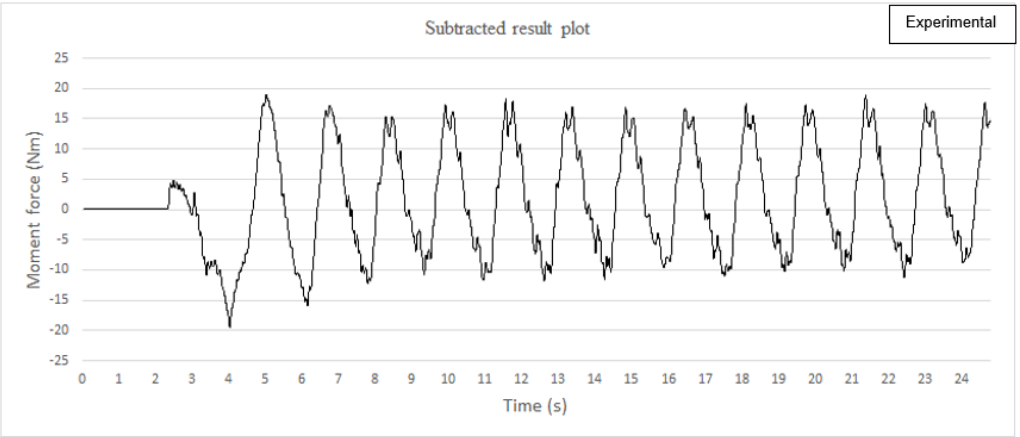

Figure 42: Experimental result of subtracted moment force graph over the excitation period of 1.65s, 30% water level, low central baffle installed

Figure 43 illustrates the comparison of the numerical and experimental results. Comparing the numerical and experimental results in the below figure, it appears that the numerical result and the experimental result show a difference of approximately 10Nm, where the experimental result shows a moment force of 15Nm, and the numerical result displays a moment force of 25Nm.

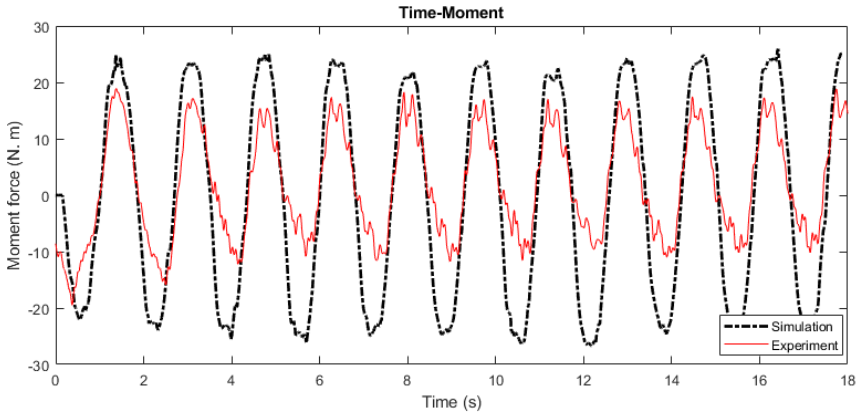

Figure 43: Numerical and experimental moment forces comparison of case 1 with the excitation period of 1.65s, 30% filling level with water, with low central baffle

The numerical results can also be validated by corresponding the camera shots which are taken during the experimental part with the numerical patterns of the volume fraction of water. Figure 44 compares the patterns from simulation and experiment that show a good agreement between them.

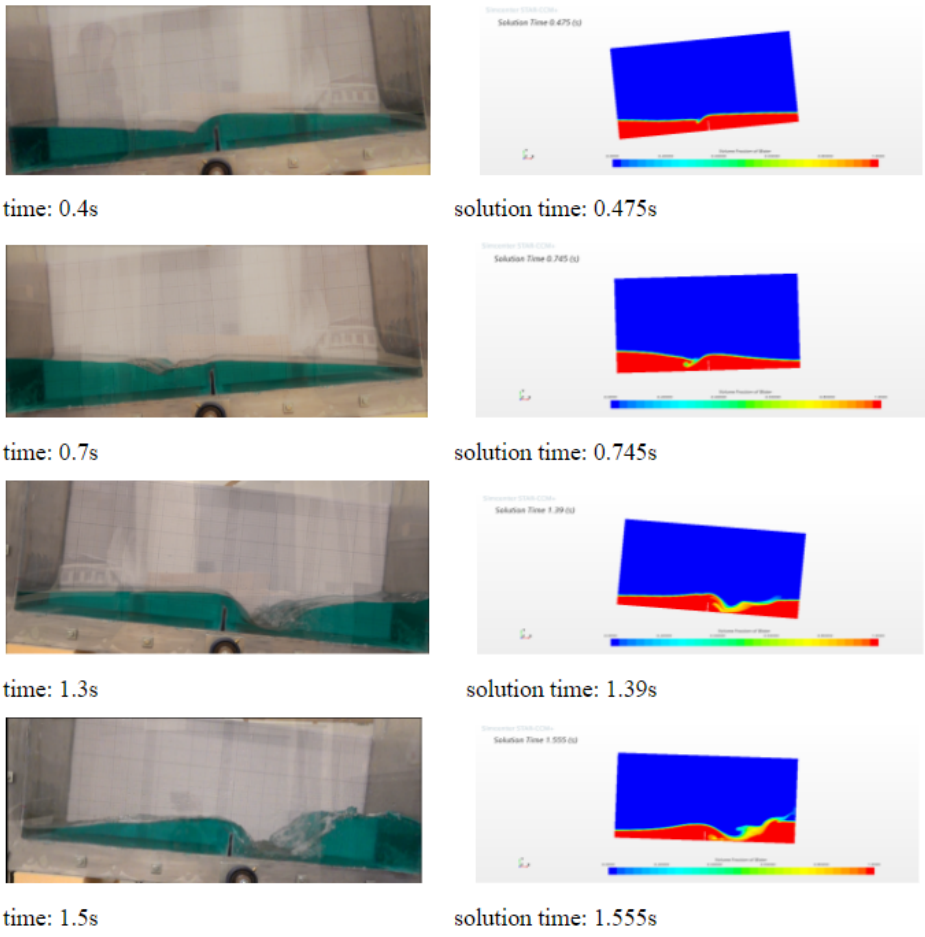

Figure 44: Correspondence between experimental and numerical patterns shots for case 1

5.2.2 Experimental Results of Case 2

In case number 2 the rectangular tank with no baffle is filled with 30% (7.5cm) using the excitation period of 2.35s. Firstly the empty tank moment force result is measured showing the average of 10Nm for case 2 as figure 91 (refer to appendix B) shows. Figure 92 (refer to appendix B) represents the experimentally recorded moment force for the filled tank with the value of 60Nm. The value for the moment force after subtraction of filled tank from empty one is around 50Nm as Figure 93 (refer to appendix B) displays. The simulation and experimental results are compared in figure 45. As the recorded moment force for the numerical and experimental results differs by around 15%, the numerical and experimental results are comparable.

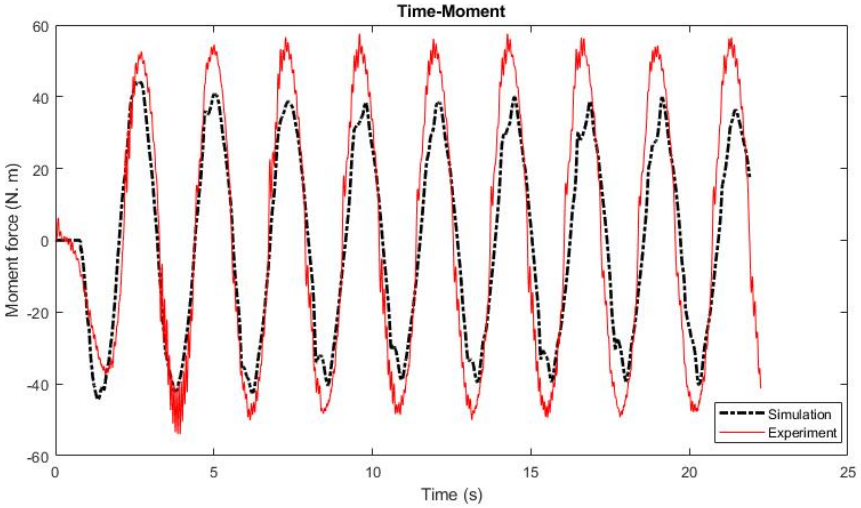

Figure 45: Numerical and experimental moment forces comparison of case 2 with the period of 2.35s, 30% filling level, without baffle

5.2.3 Experimental Results of Case 3

In case 3 the low central baffle is installed within the tank, the excitation period is set to 3s, and the tank is filled by 50% (12.5cm). The empty tank result is plotted in figure 94 (refer to appendix B). According to figure 94, the moment force recorded for the empty tank with the excitation period of 3 is around 8Nm. According to the results from the filled tank, the recorded moment force is around 58Nm, which can be seen in Figure 95 (refer to appendix B). In figure 96 (refer to appendix B) the subtracted filled tank from the empty tank result can be seen, in which the moment force appears to be around 50Nm. For case 3, the numerical and experimental results show a difference of less than 10Nm (Figure 46).

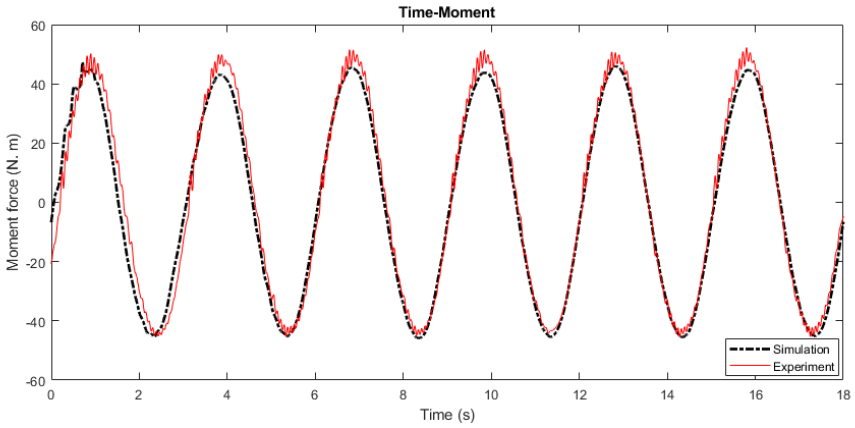

Figure 46: Numerical and experimental moment forces comparison of case 3 with the excitation period of 3s, 50% filling level, with low central baffle

5.2.4 Experimental Results of Case 4

Case 4 has a filling level of 50% (12.5 cm) and the excitation period of 2.35 seconds. The experiment is performed in the rectangular tank without baffles. The empty tank result is the same as case 2 as figure 91 (refer to appendix B) shows. Thus the moment force for the empty tank over the period of 2.35s is about 10Nm. The filled tank moment force plot can be seen in figure 97 (refer to appendix B). According to figure 97, the tank is subjected to a moment force of around 90Nm. The subtracted filled tank from the empty tank moment force result showing the value of about 80Nm is displayed in figure 98 (refer to appendix B). Based on a comparison of the numerical and experimental results in case 4 shown in figure 47, a difference of around 20Nm can be observed.

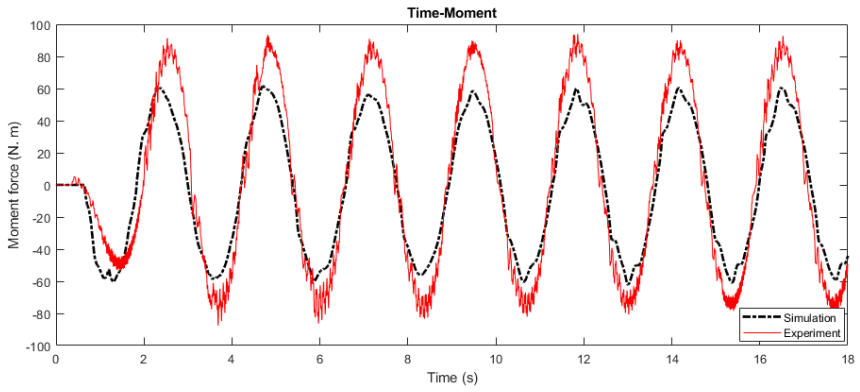

Figure 47: Numerical and experimental moment forces comparison of case 4 with the excitation period of 2.35s, 50% filling level, without baffle

5.3 Numerical Simulations of Water in Cylindrical Tank at 30% Filling Level

5.3.1 Numerical Results of Cylindrical Tank Without Baffle

30% Filling level

Refer to chapter 4.7 the cylindrical tank's natural frequency in a horizontal position is estimated through the Equation23 as $f_n = 3.42$ therefore the natural period for the tank is estimated as $T_n = 1.83$s. Water properties are the same as for rectangular tanks simulations which are shown in Table 8 in chapter 5.1.

Numerical Results of the Imposed Maximum Forces on the Left Hemisphere of the Cylindrical Tank for Water, Without Baffle

To find the maximum force applied on the left hemisphere, five other excitation periods (1.5s, 2s, 2.5s, 3s, 3.5s) in addition to the estimated natural period of 1.83s are simulated. In the following, the peak forces, and pressure for the filing level of 30% (7.2cm) will be studied. Figure 48 compares the peak forces applied on the left hemisphere of the cylindrical tank over the different excitation periods. The figure shows that at the period of 2.5s, the severity of the exerted forces on the left hemisphere of the tank is more than the other periods. The peak force of 74N is detected for this case, thus the excitation period of 2.5s is considered as the closest period to the natural period.

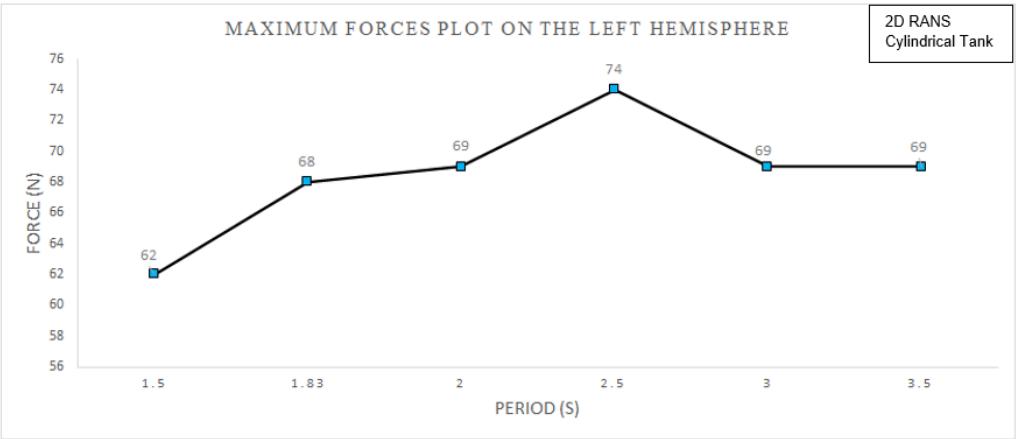

Figure 48: Numerical maximum forces of different simulated excitation periods on the left hemisphere of the cylindrical tank, when the filling level is 30% filled with water, without baffle

Figure 49 shows the imposed force diagram on the left hemisphere of the tank over the period of 2.5s. According to the below figure, the tank experienced the peak force at the time of 8.4 s with a value of 74.2N.

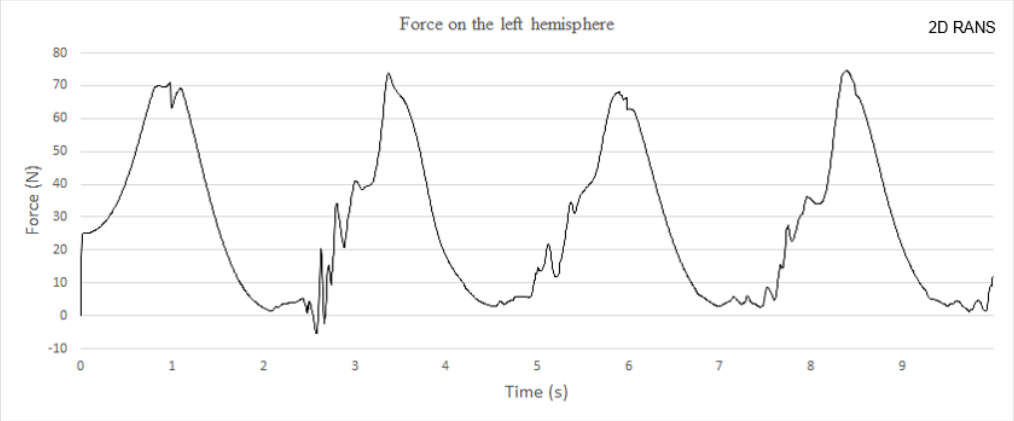

Figure 49: Numerical force monitor plot of the left hemisphere of the cylindrical tank at the excitation period of 2.5s when the filling level is 30% with water and no baffle is deployed

Figure 50 shows the volume fraction of the water shot taken at the moment of 8.4s when the highest force imposed on the left hemisphere.

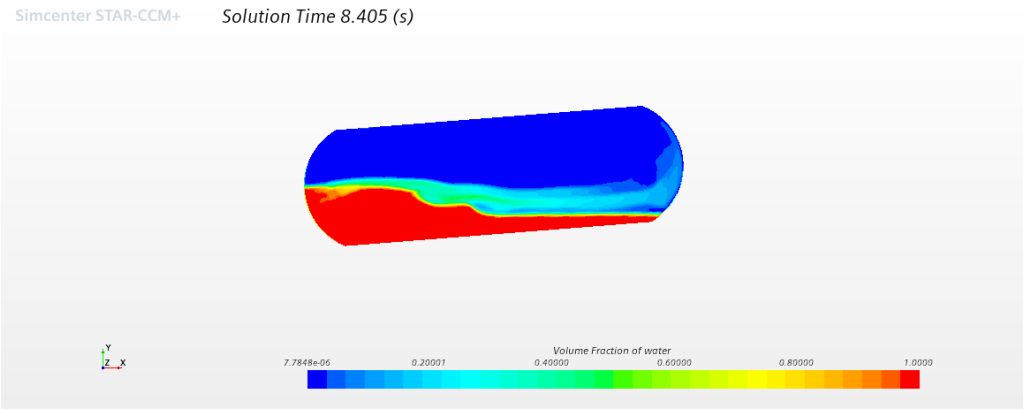

Figure 50: The volume fraction of water shot of peak force applied on the left hemisphere at the time of 8.4s, over the excitation period of 2.5s, filling level of 30%, without baffle

Numerical Results of the Impact Pressure and Pressure Distribution on the Left Hemisphere of the Cylindrical Tank for Water, Without Baffle

The impact pressure on the left hemisphere of the tank is measured over the excitation period of 2.5s. At the time of 8.4s, the highest pressure on the wall is measured as 368.5Pa. The pressure diagram and the pressure distribution are shown in figures 51 and 52, respectively.

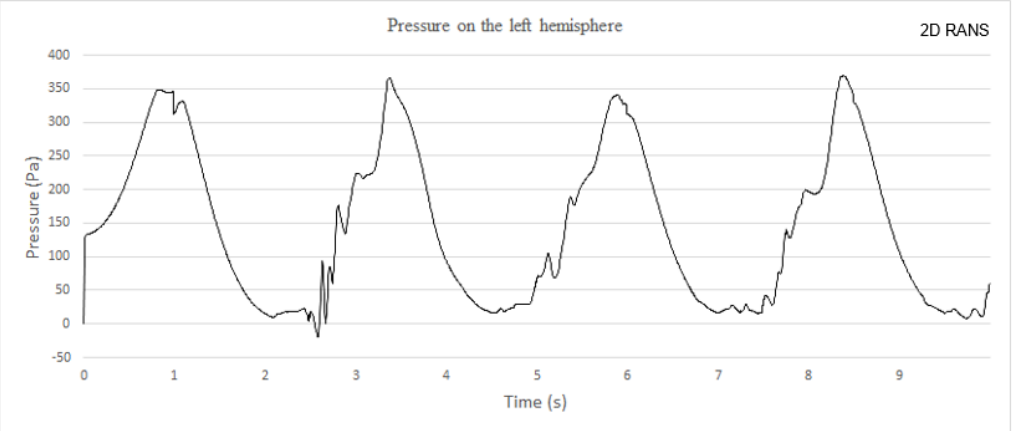

Figure 51: Numerical pressure monitor plot of the left cylindrical tank hemisphere over the excitation period of 2.5s, filling level of 30% with water when no baffle installed

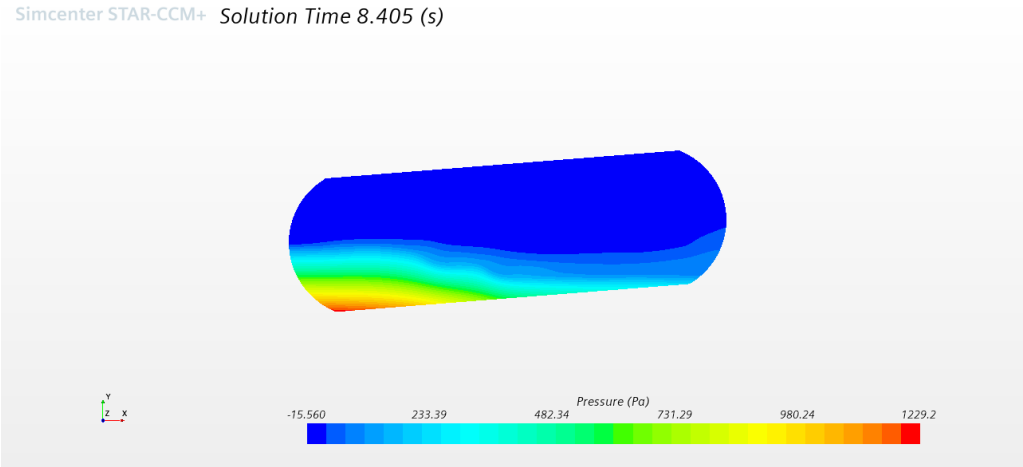

Figure 52: Pressure distribution on the left hemisphere at time 8.4s over the period of 2.5s, filling level of 30% with water, without baffle

5.3.2 Numerical Results of Baffle Effect on Cylindrical Tank

Maximum Imposed Forces on the Left Hemisphere Comparison

A low central baffle is used in the center of the cylindrical tank to study the effect of the baffle on the forces using the same periods (1.5s,1.83s, 2s, 2.5s, 3s, 3.5s) that have been simulated for the non-baffled cases. The low central baffle geometry and position in the cylindrical tank can be seen in figure 53.

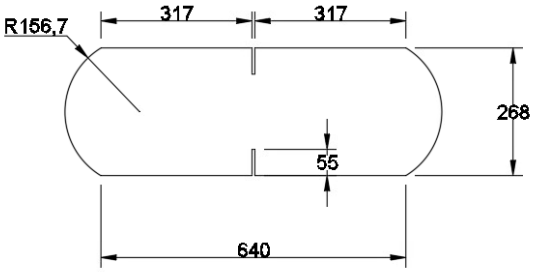

Figure 53: Low central baffle geometry and position within the cylindrical tank

The comparison of the measured peak forces diagram on the left hemisphere of the cylindrical tank for the baffled and non baffle cases can be seen in the figure 54. The force reduction for all cases is obvious when the low central baffle is used within the tank. As seen in the below diagram, a reduction of 25.6% $\left(\frac{74-55}{74}\right)$ occurs when the excitation period is 2.5s.

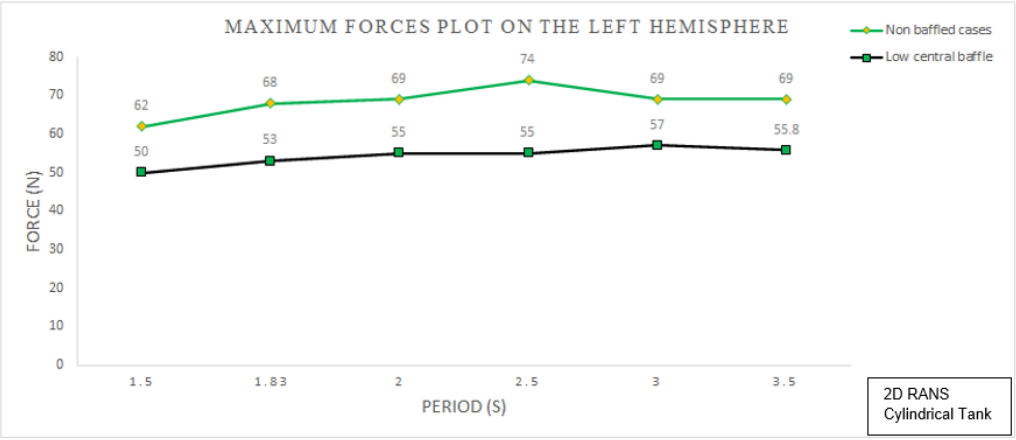

Figure 54: Numerical comparison of the maximum imposed forces on the tank's left hemisphere over different simulated periods between the low central baffle, and non baffle cases at 30% filling level with water

Figures 55 and 56 compare the force and volume fraction diagrams for baffled and non baffle cases during this excitation period.

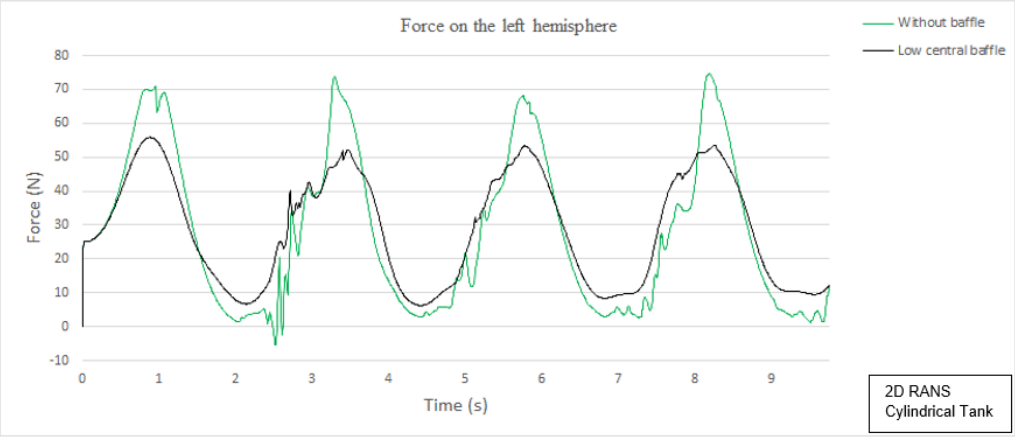

Figure 55: Numerical comparison between imposed forces on the left hemisphere over the excitation period of 2.5s between low central baffle, and non baffle cases at 30% filling level with water

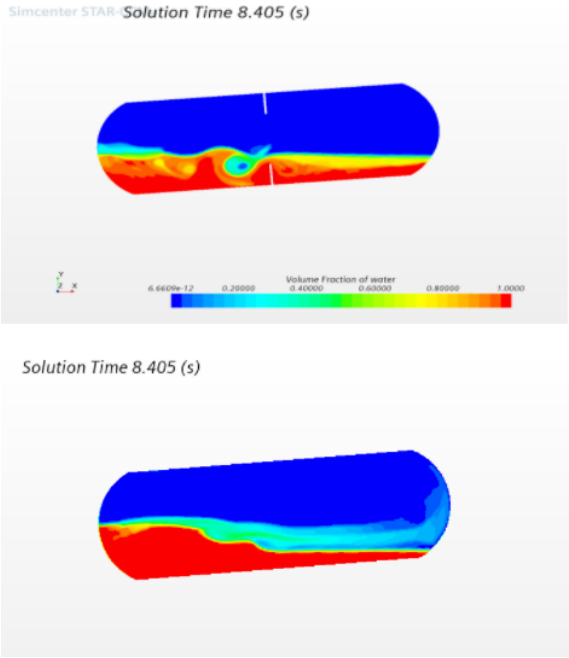

Figure 56: Volume fraction of water comparison at time 8.4s between baffled (up) and non baffle (down) cases over the period of 2.5s with 30% filling level

Impact Pressure on the Left Hemisphere Comparison

The pressure on the left hemisphere of the tank has been measured as well. In the following, both pressure diagrams for baffled and non baffle cases over the period of 2.5s where the highest pressure is measured between the other simulated periods are compared (Figure 57). The diagram shows that for the non baffle case the highest measured pressure is 368.5Pa while after the low central baffle installation the pressure value has decreased to 280Pa which shows a reduction of 24%.

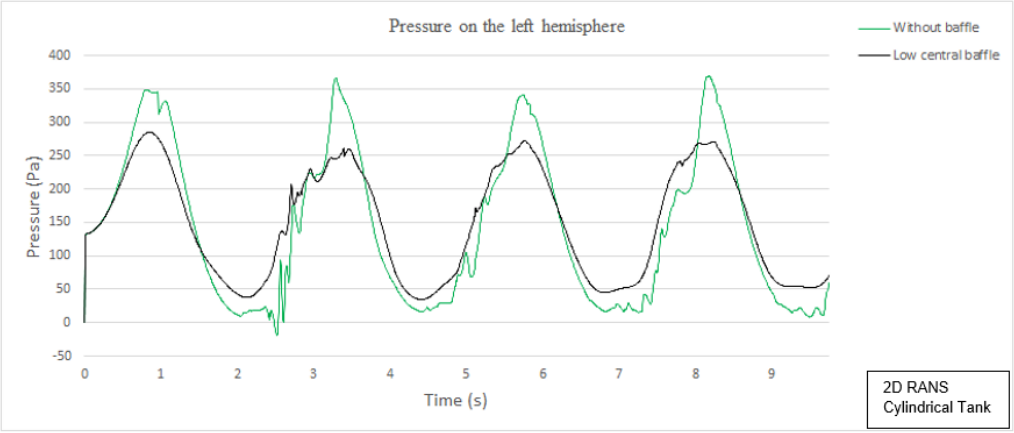

Figure 57: Numerical Pressure comparison for baffled and non baffle cases on the left hemisphere of the cylindrical tank over the period of 2.5s at the filling level of 30% with water

5.4 Numerical Simulations of Liquid Hydrogen in Cylindrical Tank at 30% Filling Level

30% Filling Level

5.4.1 Numerical Results of Cylindrical Tank Without Baffle

In this chapter LH2 and H2 are defined for the multi-phase components as the liquid and gas states respectively to be simulated in the same cylindrical tank as used for water with 30% filling level. Table 14 shows the properties of both LH2 and H2 when they are at equilibrium as they are defined in the simulation using the temperature of $-251.15°C$ (22K).

Table 14: LH2 and H2 properties at 22K

Fluid Type	Density	Dynamic Viscosity
LH2	68.9 kg/m^3	$1.14 * 10^{-5} Pa - s$
H2	2.06 kg/m^3	$6.98 * 10^{-7} Pa - s$

Numerical Results of the Imposed Maximum Forces on the Left Hemisphere of the Cylindrical Tank for LH2, Without Baffle

The maximum forces on the left hemisphere are measured for the periods of 1.5s, 1.83s, 2s, 2.5s, 3s, 3.5s the same as water cases. The peak forces diagram can be seen in the figure below (Figure 58). The below diagram shows that the exerted forces on the left tank hemisphere over the simulated periods are now more at the same levels with the peak of 4.5N using LH2 and H2 as the phases.

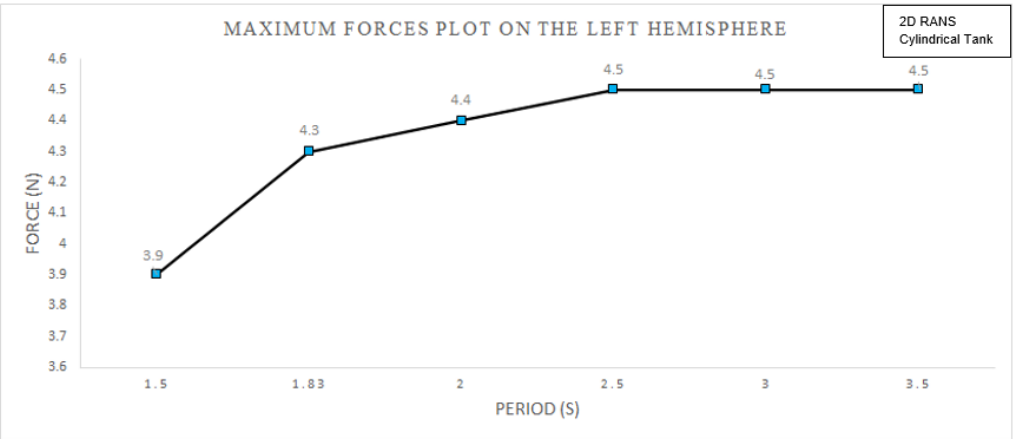

Figure 58: Numerical maximum forces of different simulated excitation periods on the left hemisphere of the cylindrical tank when the filling level is 30% for LH2, without baffle

Since in the water simulations, 2.5s was selected as the closest period to the natural period, this period is selected for the hydrogen as well to be able to have the comparison with the water results too. The force diagram on the left tank hemisphere over the excitation period of 2.5s is shown in Figure 59. The peak of 4.5N is detected at the moment of 8.37s as the below diagram shows.

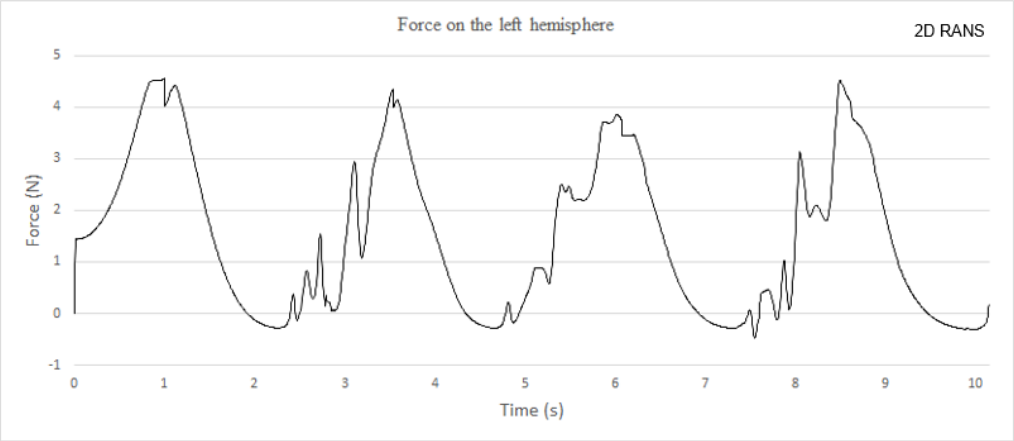

Figure 59: Numerical force monitor plot of the left hemisphere of the cylindrical tank over the excitation period of 2.5s when the filling level is 30% with LH2 and no baffle is deployed

Consequently, the shot from that moment can be taken from the volume fraction of hydrogen as figure 60 displays.

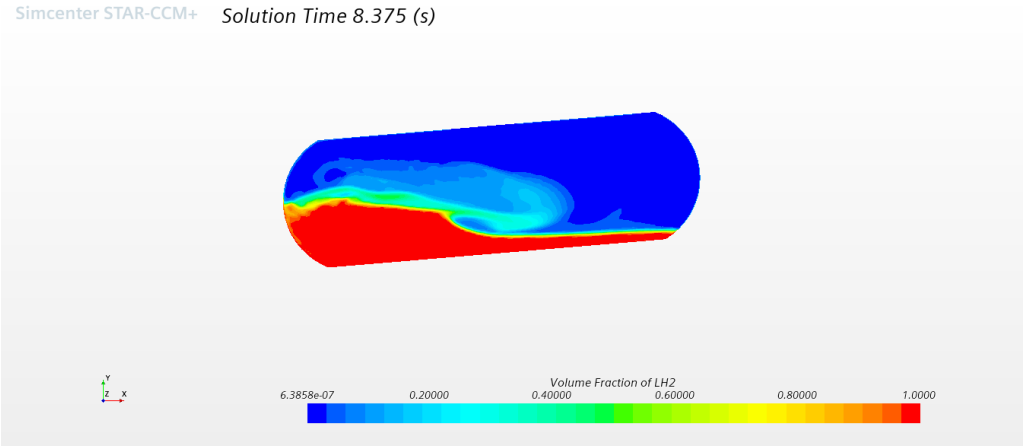

Figure 60: The volume fraction of LH2 shot of the peak force applied on the left hemisphere at the time of 8.37s over the excitation period of 2.5s, filling level of 30%, without baffle

Numerical Results of the Impact Pressure and Pressure Distribution on the Left Hemisphere of the Cylindrical Tank for LH2, Without Baffle

The impact pressure on the left hemisphere is measured when the excitation period is 2.5s. The diagram below shows the recorded pressure (Figure 61). The figure diagram shows that the highest pressure of 23.5Pa is measured at the time of 8.37s.

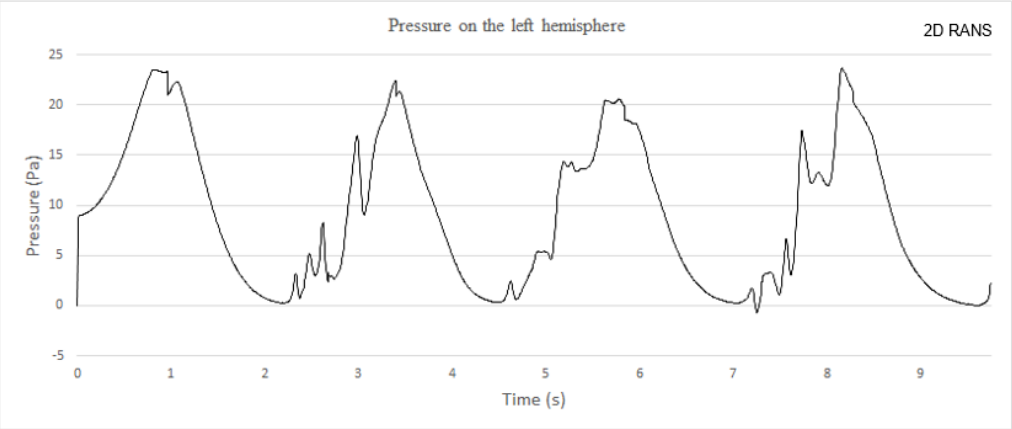

Figure 61: Numerical pressure monitor plot of the left tank hemisphere over the excitation period of 2.5s, filling level of 30% with LH2 and no baffle installed

The pressure distribution at the moment of 8.37s over the same excitation period of 2.5s is shown in figure 62.

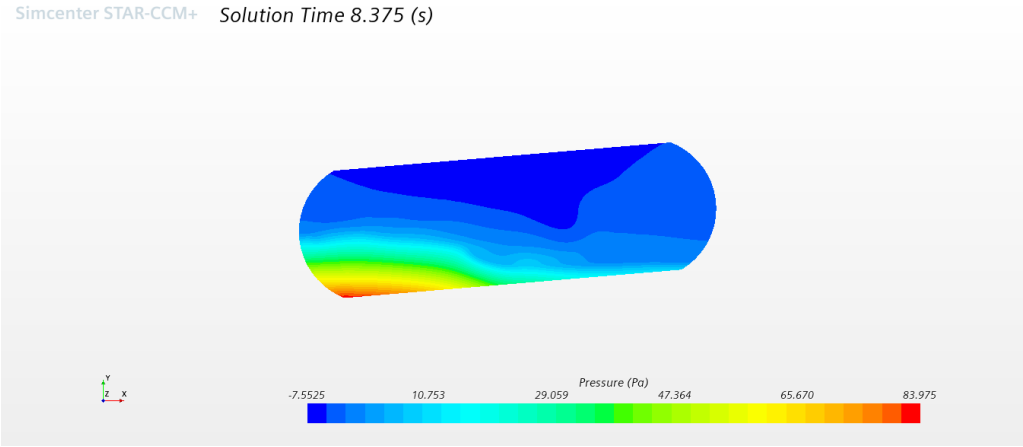

Figure 62: Pressure distribution on the left hemisphere at time 8.37s, filling level of 30% with LH2, without baffle

5.4.2 Numerical Results of Baffle Effect on Cylindrical Tank

Maximum Imposed Forces on the Left Hemisphere Comparison

The same low central baffle is used as the one which was used for the cylindrical water tank. At 30% filling level, the comparison between the peak forces of the baffled and non baffle cases can be seen in figure 63. The comparison shows a reduction of 17.7% $\left(\frac{4.5-3.7}{4.5}\right)$ for the case with the excitation period of 2.5s.

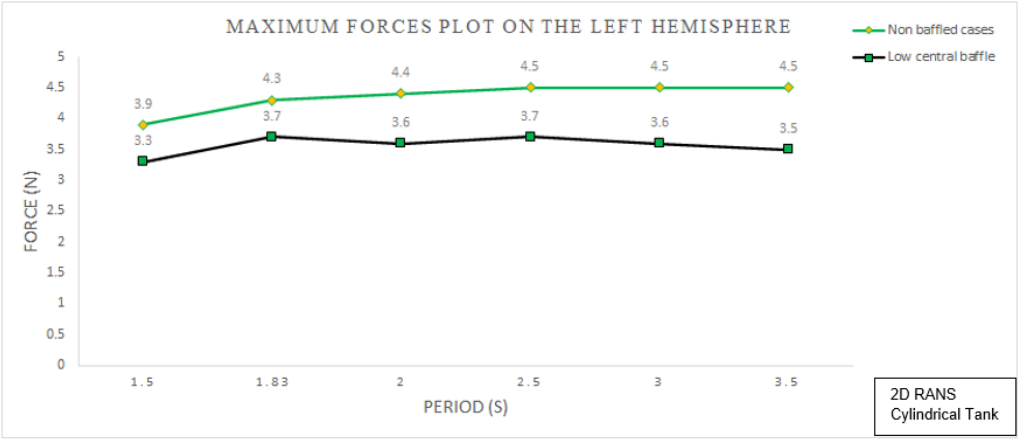

Figure 63: Numerical comparison of the maximum imposed forces on the tank's left hemisphere over different simulated periods between the low central baffle, and non baffle cases at 30% filling level with LH2

The force and volume fraction diagrams for baffled and non baffle cases are compared in figures 64 and 65 respectively. The below diagram shows clearly the force drop of 17.7% after installing the low central baffle over the excitation period of 2.5s.

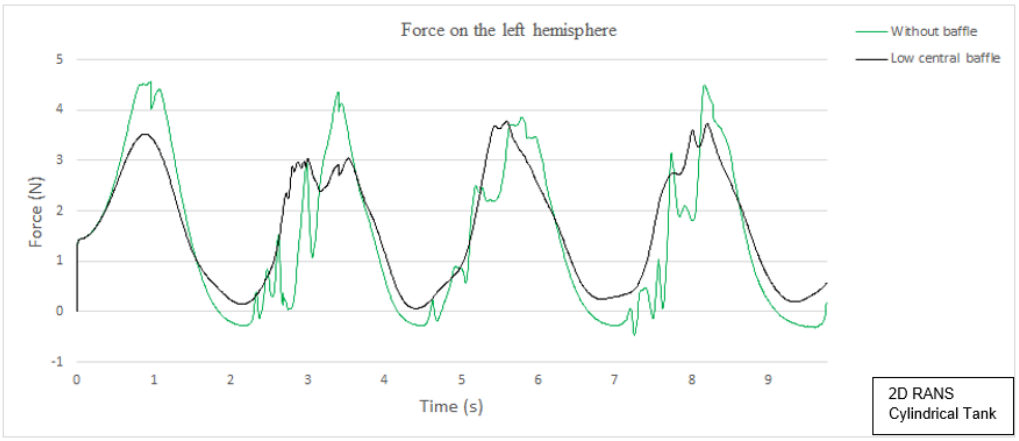

Figure 64: Numerical comparison between imposed forces on the left hemisphere over the excitation period of 2.5s between low central baffle, and non baffle cases at 30% filling level filled with LH2

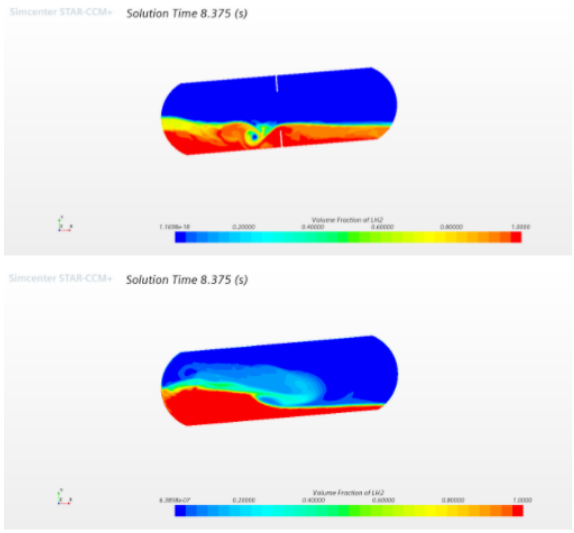

Figure 65: Volume fraction of LH2 comparison at time 8.37s between baffled (up) and non baffle (down) cases over the excitation period of 2.5s

Impact Pressure on the Left Hemisphere Comparison

The pressure on the left hemisphere diagram for baffled and non baffle cases can be compared as the pressure is measured for both cases. Figure 66 compares the pressure measured on the left hemisphere for baffled and non baffle cases. The below diagram shows after installing the low central baffle the measured peak pressure is about 20Pa while the peak pressure for the non baffle case is detected as 23.5Pa which shows a drop of 14.8% in the peak pressure value over the excitation period of 2.5s.

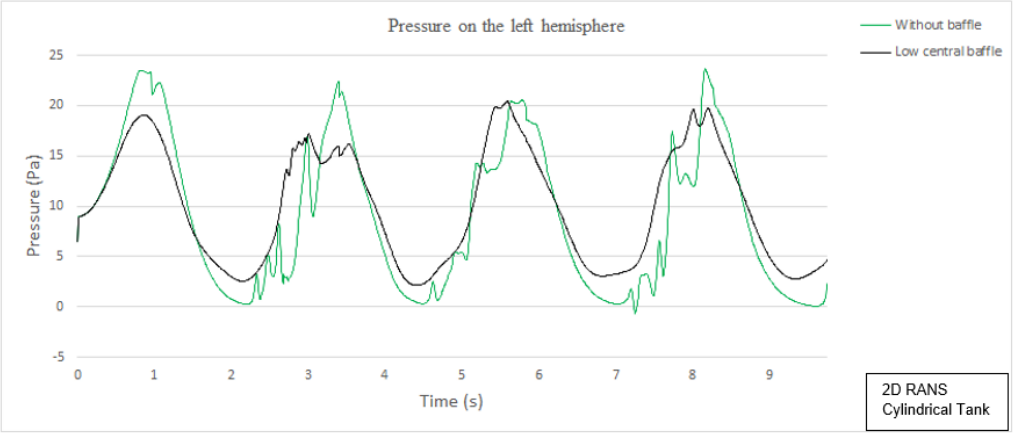

Figure 66: Numerical Pressure comparison for baffled and non baffle cases on the left hemisphere of the cylindrical tank over the period of 2.5s at the filling level of 30% filled with LH2

5.5 Numerical Simulations of LNG in Cylindrical Tank at 30% Filling Level

5.5.1 Numerical Results of Cylindrical Tank Without Baffle

30% Filling Level

This section studies the behavior of the LNG using pure methane (CH4) as the main fluid in the same cylindrical tank as used for water and LH2 with 30% filling level. CH4 properties in liquid and gas states when the liquid and gas are at equilibrium at the temperature of $-163°C$ (110K) are defined in the simulation as multi-phase. Table 15 shows the fluid properties.

Table 15: LNG and CH4 properties at 110K

Fluid Type	Density	Dynamic Viscosity
LNG	422.6 kg/m^3	$1.2 * 10^{-4} Pa - s$
CH4	1.79 kg/m^3	$4.4 * 10^{-6} Pa - s$

Numerical Results of the Imposed Maximum Forces on the Left Hemisphere of the Cylindrical Tank for LNG, Without Baffle

Excitation periods for LNG are the same as those used for water and hydrogen and simulated in the same cylindrical tanks. When there is no baffle installed, the peak forces on the left hemisphere of the cylindrical tank are measured as before which can be seen in figure 67. As the below diagram illustrates the maximum force is detected over the excitation period of 2.5s with the value of 30.2N and due to the comparison of the simulated LNG results with water and hydrogen results, the same excitation period of 2.5s is selected to be studied for LNG.

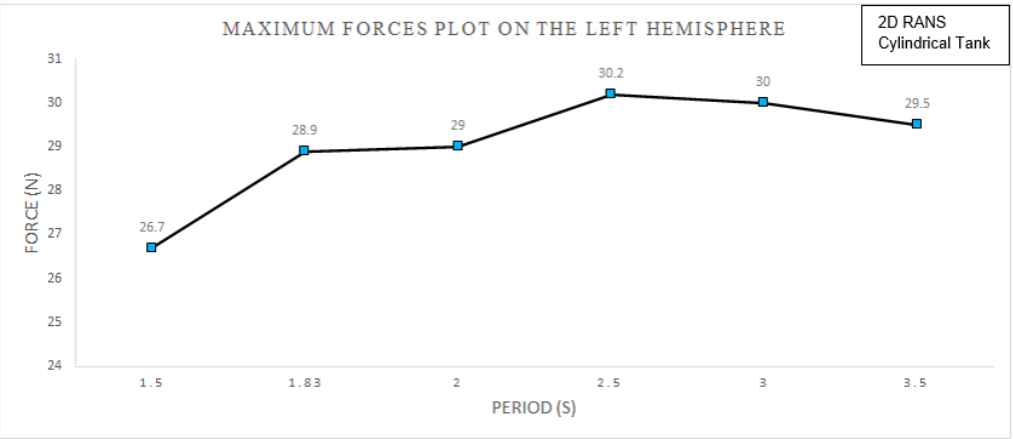

Figure 67: Numerical maximum forces of different simulated excitation periods on the left hemisphere of the cylindrical tank, when the filling level is 30% with LNG

The figure below shows the exerted force diagram on the left hemisphere of the tank over the excitation period of 2.5s. (Figure 68).

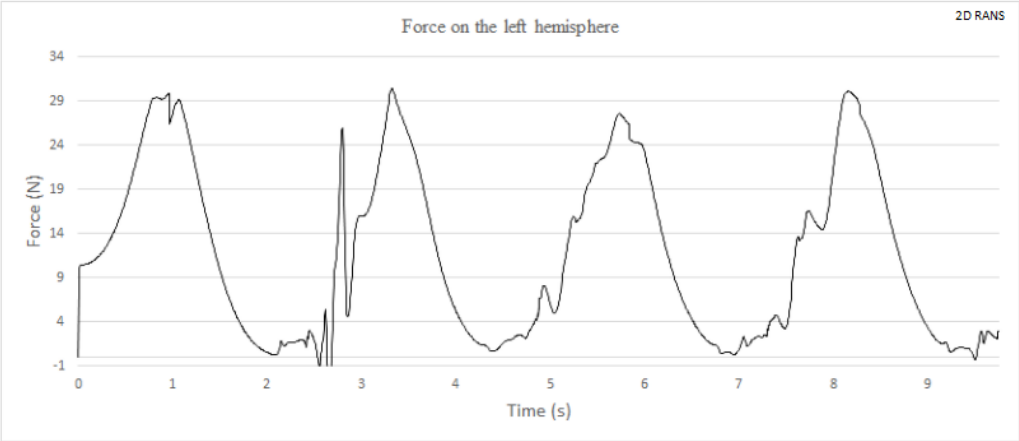

Figure 68: Numerical force monitor plot of the left hemisphere of the cylindrical tank over the excitation period of 2.5s when the filling level is 30% with LNG and no baffle is deployed

According to the above diagram, the peak of 30.2N is detected at 3.42s, thus the shot taken from the volume fraction of LNG at the same moment of 3.42s is shown in figure 69.

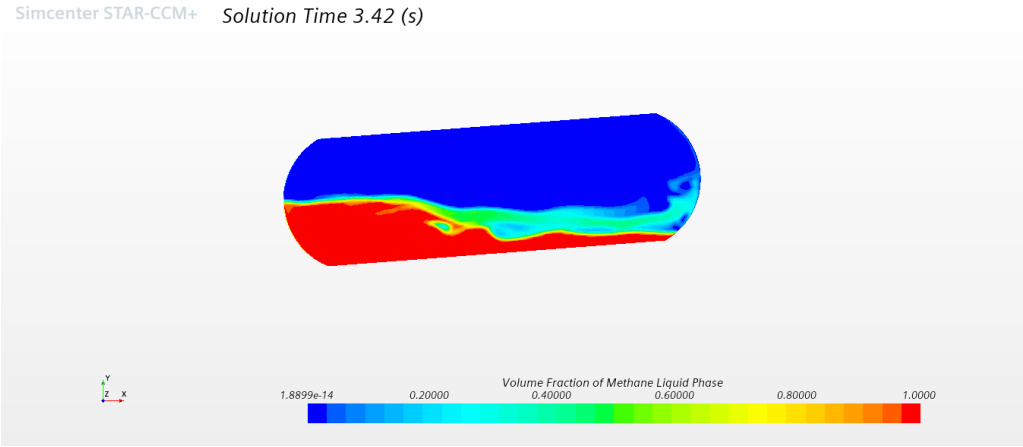

Figure 69: The volume fraction of LNG shot of peak force applied on the left hemisphere at the time of 8.4s, over the excitation period of 2.5s, filling level of 30%, without baffle

Numerical Results of the Impact Pressure and Pressure Distribution on the Left Hemisphere of the Cylindrical Tank for LNG, Without Baffle

Over the same excitation period of 2.5s, the pressure is measured on the left tank hemisphere as figure 70 shows.

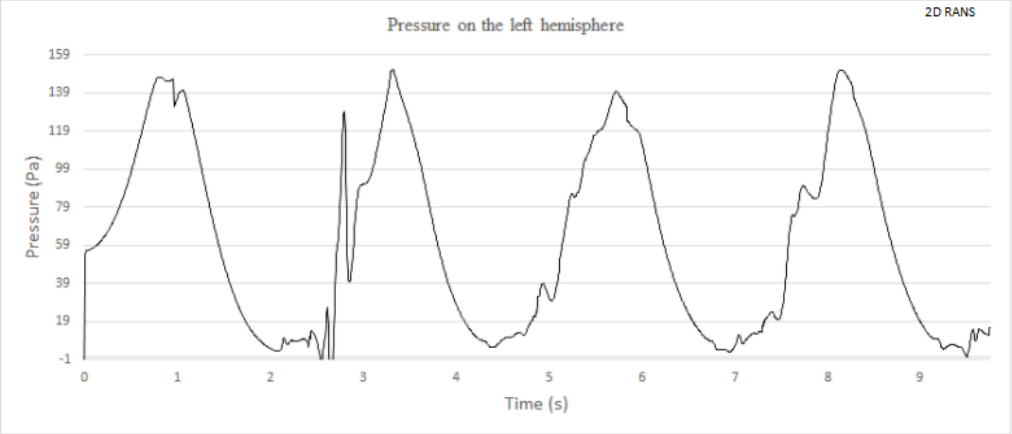

Figure 70: Numerical pressure monitor plot of the left tank hemisphere over the excitation period of 2.5s, filling level of 30% with LNG and no baffle installed

According to the above diagram, the peak pressure of 151.2Pa occurs at 3.42s over the excitation period of 2.5s. The pressure distribution at this time is shown in figure 71.

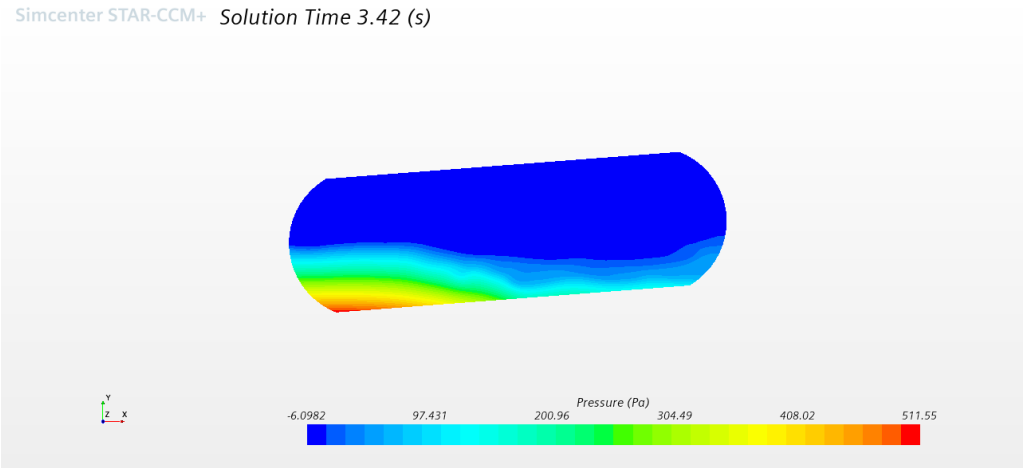

Figure 71: Pressure distribution on the left hemisphere at time 3.42s over the excitation period of 2.5s, filling level of 30% with LNG, without baffle

5.5.2 Numerical Results of Baffle Effect on Cylindrical Tank

The same low central baffle and excitation periods are used for LNG as previously used for water and LH2 to measure and compare the result with non baffle cases. The peak forces comparison for baffled and non baffle cases is shown in figure 72. The below diagram shows after installing the low central baffle, a drop of 23% $\left(\frac{30.2-23.2}{30.2}\right)$ is occurred in the imposed maximum forces on the left hemisphere over the excitation period of 2.5s.

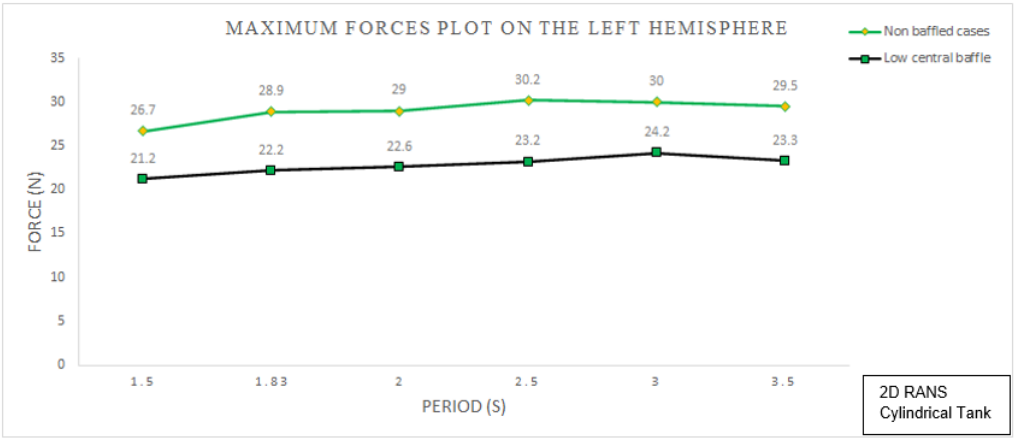

Figure 72: Numerical comparison of the maximum imposed forces on the tank's left hemisphere over different simulated periods between the low central baffle, and non baffle cases at 30% filling level with LNG

The imposed force on the left hemisphere of the tank comparison diagram between baffled and non baffle cases over the excitation period of 2.5s shows a drop of 23% in the peak measured forces is shown in figure 73.

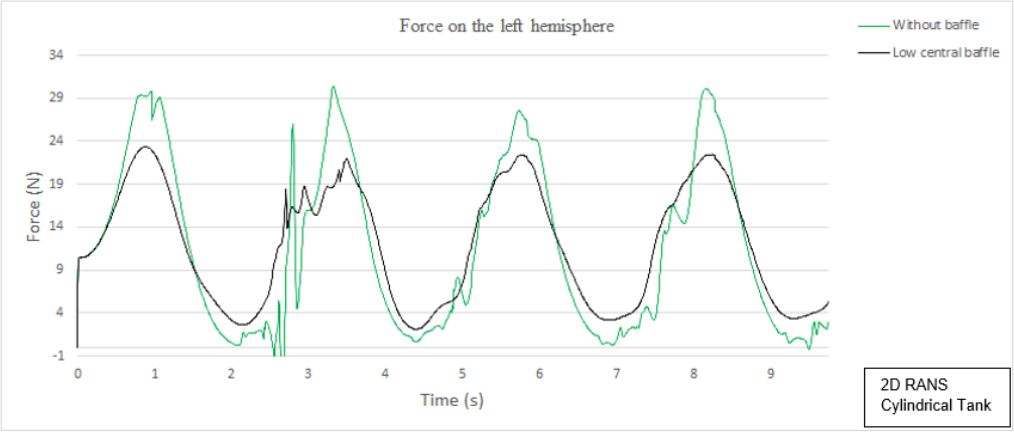

Figure 73: Numerical comparison between imposed forces on the left hemisphere over the excitation period of 2.5s between low central baffle, and non baffle cases at 30% filling level with LNG

The volume fraction of LNG shot at the time of 3.42s where the highest applied force on the left side of the tank is measured for the non baffle case with the baffled case at the same time is shown in figure 74.

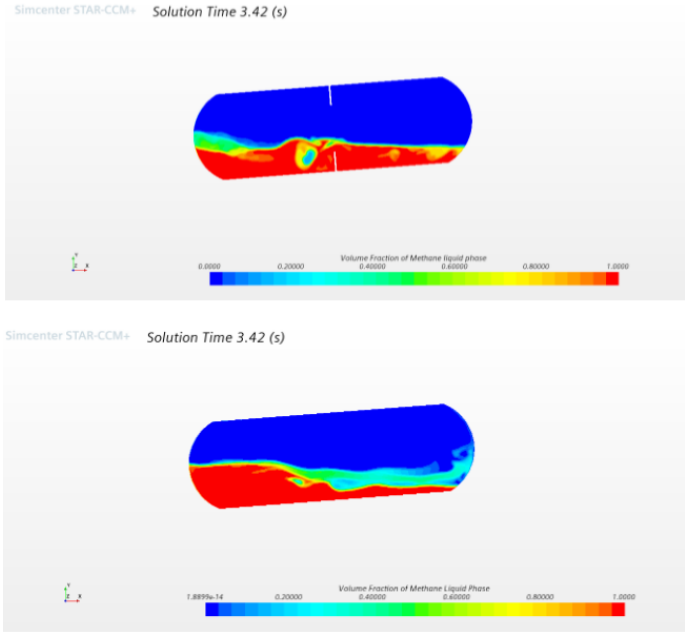

Figure 74: Volume fraction of LNG comparison at time 3.42s between baffled (up) and non baffle (down) cases over the excitation period of 2.5s

Impact Pressure on the Left Hemisphere Comparison

The impact pressure on the left hemisphere of the cylindrical tank is measured as well. Figure 75 compares the measured impact pressure on the left hemisphere for baffled and non baffle cases over the excitation period of 2.5s. According to the below diagram, a drop of 20.7% $\left(\frac{151.2-119.8}{151.2}\right)$ occurs in the peak measured pressure after installing the low central baffle within the cylindrical tank.

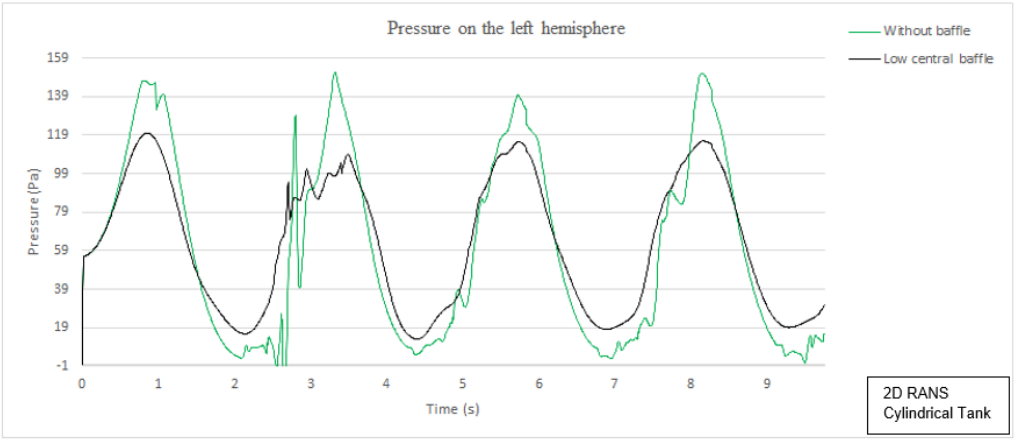

Figure 75: Numerical Pressure comparison for baffled and non baffle cases on the left hemisphere of the cylindrical tank over the period of 2.5s at the filling level of 30% with LNG

5.6 Comparison of Numerical Results of Water, Liquid Hydrogen, and LNG of Cylindrical Tank at 30% Filling Level

In this chapter, the maximum forces applied on the left tank hemisphere for water, LH2, and LNG are compared for both baffled and non baffle cases. In addition to the peak forces, the same comparison is done for the peak pressure measured on the left hemisphere for all simulated fluids. Finally, the free surface elevation of one excitation period (2.5s) is chosen to be compared with different fluids.

5.6.1 Maximum Imposed Forces on the Left Hemisphere for Without Baffle Cases

The diagram below shows the comparison of the measured peak forces on the left hemisphere of the cylindrical tank between all fluid types when no baffle is installed (Figure 76). It is evident in the below diagram that the tank walls are subject to the largest forces when water is the main fluid, while the least forces occur when LH2 is the main fluid which is due to the difference in densities of the fluids. As seen, the highest force value of 74N is measured for the water case over the excitation period of 2.5s, using the same period, the highest recorded force value is 4.5N for the LH2 case, which shows a drop of 93.9% $\left(\frac{74-4.5}{74}\right)$ in comparing water and LH2. This reduction is around 59% $\left(\frac{74-30.2}{74}\right)$ when the water case is compared with the LNG.

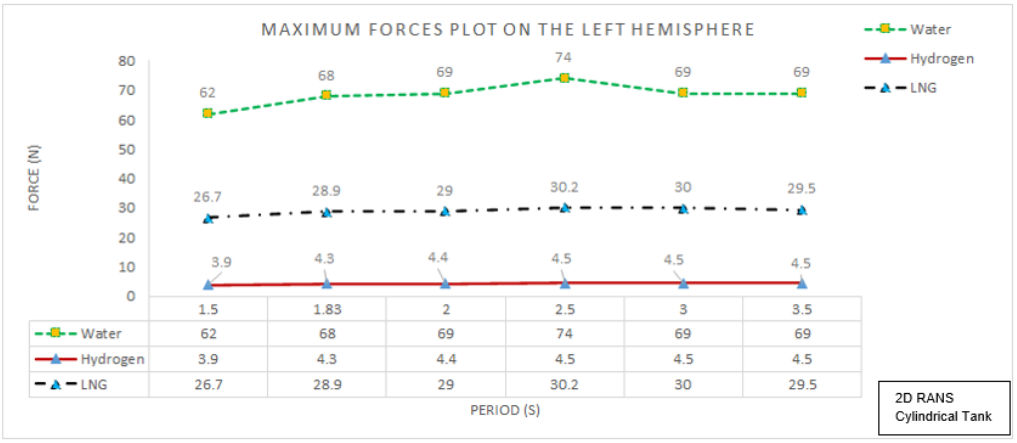

Figure 76: Numerical comparison of maximum imposed forces of different fluids and periods on the left tank hemisphere when the filling level is 30%, without baffle

5.6.2 Maximum Imposed Forces on the Left Hemisphere for Low Central Baffle Cases

The maximum forces can also be compared for the cylindrical tank which is equipped with the low central baffle for all fluid types as figure 77 shows. By comparing the highest imposed forces on the left hemisphere of the cylindrical tank between water and liquid hydrogen over the excitation period of 2.5s, the below diagram shows a reduction of 93.2% $\left(\frac{55-3.7}{55}\right)$ is detected. While this reduction over the same excitation period of 2.5s, when the comparison is performed between water and LNG is around 57.8% $\left(\frac{55-23.2}{55}\right)$.

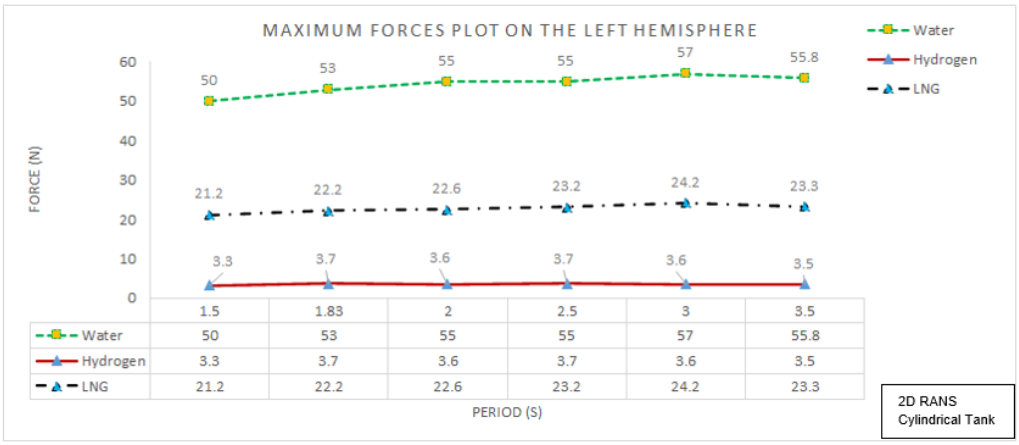

	1.5	1.83	2	2.5	3	3.5
Water	50	53	55	55	57	55.8
Hydrogen	3.3	3.7	3.6	3.7	3.6	3.5
LNG	21.2	22.2	22.6	23.2	24.2	23.3

Figure 77: Numerical comparison of maximum imposed forces of different fluids and periods on the left tank hemisphere when the filling level is 30%, with low central baffle

5.6.3 Maximum Impact Pressure on the Left Hemisphere for Without Baffle Cases

The diagram below compares the detected peak pressure on the left tank hemisphere of different simulated fluids of water, hydrogen, and LNG when there is no baffle inside the tank (Figure 78). The below diagram shows, a reduction of 93.6% $\left(\frac{368.5-23.5}{368.5}\right)$ comparing the water and LH2 cases over the excitation period of 2.5s. This reduction value is around 59% $\left(\frac{368.5-151.2}{368.5}\right)$ when the water case is compared with the LNG case with the same excitation period of 2.5s.

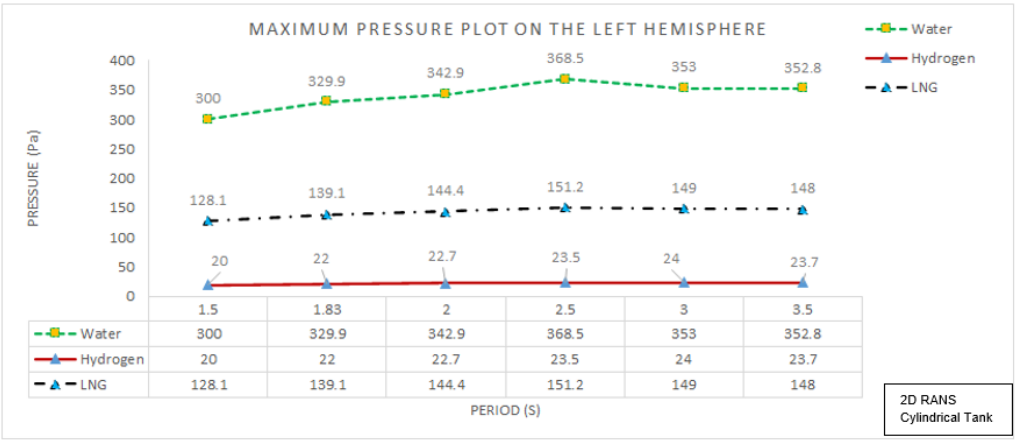

	1.5	1.83	2	2.5	3	3.5
Water	300	329.9	342.9	368.5	353	352.8
Hydrogen	20	22	22.7	23.5	24	23.7
LNG	128.1	139.1	144.4	151.2	149	148

Figure 78: Numerical comparison of maximum pressure of different fluids and periods on the left hemisphere when the filling level is 30%, without baffle

5.6.4 Maximum Impact Pressure on the Left Hemisphere for Low Central Baffle Cases

The following figure compares the pressure on the left tank hemisphere of different fluids when the tank has the low central baffle installed (Figure 79). Considering the excitation period of 2.5s, the below diagram shows a reduction of 93% $\left(\frac{284.9-20}{284.9}\right)$ when the water case is compared with the

LH2 using the cylindrical tank equipped with the low central baffle. This reduction is about 58% $\left(\frac{284.9-119.8}{284.9}\right)$ when the comparison is between water and LNG cases over the excitation period of 2.5s.

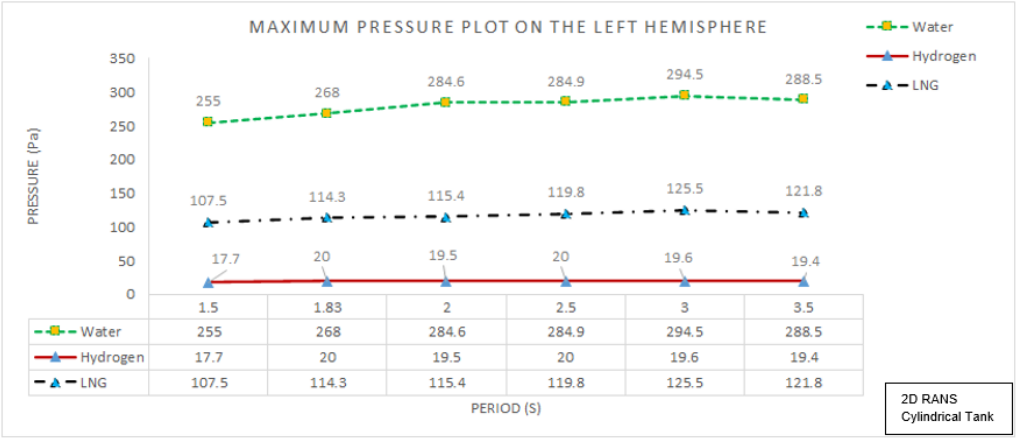

Figure 79: Numerical comparison of maximum pressure of different fluids and periods on the left hemisphere when the filling level is 30%, with low central baffle

5.6.5 Free Surface Elevation on Defined Plane for Without Baffle Cases

The excitation period of 2.5s is selected to compare the free surface elevation on the defined plane of water, LH2, and LNG. Figure 80 compares the free surface elevation measured from water, LH2, and LNG when no baffle is installed in the cylindrical tank over the excitation period of 2.5s. The below diagram shows that the free surface height measured on the defined plane is approximately around 13.5cm for all fluids.

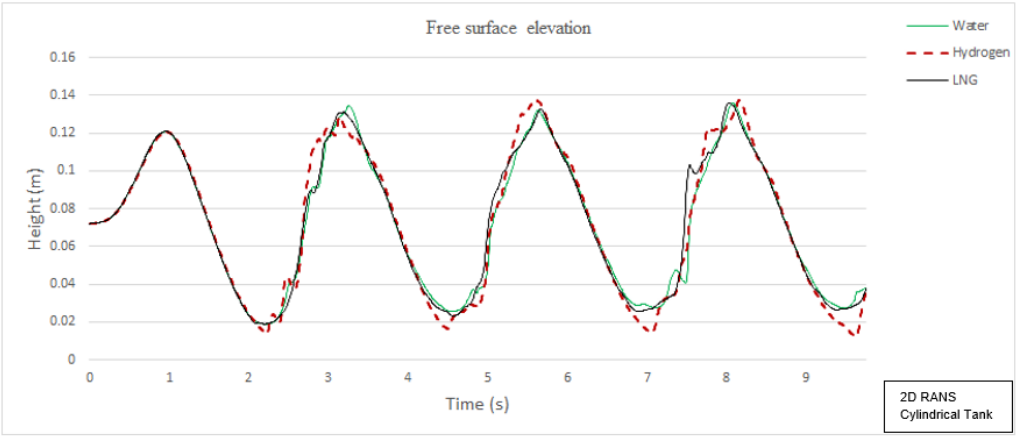

Figure 80: Numerical comparison of the measured free surface elevation on a defined plane between different fluids, over the excitation period of 2.5s at 30% filling level and without baffle

5.6.6 Free Surface Elevation on Defined Plane for Low Central Baffle Cases

The comparison is performed for the low central baffle cases as well, which can be seen in the figure below (Figure 81). Based on the below diagram, all fluids have almost the same elevation on the plane which is approximately 10cm over the period of 2.5s when the low central baffle is installed within the cylindrical tank.

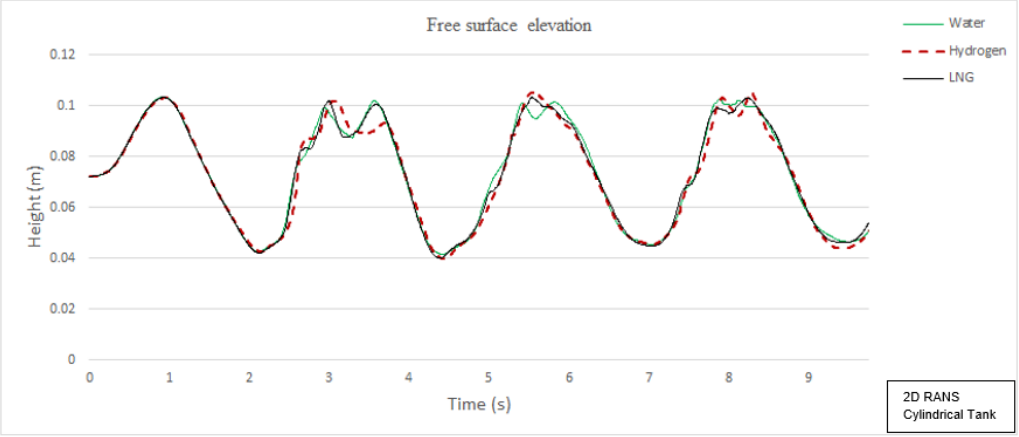

Figure 81: Numerical comparison of the measured free surface elevation on a defined plane between different fluids, over the excitation period of 2.5s at 30% filling level with low central baffle

5.7 Numerical 3-Dimensional Effect

To support the 2D numerical results, a Three-Dimensional case of the non baffled cylindrical tank is simulated as well in this research to compare the obtained hydrodynamic forces on the left hemisphere of the cylindrical tank between 2D and 3D cases. As Table 5 in chapter 1.5 shows, the filling level is 30%, the excitation period of 2.5s is selected when water is the main fluid.

Figure 82 compares the imposed forces on the left hemisphere of the cylindrical tank between 2D and 3D cases over the natural period of 2.5s. as can be seen in this figure, the difference of about 14% can be observed between the two graphs.

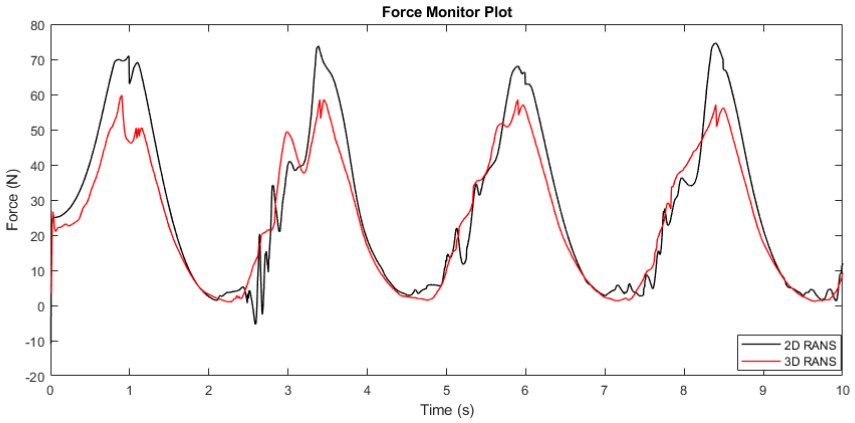

Figure 82: Numerical comparison of the 2D and 3D measured force imposed on the left hemisphere of the cylindrical tank over the excitation period of 2.5s, when the filling level is 30%, filled with water, without baffle

The impact pressure on the left hemisphere is also measured. As figure 83 shows, the peak pressure for the 2D case is measured as 367Pa while this value for the 3D case is 320Pa which shows the difference of around 13%. Therefore, the 2D numerical cases in this research are comparable with the 3D ones with the difference of about 13%.

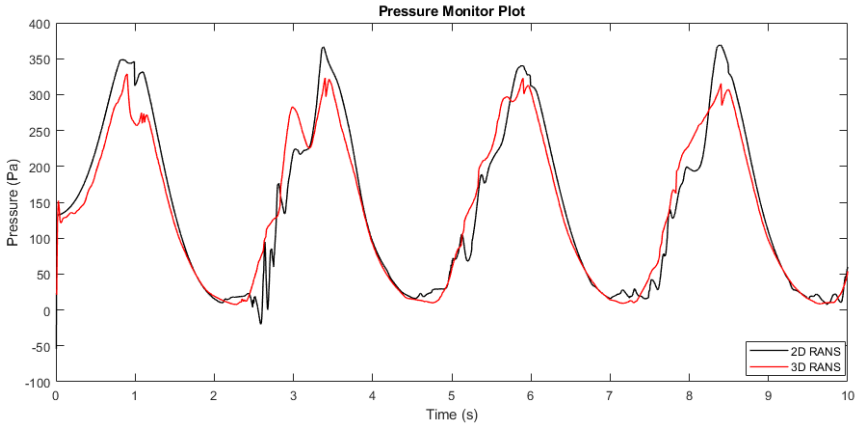

Figure 83: Numerical comparison of the 2D and 3D measured pressure imposed on the left hemisphere of the cylindrical tank over the excitation period of 2.5s, when the filling level is 30%, filled with water, without baffle

5.8 Summary of Chapter

In this chapter, three different fluids (water, LH2, and LNG) are selected to be simulated. The first case was water which is simulated for both rectangular and cylindrical tanks. With the pitch motion of 4.8 degrees applied to the rectangular tank and 6 degrees for the cylindrical tank. Three different filling levels are applied including 30, 50, and 70 percent. The left wall of the rectangular tanks is selected to study the exerted hydrodynamic forces on it over different excitation periods to find the natural period and the most severe motions in the tank. In addition to the forces, the free surface elevation is measured on the defined plane placed 3cm away from the left tank wall. Furthermore, the impact pressure on the same left wall of the rectangular tanks and pressure distribution are studied as well. Except for the filling level which is only 30%, the same procedure is performed for cylindrical tanks using its left hemisphere to measure the imposed forces and pressure having water, hydrogen, and LNG as main fluids. The effect of baffles is also studied as two different baffles (Low and slot central baffle) are used for the rectangular and the low central baffle is used for the cylindrical tank. The applied moment force results on the rectangular tank obtained from the simulations are validated by comparing them with the experimental results for 4 different cases and lastly, comparisons in terms of forces and free surface elevation in the cylindrical tanks are performed between all three simulated fluids with 30% of filling level.

Due to a large number of results and to have an efficient and accurate summary, Table 16 is designed for the rectangular tank filled with water showing different filling levels to display the reduction percentage of imposed forces and free surface elevation on the left tank wall and the defined plane while the low and slot baffle are compared with the non-baffle cases over the natural periods.

Table 16: Numerical results of the reduction percentage comparison of imposed forces and free surface elevation on the left rectangular tank wall and the defined plane while the low and slot baffle are compared with the non-baffle cases with different filling levels over the natural period for each filling, filled with water

Filling level	Natural period (s)	Reduction percentage of forces -low baffle	Reduction percentage of forces -slot baffle	Reduction percentage of free surface -low baffle	Reduction percentage of free surface -slot baffle
30%(7.5cm)	1.9	34.4%	56%	31.8%	40.9%
50%(12.5cm)	1.65	46.4%	59.5%	36.8	47.3%
70%(17.5cm)	1.6	42%	52.1%	14.2%	26.1%

This result can also be summarized for a period that is away from the natural period such as the excitation period of 3s. Table 17 shows the efficiency of both baffles in reducing the imposed forces on the rectangular tank walls over the excitation period of 3s, filled with water.

Table 17: Reduction in baffles efficiency over the excitation period of 3s within the rectangular tank filled with water

Filling level	Excitation period (s)	Reduction percentage of forces -low baffle	Reduction percentage of forces -slot baffle
30%(7.5cm)	3	40.4%	44.7%
50%(12.5cm)	3	16.1%	23%
70%(17.5cm)	3	4.6%	12.1%

Regarding the cylindrical tank, Table 18 is designed to compare the measured peak forces on the left hemisphere of the tank for both baffled and non-baffled cases over the natural period of 2.5s between water, LH2, and LNG at 30% filling level.

Table 18: Comparison of the measured peak forces on the left hemisphere of the cylindrical tank over the natural period of 2.5s between water, LH2, and LNG at 30% filling level for baffled and non-baffled cases

Fluid Type	Natural Period (s)	Highest Imposed Force on the Left Hemisphere -Without Baffle (N)	Highest Imposed Force on the Left Hemisphere -With Baffle (N)
Water	2.5	74	55
LNG	2.5	30.2	23.2
LH2	2.5	4.5	3.7

6 Conclusion

6.1 Conclusion

The sloshing phenomenon with different filling levels (30%,50%,70%), tank types (rectangular, cylindrical), and fluids (Water, LH2, LNG) is studied in this thesis. The 2D RANS turbulence model and VOF numerical multi-phase flow are performed using STAR-CCM+ and the results are validated through the experimental results which are recorded in the NTNU laboratory. The tanks are subjected to pitch motion with an amplitude of 4.8 degrees (6 degrees for cylindrical tanks) while they are in horizontal positions. The method of using the empirical formulas for calculating the natural frequencies of tanks is detected to have a good agreement with the numerical results as for the rectangular tank with 30% filling level the difference percentage is 19%, for 50% filling level the difference is 10% and when the tank is filled for 70% the method is nearly accurate, meaning that the difference percentage for estimated natural frequency of the rectangular tank with 70% filling level is less than 5% with the numerical results, however for the cylindrical tank with 30% filling level, the difference percentage is around 26.8% which is larger than the estimated values for the rectangular tank. That could be due to the shape and structure of the hemispheres of the cylindrical tank. Within the rectangular tank filled with water with different levels of filling, two types of baffles are used, including low central and slot central baffles. The study is performed considering the hydrodynamic forces, pressure and free surface elevation.

Table 16 in chapter 5.8 indicates that, for the imposed forces on the rectangular tank walls filled with water, the efficiency of the low central baffle to reduce the forces on the walls for all filling levels ranges from 34.4 to 46.4 percent, whereas the slot baffle's efficiency ranges from 52.1 to 59.5 percent. The elevation of the free surface is also influenced by baffles which have reductions ranging from 14.2 to 36.8 percent for low baffles and from 26.1 to 47.3 percent for slot baffles. In addition, it should be noted that the maximum effect from both baffles occurs when the filling level is 50% but in total, the slot baffle is found to be highly effective in controlling the intensity of sloshing motions, thereby reducing the rapid pressure drop and imposed forces in the tanks.

Furthermore, this should be taken into account that the excitation periods away from the natural period decrease the efficiency of both baffles, especially when the filling level increases. As Table 17 in chapter 5.8 displays the cases over the excitation period of 3s, by increasing the filling level, the reduction percentage of the imposed forces on the tank walls decreases. In the example of cases with 70% filling level between the natural period of 1.6s and the excitation period of 3s, the low baffle's efficiency drops from 46.4% to 16.1%, likewise for the slot baffle, it drops from 59.5% to 23%.

In the validation part, a comparison of the moment forces recorded with the rectangular tank in different experimental cases and the numerical cases shows a difference of 20 to 25 percent. which can be considered as a normal difference due to the whole simplifications that are done in the numerical method such as time step and mesh size adjustments to reduce the computational cost and time, additionally, the shot correspondence shows a good agreement with the numerical results.

For the cylindrical tank, the comparisons are performed between the tanks filled with water, LH2, and LNG as the main fluids with a filling level of 30% in terms of measuring the hydrodynamic forces and pressures on the left hemisphere of the tank. By comparing the results of the three mentioned fluids, water imposes the highest hydrodynamic forces on the tank walls for both low central baffle and non baffle cases and after that, LNG is ranked as the second fluid and lastly, LH2 is ranked as the third fluid with the least amount of imposed forces on the cylindrical tank walls over the natural period of 2.5s (refer to Figure 76 and Figure 77). In percentage terms, the hydrodynamic forces and pressures imposed on the tank walls by LH2 are 93.9% $\left(\frac{74-4.5}{74}\right)$ lower than those imposed by water for both baffled and non-baffle cases over the excitation period of 2.5s. This value is about 59% $\left(\frac{74-30.2}{74}\right)$ comparing water with LNG (refer to Table 18). The results also show that the efficiency of the low central baffle in the cylindrical tank over the natural period of 2.5s, to reduce the imposed forces on the left tank's hemisphere is about 25.6% $\left(\frac{74-55}{74}\right)$ when the main fluid is water, for LH2 it is around 17.7% $\left(\frac{4.5-3.7}{4.5}\right)$ and for LNG this reduction percentage is

around 23% $\left(\frac{30.2-23.2}{30.2}\right)$ (refer to Table 18).

By studying the comparison of the free surface elevation diagrams between water, LH2, and LNG in the cylindrical tank in chapter 5.6.5 and 5.6.6 for non baffle and baffled cases respectively, it appears that the recorded fluid motion at 30% filling level is almost unified between all simulated fluids over the natural period of 2.5s as for non baffled cases over this natural period, the height of the fluid is detected around 13.5cm for all simulated fluids (refer to figure 80) and for the cases with the low central baffle it is reduced to 10cm (refer to figure 81) which shows a drop of 25.9%.

A 3D case is also performed in this study as Table 5 in chapter 1.5 shows. This should be mentioned that in this research, the aim is not to simulate the 3D cases but to support the 2D cases, one three-dimensional case is conducted which its results is shown in chapter 5.7. As figure 82 shows, the comparison of the imposed forces on the left hemisphere of the cylindrical tanks between 2D and 3D cases shows a difference of 14% which makes the 2D cases valid in comparison of 3D cases.

The measured pressure on the left hemisphere of the cylindrical tank comparison between 2D and 3D cases that can be seen in figure 83 shows the difference of 13% as well. Thus, the 2D cases can be supported by these obtained 3D numerical results.

6.2 Future Work

It would be possible to expand this study by including other motion types and amplitude as well to obtain results that can be compared with real conditions, such as the results of tanks sloshing inside cargo tanks on decks. The other factor that can be included is to develop the inner structure of the tanks such as increasing or designing baffles using the 3D models. Finally, temperature could be incorporated to model the phase change and thermodynamic response as well which could be very influential especially for LH2 and modeling the cryogenic tanks.

Bibliography

[1] Chemistryexplained. http://www.chemistryexplained.com/Co-Di/Dewar-James.html. Accessed: 2021-11-17.

[2] Exo Cruiser. https://dodlithr.blogspot.com/2015/11/soviet-options-1989-for-manned-mars.html. Accessed: 2021-11-17.

[3] Howstuffworks. https://auto.howstuffworks.com/bmw-h2r.htm. Accessed: 2021-11-17.

[4] Hydrogen Storage - Basics. https://www.energy.gov/eere/fuelcells/hydrogen-storage-basics-0. Accessed: 2021-11-18.

[5] Lamb. hydrodynamics 1932, §.

[6] Liquid Hydrogen Distribution Technology. https://www.sintef.no/globalassets/project/hyper/presentations-day-2/day2_1105_decker_liquid-hydrogen-distribution-technology_linde.pdf. Accessed: 2021-11-18.

[7] livescience. https://www.livescience.com/28466-hydrogen.html. Accessed: 2021-11-17.

[8] Maritimecleantech. https://maritimecleantech.no/wp-content/uploads/2016/11/Report-liquid-hydrogen.pdf. Accessed: 2021-11-17.

[9] Rechargenews. https://www.rechargenews.com/transition/world-s-first-liquid-hydrogen-fuel-cell-cruise-ship-planned-for-norway-s-fjords/2-1-749070. Accessed: 2021-11-17.

[10] Safe Rack. https://www.saferack.com/glossary/cargo-tanks-transport-safety/. Accessed: 2021-11-26.

[11] Siemens STAR-CCM+. https://www.plm.automation.siemens.com/global/en/products/simcenter/STAR-CCM.html/. Accessed: 2021-11-19.

[12] STAR-CCM+ Product Guide. https://CD-adapco/12.04.011/STAR-CCM+12.04.011/doc/en/. Accessed: 2021-11-19.

[13] Think Fluid Dynamix. http://www.think-fluid-dynamix.com/multiphase-simulation/. Accessed: 2021-11-19.

[14] V. AEsoy, P. M. Einang, D. Stenersen, E. Hennie, and I. Valberg. Lng-fuelled engines and fuel systems for medium-speed engines in maritime applications. Technical report, SAE Technical Paper, 2011.

[15] C. K. Batchelor and G. Batchelor. *An introduction to fluid dynamics*. Cambridge university press, 2000.

[16] K. Biswal, S. Bhattacharyya, and P. Sinha. Non-linear sloshing in partially liquid filled containers with baffles. *International Journal for Numerical Methods in Engineering*, 68(3):317–337, 2006.

[17] D. Chongdong. Modeling and simulation of sloshing motion in partly filled tank. *Aalesund University College*, 2015.

[18] L. J. Clancy. *Aerodynamics*. John Wiley & Sons, 1975.

[19] E. Demirel and M. M. Aral. Liquid sloshing damping in an accelerated tank using a novel slot-baffle design. *Water*, 10(11):1565, 2018.

[20] U. Eberle, B. Müller, and R. Von Helmolt. Fuel cell electric vehicles and hydrogen infrastructure: status 2012. *Energy & Environmental Science*, 5(10):8780–8798, 2012.

[21] O. M. Faltinsen and A. N. Timokha. *Sloshing*, volume 577. Cambridge university press Cambridge, 2009.

[22] T. Flynn. *Cryogenic Engineering, Revised and Expanded*. 2004.

[23] E. Grotle, V. Æsøy, and E. Pedersen. Modelling of lng fuel systems for simulations of transient operations. *Maritime-Port Technology and Development; CRC Press: Cleveland, OH, USA*, page 205, 2014.

[24] E. L. Grotle. Thermodynamic response enhanced by sloshing in marine lng fuel tanks: Experimental work and numerical modelling. 2018.

[25] E. L. Grotle and V. Æsøy. Experimental and numerical investigation of sloshing in marine lng fuel tanks. In *International Conference on Offshore Mechanics and Arctic Engineering*, volume 57632, page V001T01A046. American Society of Mechanical Engineers, 2017.

[26] E. L. Grotle and V. Æsøy. Numerical simulations of sloshing and the thermodynamic response due to mixing. *Energies*, 10(9):1338, 2017.

[27] E. L. Grotle, K. H. Halse, E. Pedersen, Y. Li, et al. Non-isothermal sloshing in marine liquefied natural gas fuel tanks. In *The 26th International Ocean and Polar Engineering Conference*. OnePetro, 2016.

[28] R. A. Ibrahim. *Liquid sloshing dynamics: theory and applications*. Cambridge University Press, 2005.

[29] D. Liu and P. Lin. Three-dimensional liquid sloshing in a tank with baffles. *Ocean engineering*, 36(2):202–212, 2009.

[30] C. Ludwig, M. Dreyer, and E. Hopfinger. Pressure variations in a cryogenic liquid storage tank subjected to periodic excitations. *International Journal of Heat and Mass Transfer*, 66:223–234, 2013.

[31] J. Pedlosky et al. *Geophysical fluid dynamics*, volume 710. Springer, 1987.

[32] F. D. Rossini. A report on the international practical temperature scale of 1968. *Pure and Applied Chemistry*, 22(3-4):555–570, 1970.

[33] M.-A. Xue, J. Zheng, P. Lin, and X. Yuan. Experimental study on vertical baffles of different configurations in suppressing sloshing pressure. *Ocean Engineering*, 136:178–189, 2017.

Appendix

A Appendix A

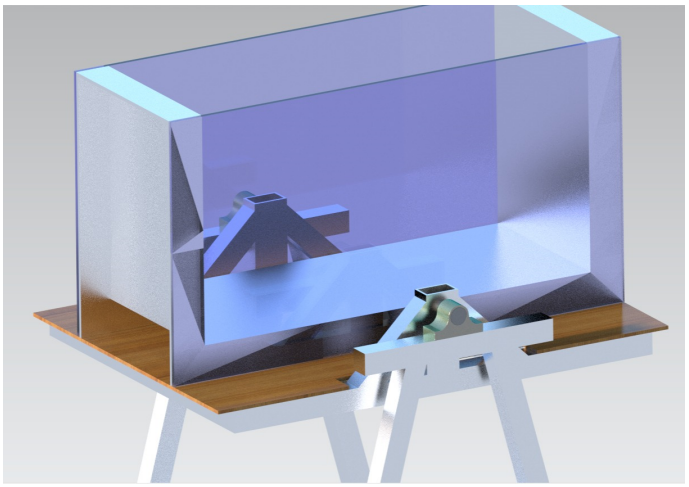

Figure 84: The experimental rig

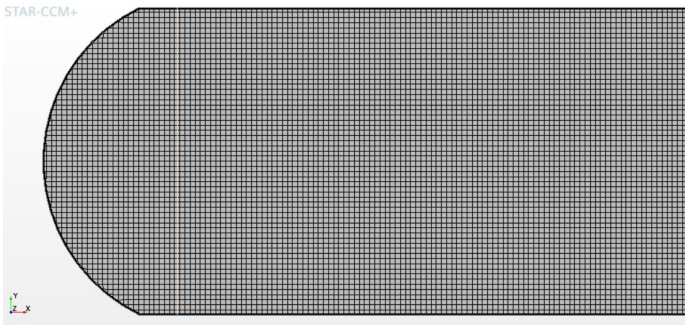

Figure 85: Cylindrical tank's mesh model

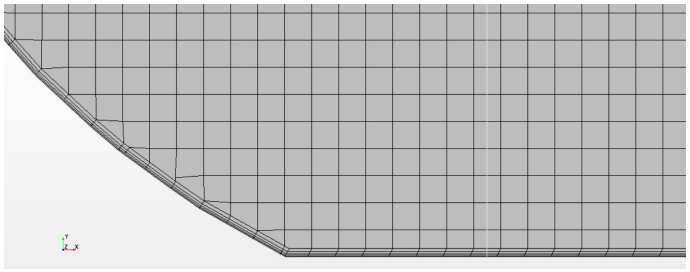

Figure 86: Cylindrical tank's prism layer model

B Appendix B

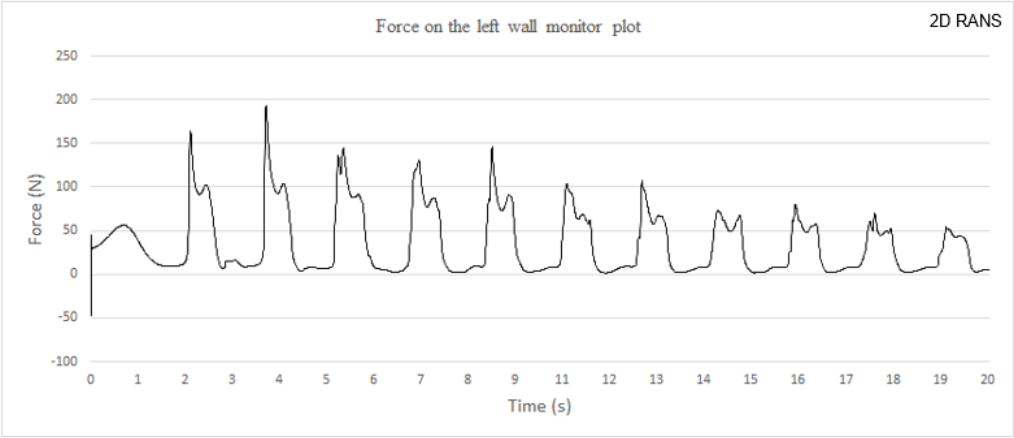

Figure 87: Numerical force monitor plot on the left wall of the rectangular tank over the excitation period of 1.65s when the filling level is 50% with water and no baffle is deployed

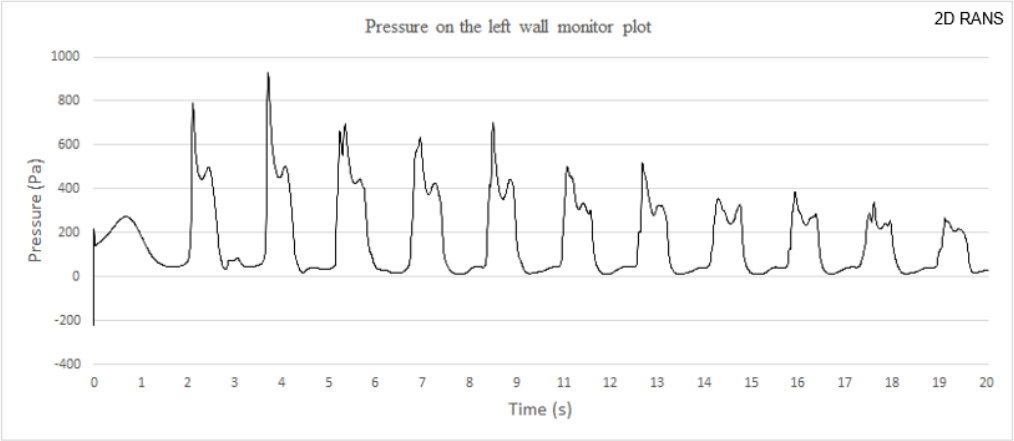

Figure 88: Numerical pressure monitor plot on the left wall of the rectangular tank over the excitation period of 1.65s, filling level of 50% with water and no baffle installed

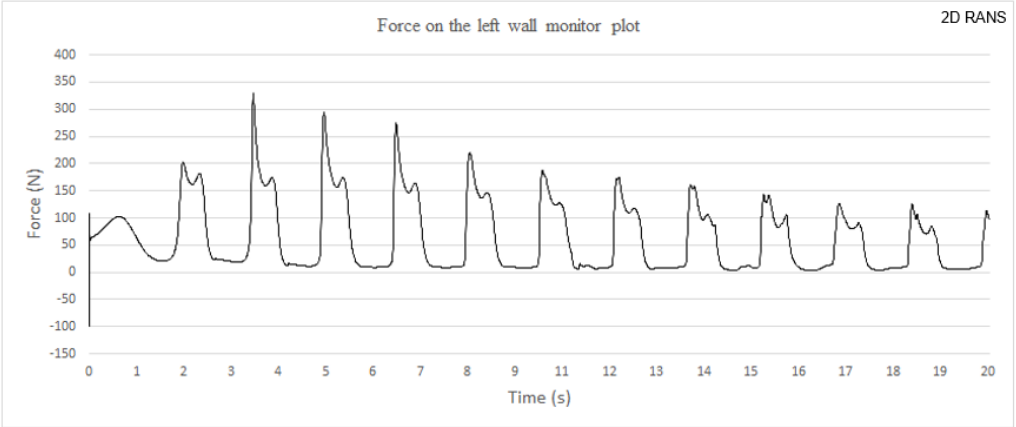

Figure 89: Numerical force monitor plot on the left wall of the rectangular tank over the excitation period of 1.6s when the filling level is 70% with water and no baffle is deployed

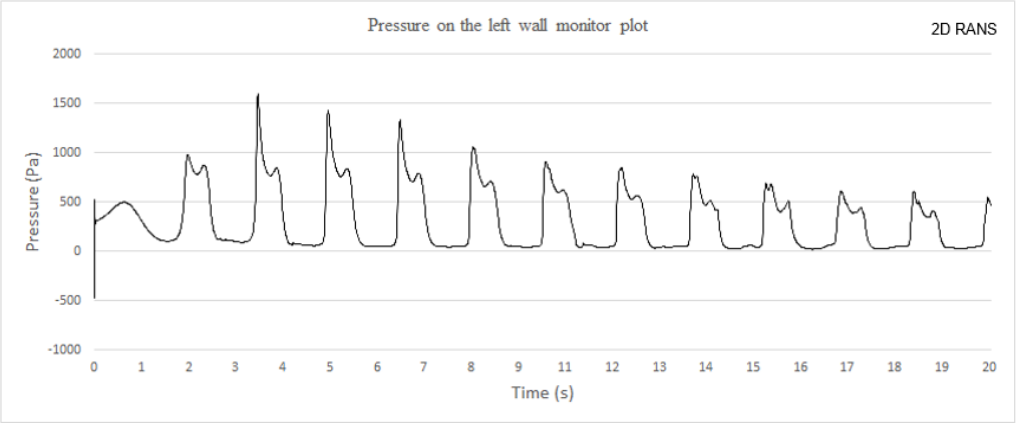

Figure 90: Numerical Pressure monitor plot on the left wall of the rectangular tank over the excitation period of 1.6s, when the filling level is 70% with water and no baffle installed

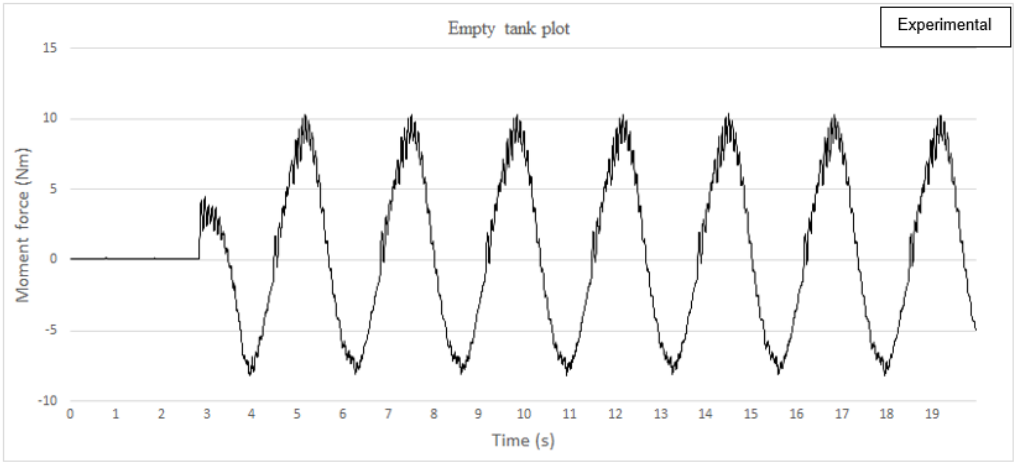

Figure 91: Experimental empty rectangular tank result over the excitation period of 2.35s of case 2 and case 4

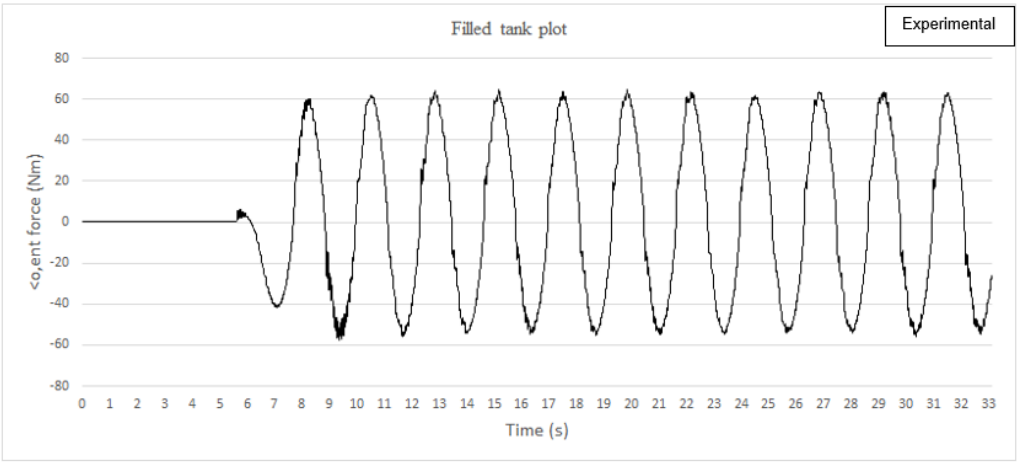

Figure 92: Experimental filled tank moment force result with the excitation period of 2.35s, 30% water level, without baffle of case 2

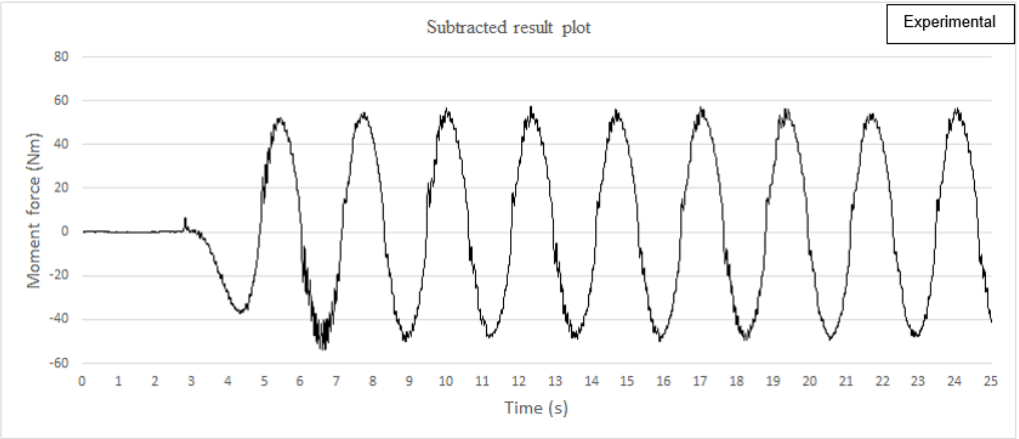

Figure 93: Experimental result of subtracted moment force graph with the period of 2.35s, 30% water level, without baffle for case 2

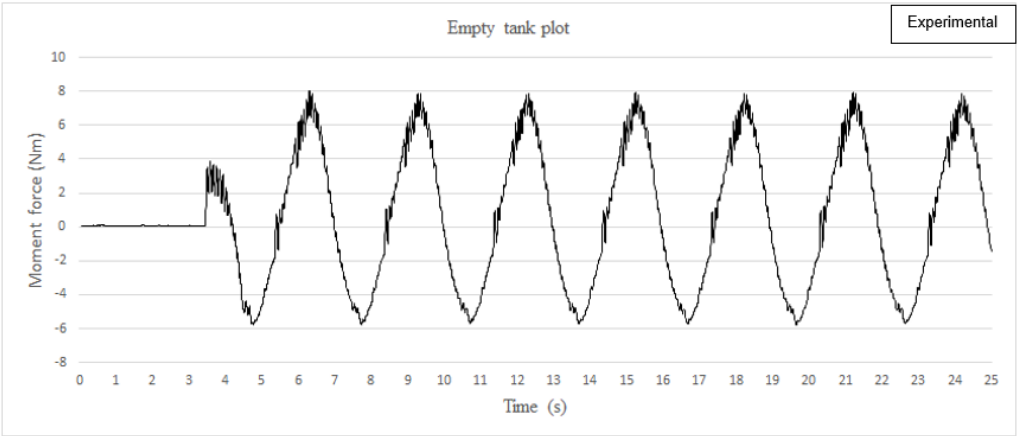

Figure 94: Experimental empty rectangular tank result over the excitation period of 3s of case 3

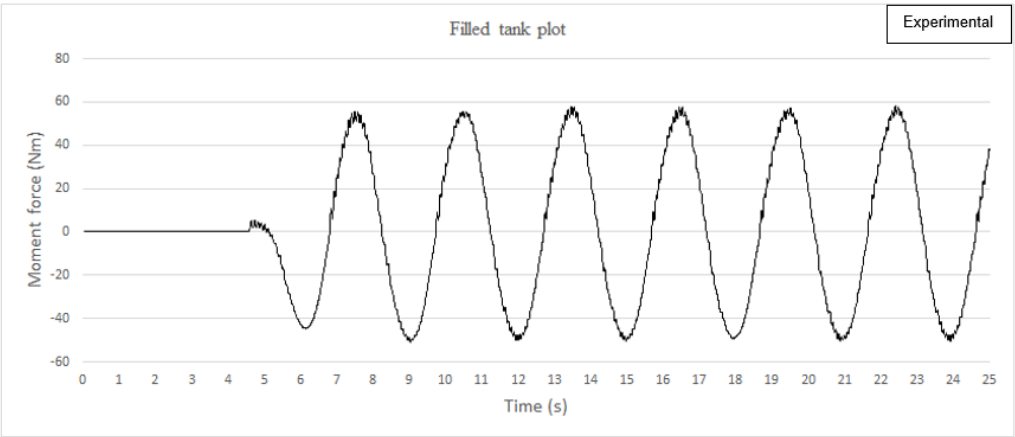

Figure 95: Experimental filled tank moment force result with the excitation period of 3s, 50% water level, low central baffle installed for case3

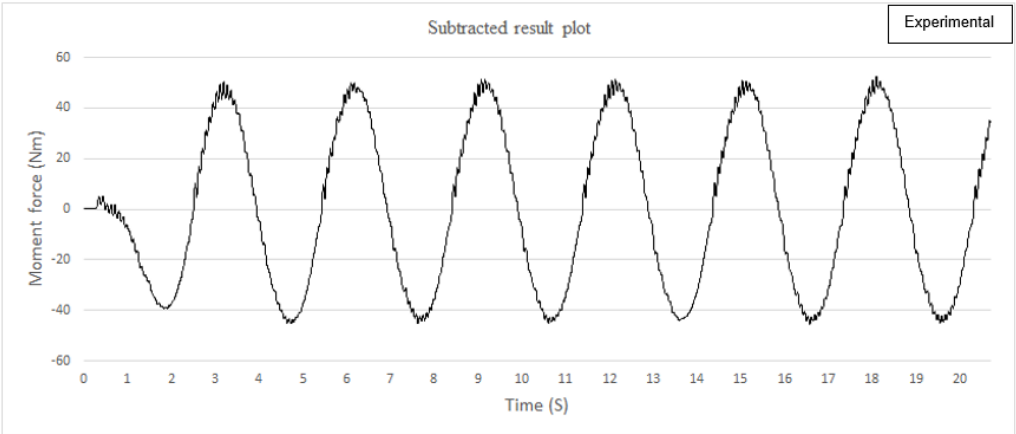

Figure 96: Experimental result of subtracted moment force graph with the excitation period of 3s, 50% water level, Low central baffle installed for case 3

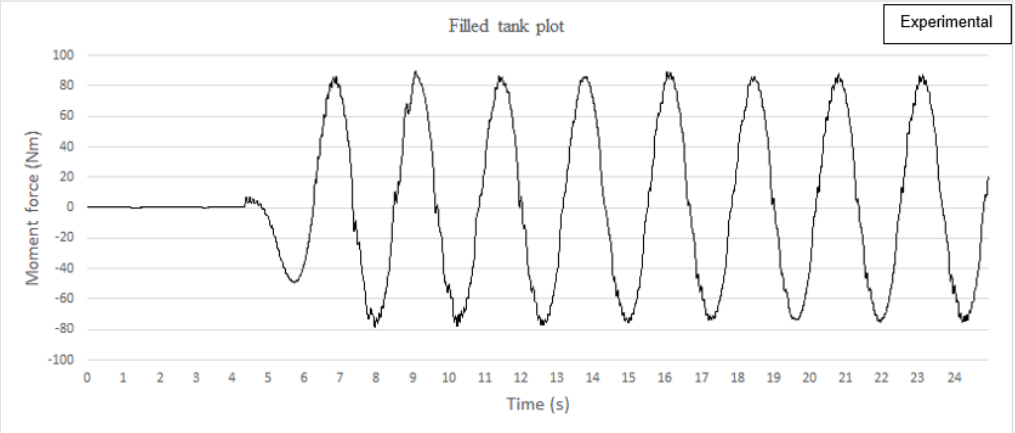

Figure 97: Experimental filled tank moment force result with the excitation period of 2.35s, 50% water level, without baffle for case 4

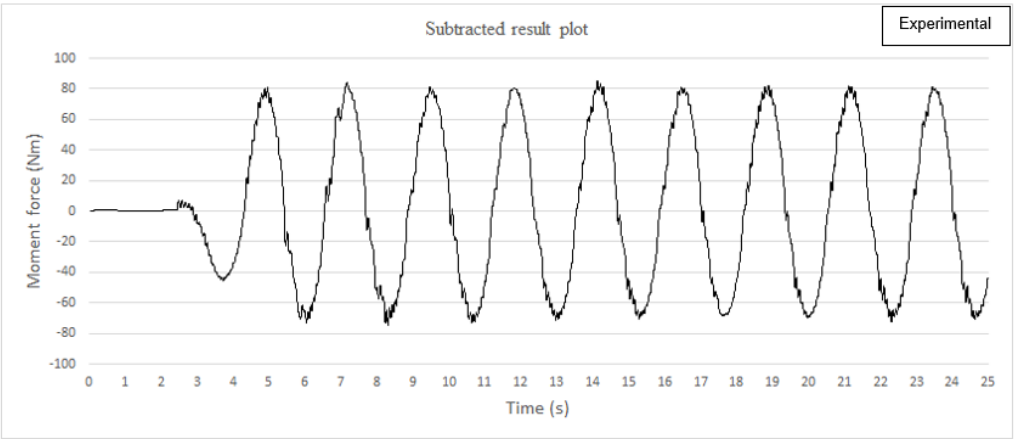

Figure 98: Experimental result of subtracted moment force graph with the excitation period of 2.35s, 50% water level, without baffle of case 4

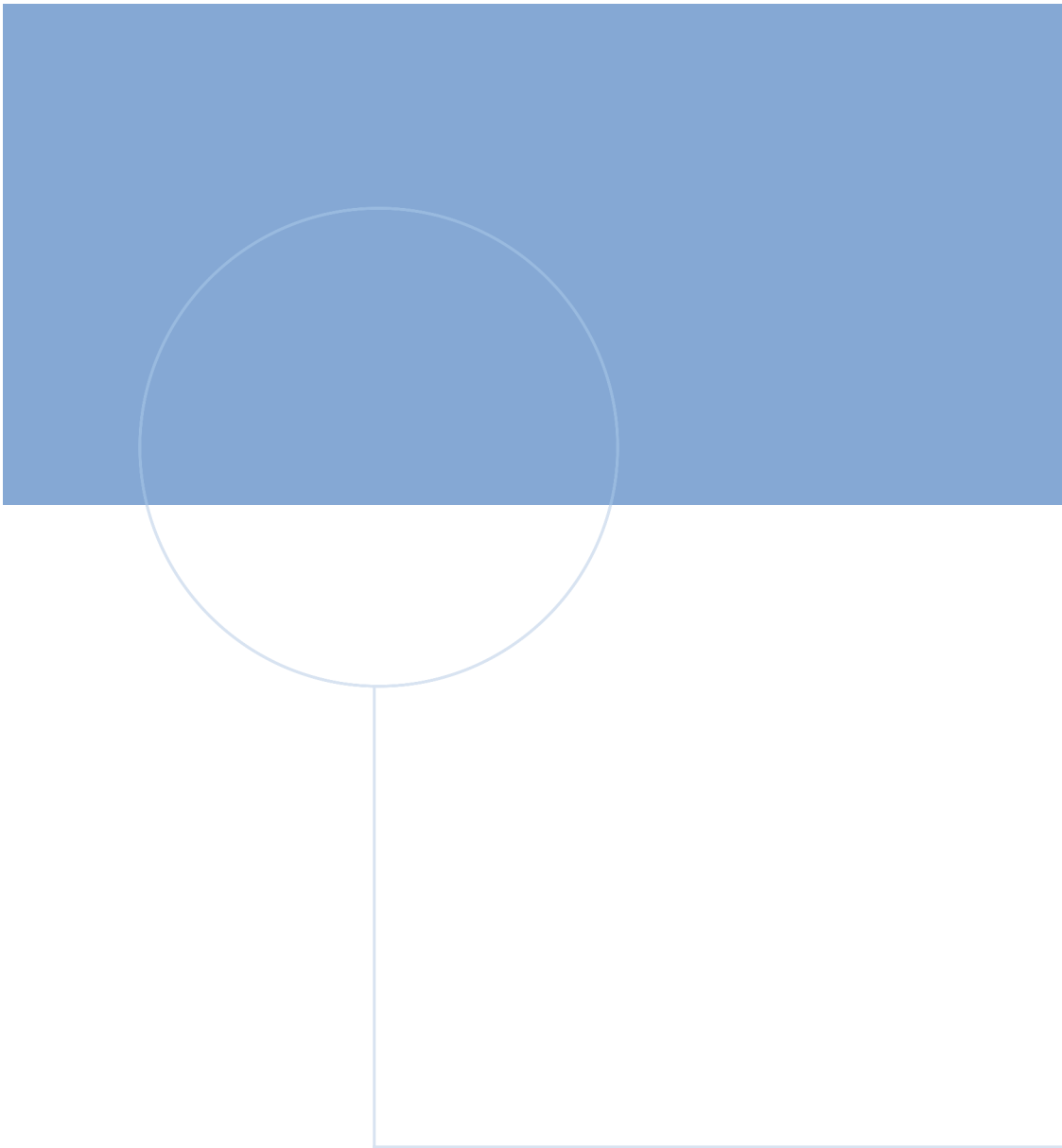

NTNU

Norwegian University of
Science and Technology